Final Technical Report

NASA Cooperative Agreement NCC2-971

"Geophysics of Small Planetary Bodies"

August, 1998

by

Erik I. Asphaug,
Principal Investigator
SETI Institute

As a SETI Institute PI from 1996–1998, Erik Asphaug studied impact and tidal physics and other geophysical processes associated with small (low-gravity) planetary bodies. This work included: a numerical impact simulation linking basaltic achondrite meteorites to asteroid 4 Vesta (Asphaug 1997), which laid the groundwork for an ongoing study of Martian meteorite ejection; cratering and catastrophic evolution of small bodies (with implications for their internal structure; Asphaug et al. 1996); genesis of grooved and degraded terrains in response to impact; maturation of regolith (Asphaug et al. 1997a); and the variation of crater outcome with impact angle, speed, and target structure. Research of impacts into porous, layered and prefractured targets (Asphaug et al. 1997b, 1998a) showed how shape, rheology and structure dramatically affects sizes and velocities of ejecta, and the survivability and impact-modification of comets and asteroids (Asphaug et al. 1998a). As an affiliate of the Galileo SSI Team, the PI studied problems related to cratering, tectonics, and regolith evolution, including an estimate of the impactor flux around Jupiter and the effect of impact on local and regional tectonics (Asphaug et al. 1998b). Other research included tidal breakup modeling (Asphaug and Benz 1996; Schenk et al. 1996), which is leading to a general understanding of the role of tides in planetesimal evolution. As a Guest Computational Investigator for NASA's HPCC/ESS supercomputer testbed, helped graft SPH3D onto an existing tree code tuned for the massively parallel Cray T3E (Olson and Asphaug, in preparation), obtaining a factor x1000 speedup in code execution time (on 512 cpus). Runs which once took months are now completed in hours.

For work conducted at the SETI Institute and NASA Ames, the PI was selected to receive the 1998 Urey Prize of the Division for Planetary Sciences of the American Astronomical Society. Recent work (Asphaug et al. 1998) attracted considerable interest from those concerned about the deflection of potentially hazardous near-Earth asteroids and comets; these computational results have been featured on CNN Headline News, NPR All Things Considered, the BBC World Service, and many other forums such as Discover, Sky and Telescope, and Astronomy magazines.

PUBLICATIONS

(1) Asphaug, E., J.M. Moore, D. Morrison, W. Benz, M.C. Nolan and R.A Sullivan (1996), "Mechanical and geological effects of impact cratering on Ida", Icarus 120, 158-184.

(2) Sullivan, R.A., E. Asphaug, M. Belton, M. Carr, C.R. Chapman, P. Geissler, R. Greeley, R. Greenberg, J.W. Head III, R. Kirk, P. Lee, A. McEwen, D. Morrison, J.M. Moore, R. Pappalardo, P. Thomas and J. Veverka (1996), "Geology of 243 Ida", Icarus 120, 119-139.

(3) Greenberg, R., W.F. Bottke, M.C. Nolan, P. Geissler, J.M. Petit, D. Durda, D. Morrison, J. Moore, E. Asphaug, and J. Head (1996), "Collisional and dynamical history of Ida", Icarus 120, 106-118.

(4) Asphaug, E. and W. Benz (1996), "Size, density, and structure of comet Shoemaker-Levy 9 inferred from the physics of tidal breakup", Icarus 121, 225-248.

(5) Schenk, P., E. Asphaug, W.B. McKinnon, H.J. Melosh, and P. Weissman (1996), "Cometary nuclei and tidal disruption: The geologic record of crater chains on Callisto and Ganymede", Icarus 121, 249-274.

(6) Nolan, M.C., E. Asphaug, H.J. Melosh, and R. Greenberg (1996), "Impact craters on asteroids: does gravity or strength control their size?", Icarus 124, 359-371.

(7) Asphaug, E. (1997), "Impact Origin of the Vesta Family", Meteoritics and Planetary Science 32, 965-980.

(8) Asphaug, E., S.J. Ostro, R.S. Hudson, D.J. Scheeres and W. Benz (1998), "The effect of collisions on small asteroids", Nature, in press.

(9) Asphaug, E., J.M. Moore, D. Morrison, P.H. Figueredo, R. Greeley, R.T. Pappalardo, L.M. Prockter, R. Tufts and the Galileo SSI Team (1998), "Crater-controlled fracture networks and the depth of ice lithospheres", LPSC XIX Abstracts.

(10) Asphaug, E. (1997), "New views of asteroids", Perspectives article in Science 277, 2070-2071.

(11) J.M. Moore, E. Asphaug, R.J. Sullivan, J.E. Klemaszewski, K.C. Bender, R. Greeley, P.E. Geissler, A.S. McEwen, E.P. Turtle, C. B. Phillips, B. R. Tufts, J.W. Head III, R.T. Pappalardo, K.B. Jones, C.R. Chapman, M.J.S. Belton, R.L. Kirk and D. Morrison (1998), "Large impact features on Europa: results of the Galileo nominal mission", Icarus, in press.

(12) Nolan, M.C., E. Asphaug, R. Greenberg and H.J. Melosh (1998), "Impacts on asteroids: fragmentation, regolith transport and disruption", Icarus, in press.

(13) Olson, K.M. and E. Asphaug (1998), "Impact simulations with a parallel SPH treecode", in preparation for Computer Physics Communications.

(14) Moore, J.M., E. Asphaug, R.J. Sullivan, J.E. Klemaszewski, R. Greeley, K.C. Bender, P.E. Geissler, A.S. McEwen, B.R. Tufts, J.W. Head III, R.T. Pappalardo, K.B. Jones, C.R. Chapman, M.J.S. Belton, R.L. Kirk, D. Morrison and the Galileo SSI Team (1998), "Landform degradation and mass wasting on icy Galilean satellites", Icarus, in press.

(15) Greeley, R., R. Sullivan, J. Klemaszewski, J.W. Head III, R.T. Pappalardo, J. Veverka, B. Clark, T.V. Johnson, M. Belton, J. Moore, E. Asphaug, M.H. Carr, G. Neukum, T. Denk, C.R. Chapman, C.B. Pilcher, P.E. Geissler, R. Greenberg, R. Tufts and the Galileo SSI Team (1998), "Geology of Europa", Icarus, in press.

PLANETARY SCIENCE

New Views of Asteroids

Erik Asphaug

Imagine exploring the surface of a near-Earth asteroid. You must be delicate in your traversal of this warped and mountainous world, an irregular agglomeration several kilometers across that pulls with a mere ten-thousandth the gravity of Earth (1)—a body so small you might jump off, never to return. The asteroid spins beneath a brilliant sun, sweeping out constellations and cycling the landscape into night and day more rapidly than you are used to (2). Promontories loom at improbable angles, and a stark horizon drops abruptly a hundred meters from your feet. In this precipitous world, your progress is further hindered by microgravity and the extraordinarily loose soil: Each gentle step raises volumes of dust and sends you floating for minutes. Global voyages may in principle be achieved with measured steps, but it takes an hour or more to complete the slow, all-but-unpredictable trajectories governed by the weird gravity and Coriolis forces (3). For the most part you just relax and enjoy the view of your home planet, appearing the size of a marble at arm's length, into which this asteroid may someday collide if left alone.

This microgravity fantasy is rooted in spacecraft and radar imaging of several near-Earth asteroids and other minor planets, and some application of routine physics. We can hope to witness this scenario in our lifetimes. More detailed speculation remains imprudent until we find out whether asteroids are intact, or fractured and cavernous; whether they sequester volatile ices in their not-so-deep interiors; and whether they harbor rich deposits of metals, exotic minerals, or prebiotic compounds. Almost certainly asteroids are stranger than we assume, and the enchantment of their discovery—spurred on by wide public access to recent images and reflected in the popularity of comets and asteroids in contemporary doomsday cinema—is spreading to a wide forum as we begin to learn the answers to these questions.

Near Earth Asteroid Rendezvous (NEAR), the first-launched NASA Discovery spacecraft, is a spearhead for asteroid science. NEAR will maneuver in early 1999 into the first orbit about a low-gravity planet, the ~14 km × 40 km Earth-approaching asteroid 433 Eros, to circle some 30 to 100 km above the surface, revolving at a stately ~5 m s^{-1} for a year or more. Multispectral mineralogy, altimetry, magnetometry, orbital gravimetry, and unprecedented color images (with a resolution of 3 m per pixel) will transform little-known Eros into one of the most exhaustively explored members of our solar system, and the first body in that size range to be (we hope) approximately understood.

The view from asteroid 4179 Toutatis on 29 September 2004, when it comes within 0.1 astronomical unit of Earth. The view is from an observer in close orbit; the stars and the appearance of Earth are exact, with Earth about the size of a full moon. [Composite image created by E. De Jong and S. Suzuki of DIAL/JPL]

Last June, as an en route preview to that encounter, NEAR flew by the main-belt asteroid 233 Mathilde for the first look at a primitive C-type object (4), as reported by Veverka *et al.* and Yeomans *et al.* in this issue on pages 2106 and 2109 (5). Although the resolution was 50 times as coarse as expected at Eros, the images of Mathilde reveal some surprises and provoke an overdue reevaluation of asteroid geophysics. Mathilde has survived blow upon blow with almost farcical impunity, accommodating five great craters with diameters from 3/4 to 5/4 the asteroid's mean radius, and none leaving any hint of global devastation. Given that one of these great craters was the last to form, preexisting craters ought to bear major scars of seismic degradation, which they do not. Furthermore, asteroids Gaspra and Ida (encountered by Galileo en route to Jupiter) and the small martian satellite Phobos all exhibit fracture grooves related to impact, yet fracture grooves are absent on the larger, more-battered Mathilde. Perhaps fractures are hidden beneath deep regolith, or are so pervasive that Mathilde is nothing but regolith: a "rubble pile." In any event, Mathilde demonstrates that the formation of large craters can be quite local, and locally energetic: Ejecta was accelerated to escaping speeds (~20 m s^{-1}) without greatly disturbing the remainder of the asteroid. Interstitial voids greatly limit an impact shock wave's propagation but also enhance particle speeds within a smaller shocked region; porosity may thus explain Mathilde's strange craters, given its very low (~1.3 g cm^{-3}) density.

Until NEAR succeeds at Eros, the most detailed information about Earth-approachers derives from radar echo experiments. Powerful polarized signals are beamed from (and echoes received at) either of two antennas—one in Arecibo, Puerto Rico, and the other in Goldstone, California. Unlike optical imaging, this techniqu additionally constrains surfac roughness, electrical propertie density, position, velocity, rotation, and shape (6). Less than weeks after the discovery of Earth-crossing asteroid 1989PB, radar echo experiments revealed the first detailed images (7) of an asteroid—a probable contact binary later named 4769 Castalia. A more favorable apparition was provided by 4179 Toutatis, yielding the reconstructed view (8) shown in the figure. Extensive upgrades to the Arecibo antenna will be completed this spring, providing dozens of Toutatis-quality detections per year, spacecraft-quality images of the closest approachers, and hundred-pixel images of dozens of main-belt asteroids (9).

These irregular bodies (~1 to ~50 km in diameter) may hardly seem like planets in their own right, yet the distinction is becoming vague. Consider the third largest asteroid, 4 Vesta, a basalt-covered volcanic body 530 km in diameter that resembles the moon as much as it does Mathilde or Toutatis. Recent views (36 km per pixel) by the Hubble Space Telescope (10) show a 460-km crater, with raised rim and central peak, covering the entire southern hemisphere—an impact scar surpassing (in relative diameter, but not relative depth) the great chasms of Mathilde. Such craters greatly challenge our understanding of impact processes on asteroids, and on planets in general; evidently, our sci-

An enhanced version of this Perspective with links to additional resources is available for *Science* Online subscribers at www.sciencemag.org

---

The author is at the SETI Institute/NASA, Ames Research Center, Moffett Field, CA 94305, USA. E-mail asphaug@cosmic.arc.nasa.gov

ence must adapt. The study of asteroids is therefore particularly exciting, as small planets provide the fulcrum for the growth of planetology, and for an evolution of geophysics in general. Complex and poorly understood solar system processes—such as impact cratering, accretion and catastrophic disruption, the evolution of volcanic structures, and the triggering of differentiation—may reveal themselves only in a study across the gamut of planets, from the least significant house-sized rock to the most stately terrestrial world. Like clockwork miniatures, asteroids demonstrate primary principles governing planetary evolution at an accessible scale, and thousands await discovery and exploration in near-Earth space alone.

References and Notes

1. For a typical asteroid with density 1 5 < ρ < 2 5 g cm⁻³, escape velocity (in meters per second) is about equal to asteroidal radius (in kilometers). If you can jump half a meter on Earth, you could leap off of an asteroid 5 km in diameter.
2. Rotational periods vary tremendously. Speedy Castalia revolves every 4 hours. Mathilde every 17 days Non-principal-axis rotator Toutatis (see figure) has nothing that can be called a "day," forever showing different horizons For further insights, see Scott Hudson's Web page. http://www.eecs.wsu.edu/~hudson/asteroids.html.
3. This "human ICBM" mode of transportation is ill-advised. D. J. Scheeres et al., Icarus 121, 67 (1996) demonstrated the complexity of trajectories proximal to Castalia
4. For a video view of the Mathilde encounter, see http://hurlbut.jhuapl.edu/NEAR/Mathilde/images.html#ani
5. J. Veverka *et al.*, *Science* **278**, 2109 (1997). D K Yeomans *et al.*, *ibid.*, p. 2106
6. S. J Ostro *et al.*, *Astron. J.* **102**, 1490 (1991) Visit the asteroid radar research home page at http://echo.jpl.nasa.gov
7. R S Hudson and S J Ostro *Science* **263**, 940 (1994).
8. ______, *ibid.* **270**, 84 (1995)
9. The upgraded Arecibo antenna will also be used to image the "back side" of Mathilde, which was not seen during the NEAR flyby
10. P C Thomas *et al.*, *Science* **277**, 1492 (1997)

MATERIALS SCIENCE

Conducting Polymers: From Novel Science to New Technology

J. Campbell Scott

On page 2103 of this issue, Lonergan describes a hybrid device in which an inorganic semiconductor and a conducting polymer are combined to create a diode, one of the fundamental building blocks of electronics (*1*). Polymers of the sort used by Lonergan, which become electrically conductive after being doped with electron donors or acceptors, have occupied an increasingly prominent place in physics, chemistry, and materials science since Shirakawa first reported his method for the polymerization of acetylene (*2*). Much research has since been motivated (and many grants funded) by the conviction that there is a huge potential for technological and commercial exploitation, yet the record reveals only a few truly successful products (*3*). What can we learn by examining the history of conducting polymers?

In addition to the technological possibilities, interest in polyacetylene was driven by scientific curiosity into the effect of broken symmetry in the *trans*-isomer form, which gives rise to highly nonlinear phenomena such as solitons (*4*). Experimental data in the early 1980s were eagerly scrutinized by theorists in search of tests of their calculations in nonlinear dynamics. Identification of polarons (single electronic charges, self-trapped by a structural distortion) and bipolarons (doubly charged) followed in short order (*5*). At the same time, synthetic chemists were exploring new materials and synthetic procedures to yield higher conductivity and environmental stability. The "holy grail" became an air-stable polymer with the conductivity of copper. In retrospect, it is hard to believe that serious consideration was given to the use of plastics to replace wiring, circuit board connections, motor windings, or solenoid coils.

Nevertheless this period was an extremely productive time, owing to the synergy of scientists with backgrounds as diverse as field theory, solid-state physics, and physical and synthetic chemistry. A milestone was reached in the development of conducting polymers when it was recognized that they could be synthesized by electrochemical polymerization, then subsequently dedoped and redoped by electrochemical methods (*6*). Thus, properties such as electrical conductivity and optical absorption could be manipulated in ways that are not possible with conventional semiconductors and metals. This distinction has led to the introduction, or at least the trial, of conjugated polymers in new technological niches, and it is this feature that Lonergan exploits (*1*).

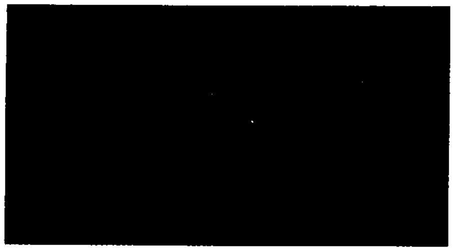

Conjugated conductor. Space-filling model of a polypyrrole chain. Carbon atoms are white; nitrogen atoms are blue.

One of the earliest commercialization attempts was in batteries (*3*), on the basis of electrochemical energy storage characteristics combined with a perceived weight advantage. However, because of breakthroughs in other battery materials such as lithium ion and metal hydride, and because volumetric capacity turned out to be more important than weight, conducting polymer batteries were not successful and have been withdrawn from the market. Electrolytic capacitors, introduced in 1992, have been more successful. Here, conducting polymers permit an all-solid-state device and obviate the problem of containing a liquid electrolyte by gelation or encapsulation.

Another unique and advantageous property of conjugated polymers lies in the processing and compatibility that one associates with plastics. The earliest examples—polyacetylene, polyphenylene, polythiophene, and polypyrrole (see figure)—were not very tractable, but considerable synthetic effort to add side-chain substituents has resulted in materials that are quite soluble in common organic solvents, and even (as with derivatives of polythiophene and polyaniline) in water. Thus, the materials engineer has at hand processes for casting thin conducting layers on a wide variety of substrates, or for blending the conducting polymer with structural polymers in films and fibers.

The resulting range of applications accounts for the majority of today's production of conducting polymers. Antistatic blends of conducting polyaniline or polypyrrole in textile fibers prevent the buildup of charge and the resultant damaging discharge. Camouflage fabrics can be treated to prevent radar reflection. A major manufacturer of photographic film coats the base layer with a transparent conductive layer of polyethylenedioxythiophene in order to make the sheet easier to handle during deposition of the optically active dyes, and to alleviate some of

---

The author is in the IBM Research Division, Almaden Research Center, San Jose, CA 95120-6099, USA. E-mail: jcscott@almaden.ibm.com

ICARUS 120, 158–184 (1996)
ARTICLE NO. 0043

7

Mechanical and Geological Effects of Impact Cratering on Ida

ERIK ASPHAUG, JEFFREY M. MOORE, AND DAVID MORRISON
NASA Ames Research Center, MS 245-3 Moffett Field, California 94035
E-mail: asphaug@cosmic.arc.nasa.gov

WILLY BENZ
Steward Observatory, University of Arizona, Tucson, Arizona 85721

MICHAEL C. NOLAN[1]
Lunar and Planetary Laboratory, University of Arizona, Tucson, Arizona 85721

AND

ROBERT J. SULLIVAN
Department of Geology, Arizona State University, Tempe, Arizona 85287

Asteroids respond to impact stresses differently from either laboratory specimens or large planets. Gravity is typically so small that seismic disturbances of a few cm s^{-1} can devastate unconsolidated topography. Yet the presence of regolith and the likelihood that many asteroids are gravitational assemblages tell us that gravity cannot generally be ignored. We use numerical models for impact fracture in solids to examine the initial stage of crater formation on asteroid 243 Ida, up to the cessation of fracture and the establishment of the cratering flow; at this stage we can infer final crater diameters but not profiles. We find that a modified strength scaling applies for craters up to a few 100 m in diameter forming in rock subject to Ida's gravity, and that gravity controls all craters larger than ~1 km. "Bright annuli" around a number of intermediate craters may be the result of low-velocity surface disturbances, rather than bright proximal ejecta deposits. We also consider large impactors, to which Ida presents a curved, finite target surface with irregular gravity. These can excavate asymmetrical concavities. Stresses from large events can refocus and cause fracture far from the crater; using the shape of Ida as a basis for 3D hydrocode simulations, we show that impact genesis of the Vienna Regio concavity can cause fracture in Pola Regio, where grooves are observed in spacecraft images. Other simulations indicate that the formation of the ~10 km crater Azzurra might have reopened these fractures, which may account for their fresh appearance. This mechanism of groove formation requires an interior which coherently transmits elastic stress. While this precludes a classic "rubble pile" asteroid, it does allow well-joined fault planes, and welded blocks or pores smaller than the stress pulse.

I. INTRODUCTION

The physical geology of asteroid 243 Ida can be explained largely in terms of a history dominated by several collisions of global consequence, plus a fusillade of smaller impacts pocking and gardening the surface and launching seismic waves through the local rock. The pre-history of Ida, probably as part of a larger parent body from which the entire Koronis family derived, is not considered here, although Ida's irregular shape may suggest a collisional genesis. In this paper we study the mechanics of impact in an effort to establish a substantive correlation between theoretical predictions and the Galileo observations. As a result we hope to offer insights into the mechanical properties of Ida (whether it is intact or has deep regolith, etc.), together with a clearer general understanding of impact cratering on small bodies.

Part of our research is aimed at non-local effects of large craters in finite targets. The idea that certain landforms on small objects might be due to distal effects from large impacts was raised by Thomas *et al.* (1979) in an attempt

---

[1] Current address: Arecibo Observatory, P.O. Box 995, Arecibo, Puerto Rico 00613.

0019-1035/96 $18.00

to explain the formation of grooves on the Martian satellite Phobos. Thomas and Veverka (1979) speculated that grooves should be found on some asteroids, in light of the probable role of collisions with these objects, if grooves are indeed impact-induced. Grooves were observed on asteroid 951 Gaspra by the Galileo spacecraft, and their genesis was attributed to a violent collisional history (Veverka *et al.* 1994). Based on the Gaspra example, Veverka *et al.* (1994) applied the criteria of Thomas and Veverka (1979) to predict grooves on Ida. Their expectations were fulfilled during the Galileo encounter (Belton *et al.* 1994), where grooves appeared to occur most densely at the elongate 180E end (Pola Regio) in the areally limited high-resolution images. Their morphology is discussed by Sullivan *et al.* (1996).

Related to the possibility of groove formation by fracture from large impacts is the issue of asteroid interior coherence and porosity. Are many asteroids rubble piles, as some researchers (e.g., Davis *et al.* 1979) suggest? Given the possible discrepancy between Ida's derived density and the density of candidate meteorite analogs (Belton *et al.*, 1996), the notion of impact-induced porosity remains relevant. We use fracture grooves as a crude seismological record, examining these outward manifestations of powerful impact stresses to infer the nature of the asteroid's interior. This method was pioneered by Fujiwara (1991) and developed numerically by Asphaug and Melosh (1993) and Asphaug and Benz (1994) to learn about the interior of Phobos. We compare post-impact accelerations with self-gravity in damaged regions to see whether substantial porosity could be introduced during a large cratering event.

The very low gravity of small asteroids has been part of the impetus to understand the relative role of target strength versus gravity in crater evolution (Housen *et al.* 1983). Our intuition can serve us poorly, particularly when we look at the cratered surface of an asteroid and attempt to extrapolate directly from our knowledge of the Moon, an object whose surface gravity is ~200 times as large. But neither can we ignore self-gravity; at sufficient distance from any noncatastrophic impact the ground motion becomes so slow that a very modest gravitational acceleration can dominate. If the rock is broken by the impact stress at that distance, or is already strengthless, then the crater structure may be governed by gravitational forces (Asphaug and Melosh 1993; Nolan *et al.* 1995).

Another issue relates to the irregular gravitational potential of many asteroids and to the Coriolis Forces, which may be quite pronounced in comparison to the modest gravity. Craters forming in a complex gravitational and inertial environment may have morphologies very different from craters forming in a half space. Purely geometrical effects must also be considered if the crater is large in comparison with the local radius of curvature, or in comparison with the asteroid itself. The relevance of this issue crystallized with the observation of several approximately circular concavities on 951 Gaspra, which some interpreted as craters. An alternative hypothesis, that these concavities are not craters but "spallation scars," prompted an ongoing debate (Belton *et al.* 1992; Chapman *et al.* 1993; Greenberg *et al.* 1994). Similar concavities are observed on Ida, encouraging detailed investigations into the plausibility of different proposed mechanisms for their origin.

With the help of a fracture mechanics hydrocode (Benz and Asphaug 1994a,b; Benz *et al.* 1995; Asphaug and Benz 1994) that resolves some of the statistical and hydrodynamical inconsistencies of previous methods, we examine the transition from small craters, whose diameters and shapes are governed primarily by mechanical strength, to large craters, whose sizes and shapes are governed by gravity. Our code has been tested extensively; by integrating fragmentation flaw by flaw, it allows stress and strain rate to fluctuate (and crack growth to cease and resume) during the course of failure. We study the general effect of target curvature for the largest impacts and use a 3D hydrocode grid derived from the topography of Ida to examine cratering, as well as possible distal effects such as groove formation, associated with three specific impact structures. We model the evolution of the crater only up to the completion of fracture damage and the emplacement of the velocity field—several tens of seconds for large craters on Ida. The subsequent evolution, over a timescale of hundreds or thousands of seconds, cannot be modeled with existing techniques.

No matter how carefully an impact model has been tested against laboratory and field data, it cannot be applied blindly to targets of unknown composition. Cautious interpretations are in order. But conversely, low-gravity targets such as Ida offer a unique opportunity for *evaluating* impact models, since they preserve subtle structures which do not form (or are hidden) on relatively high-gravity targets such as the Moon. Many codes can model a crater; if a code can also reproduce accompanying features such as distal fracture grooves and proximal albedo markings, that lends further credence to its method.

II. MODELS OF DISRUPTIVE IMPACT INTO SOLIDS

Scaling

Prior to the advent of impact fragmentation codes in planetary research (Melosh *et al.* 1992; Benz and Asphaug 1994a,b), formalisms were derived to achieve the necessary extrapolation, across six or more orders of magnitude, from the scale of the laboratory to the size range of asteroids, comets and planetesimals. These powerful and versatile *scaling laws* derive from the so-called π-theorem of Buckingham (1914) and can reduce the number of relationships in a system by the number of units of measurement, typi-

cally three: mass, distance, and time. One constructs dimensionless assemblages of constants (such as the "gravity scaled size" $g\, r_i/v_i^2$, where g is the surface gravity and v_i is the impact velocity) which can replace a dimensional quantity (e.g., the impactor size r_i) in the equations, with a corresponding reduction of free parameters. Reviews of scaling laws applied to cratering and finite-body disruption are found in Fujiwara *et al.* (1989), Melosh (1989), and Holsapple (1993), and a straightforward introduction to dimensional analysis with an emphasis on cratering is provided by Schmidt and Housen (1995).

Like all powerful tools, dimensional analysis must be applied with restraint. For example, models scaled from the original crater ejection velocity experiments by Gault *et al.* (1963) predict an absence of regolith on asteroids smaller than several tens of km (Veverka *et al.* 1986, Housen *et al.* 1979). These models were derived for simple materials whose strength depends neither on target size nor loading rate; a recent scaling analysis including rate-dependent strength (Housen 1992, Housen and Schmidt 1995) may reconcile the models with observation. Scaling laws apply to domains of functional dependencies which are often narrow for nonlinear systems; for example, they break down if at some point the fundamental length ceases to be the impactor radius and becomes instead the grain size in the soil or the mean distance between flaws in the target rock.

Another approach (see Appendix) is to incorporate what is known about rocks and about gravity into a numerical system, or hydrocode, which directly integrates a target's evolution during impact. This method has the advantage of defining functional relationships implicitly, without having to know of their existence beforehand. For example, rate-dependent strength is an automatic property of *any* hydrocode which activates flaws that are distributed according to a power-law distribution and allows them to grow at a finite speed. Furthermore, behavior is not required to be even approximately linear except during the course of a single time-step. The predictive power of numerical models relies upon the limited data available concerning the fracture properties of relevant materials, and upon good equations of state (including some idea of what asteroids are made of). The same issues concern the crater scaling models, although they typically encapsulate all material properties (and hence all uncertainty about material properties) into two parameters, strength and density.

A problem unique to numerical analyses is that, while requiring no underlying functional relationships beyond the coded equations, neither do they automatically generate insight. Instead, they provide megabytes of numbers which modelers frequently refer to as "data" (to the ire of observationalists). These numbers are interpreted much as one interprets measurements taken from a natural system: one looks for patterns and trends. Another difficulty is a practical one: presuming we have captured the essence of dynamic rock mechanics in a set of nonlinear, coupled partial differential equations, it is a formidable task to solve them. Great care must be taken to ensure that the integrations are stable and accurate; the computational requirements can be prohibitive. For these reasons, scaling laws often provide a more satisfactory *conceptual* framework, while numerical models are used to navigate between known regimes and the unknown. Numerical results can also suggest appropriate scaling relationships to the modeler. The Appendix provides the basic hydroequations (mass, energy, and momentum conservation), an elastic strength model (Hooke's law), the von Mises plastic yielding relation, and our recipe for brittle fracture.

Fracture

Three fundamental assumptions about flaw activation and crack growth are shared between the model of Benz and Asphaug (1994a) and the methods of Grady and Kipp (1980) and Melosh *et al.* (1992), from which it evolved: (1) Flaws are distributed according to a Weibull power law distribution

$$n(\varepsilon) = k\varepsilon^m \qquad (1)$$

(Weibull 1939, Jaeger and Cook 1969), where ε is the strain at which a flaw becomes active, n is the number density of flaws weaker than this threshold, and k and m are laboratory-derived constants. (2) Active flaws propagate at a constant velocity c_g. (3) Cracks relieve stress in a sphere that circumscribes them. These three basic assumptions, plus the assumption of a constant strain rate $\dot{\varepsilon}$, result in the one-dimensional integrals of Grady and Kipp (1980), developed for modeling *in situ* explosive fragmentation of oil shale. The key parameter in their model is a scalar fracture damage, $0 \le D \le 1$, where $D = 0$ for intact rock and $D = 1$ for cohesionless, frictionless rubble. The method also allows for the statistical computation of fragment sizes.

Melosh *et al.* (1992) recast the Grady–Kipp equations in differential form and adapted them to multidimensions via an eigenvalue decomposition of the total stress tensor. Their model successfully reproduces fragment size distributions for catastrophic hypervelocity impact events. It is a statistical model in which the flaw distribution in all cells are equivalent. The activation threshold (the same for every cell) is derived by inverting Eq. (1): the weakest flaw likely to exist in a rock with volume $V \equiv 1/n(\varepsilon_{\min})$ has a failure threshold $\varepsilon_{\min} = (kV)^{-1/m}$. Whenever the local strain exceeds this value in any cell, Grady–Kipp damage is integrated together with a statistical evaluation of the local fragment size distribution. At the end of the simulation, cell-by-cell fragment size distributions are summed for the entire target. While the method tends to reproduce

fragment size statistics faithfully, one problem is that all cells "know" the dimensions of the target. As a result, fragmentation can occur due to the local activation of flaws which are actually unlikely to exist in any particular cell. Consequent errors in hydrodynamics are due, essentially, to the fact that cells become strengthless even if they are fragmented into sizes larger than the cell size. This is a concern only for strain rates low enough that the weakest flaws are of importance. Because large fragments and fracture planes are created specifically in response to the weakest available flaws, however, a different treatment is needed to meaningfully resolve crack growth on a scale larger than the cell size.

The method used here largely coincides with the method of Melosh *et al.* (1992) when the strain rate is sufficiently high, but it also accurately models relatively low strain rate events such as those which occur beyond the edges of a crater. In particular, it has proven capable (Benz and Asphaug 1994b) of reproducing the actual crack growth trajectories inside laboratory targets. For instance, this model matches the sizes, shapes, and velocities of fragments—including spall plates and the quasi-spherical core fragment—produced experimentally by Nakamura and Fujiwara (1991). It also predicts crater diameter, spall structure, and sound speed vs. distance from impact for cratering experiments by Ahrens and Rubin (1993).

This level of agreement with experiment is made possible by distributing Weibull flaws (Eq. (1)) *explicitly*, as initial conditions, so that each cell is seeded with many flaws (typically hundreds or thousands) at random. In this manner the flaw statistics are made independent of hydrocode resolution, and the minimum fracture threshold is local, not global. A 1 cm^3 subvolume of a 10 m^3 target, for instance, has on average the same flaws as a self-standing 1 cm^3 target. Integrating damage flaw by flaw makes possible a realistic response to changing strain rate. Since many explicit flaws exist independently within a given cell, damage can stop and resume in response to episodic stress. But most important, fragmentation is computed in an accurate and hydrodynamically consistent manner on a scale larger than the cell size. The Appendix fully describes this method.

III. SMALL CRATERS

The formation of small craters on asteroids does not differ appreciably from the formation of small craters on terrestrial planets from any geometrical or mechanical perspective, assuming that their surfaces are not grossly dissimilar, and neglecting that impact velocity tends to increase with target size. During the first few moments of a cratering event, by which time the material around the contact region has been fully shattered, the crater does not "know" whether the target is large or small, provided that the overburden stress ρgz at the depth of the crater bowl is small compared to the impact stress, and provided the region of crater formation is small compared to the target.

Once impact fragmentation has ended, and once the cratering flow has been established (Melosh 1989, pp. 46–51), the size of the target matters only insofar as its gravity resists and directs the excavation. One possible distinction is that the near-surface zone of loosely cohesive regolith that is largely unaffected by gravitational packing may extend more deeply on small bodies than on, say, the lunar surface, as discussed by Sullivan *et al.* (1996). The final, *evolved* shape of craters may vary on targets with different surface gravity, or on targets with appreciable coriolis accelerations such as Ida, but the fragmentation phase and the ejection phase can be treated as separate, simply-coupled events when gravity is small. In this paper we model the earliest moments of crater formation, and can offer predictions only with regard to approximate crater diameters, not their final profiles or shapes.

Strength versus Gravity

It has long been recognized that large objects are weaker than small objects composed of the same material. This was the original motivation behind Weibull's flaw distribution (Eq. (1)), used by him to explain why lumps of coal become more difficult to crush as they get smaller. Subdivide a rock into 100 equal pieces (along arbitrarily precise geometrical planes), and 99 of them are stronger than the original, owing to the simple fact that they do not contain the one weakest flaw. From Eq. (1) we have seen that the strength of rock decreases with size $R \sim V^{1/3}$ as

$$Y \propto R^{-3/m}. \tag{2}$$

Fujiwara (1982) and Farinella *et al.* (1982) suggested a size-dependent strength for asteroids of $Y \propto R^{-1/2}$, i.e., $m = 6$. For basalt (the rock whose material constants we adopt for this study, see Table I) $m \approx 9$, so that lowest failure threshold decreases with the cube root of the target dimension. A 10 km crater forms in basalt with minimum failure thresholds $(10^5)^{-3/9} = 0.02$ times as strong as the most likely thresholds local to a 10 cm laboratory crater. These are the minimum thresholds which activate under quasi-static tensile loads; there is in theory no maximum threshold, although in practice the Weibull distribution does not extend to sizes smaller than the grain size of the rock (~1 mm for basalt). Field tests in geologic settings (Grady and Kipp 1980) suggest that Eq. 1 remains valid to large scales, although recent studies indicate that size dependence may itself vary with size. Specifically, Fukushima (1990) suggested that m may range from 14 (for small samples) to 8 (for ~5 m objects) and may be as low as 2 for larger rock masses. In the latter case, Ida would be too weak to support its own topography.

Closely related to size dependence, from the point of view of flaw statistics, is the rate dependence of strength, which can lead to an order of magnitude variation in dynamic failure thresholds (Rinehart 1965). Rate dependence has an effect similar to size dependence (see Melosh *et al.* 1992, Asphaug 1993): large-scale events activate only the fewest, weakest flaws because the strain rate is low. Rate dependence is automatic in any model (such as a hydrocode) that nucleates Weibull flaws and allows each to relieve stress over a finite time governed by the crack growth velocity. For a uniform strain rate $\dot{\varepsilon}$, Grady and Kipp (1980) show that $Y \propto \dot{\varepsilon}^{3/(m+3)} = \dot{\varepsilon}^{1/4}$ in basalt and $Y \propto \dot{\varepsilon}^{1/3}$ in granite.

The gravity regime. Ignoring strength and assuming a semi-infinite target, gravity g is invariant, and the four remaining dependencies are reduced by the π-theorem to a single dimensionless relation. This results in a gravity scaling law (Housen *et al.* 1983) for the volume of crater ejecta V_e exceeding a velocity v,

$$\frac{V_e}{D^3} \propto \left(\frac{v}{\sqrt{gD}}\right)^{-e_v}, \tag{3}$$

where D is the diameter of the transient crater cavity and e_v is experimentally derived, as is the constant of proportionality. (The transient crater can be considerably smaller than the final crater due to collapse and slump of the walls.) This expression can be transformed (Asphaug and Melosh 1993) to show that for Ida, more than 80% of impact ejecta in any gravity-regime event are traveling slower than $v_{esc} \sim 18$ m s^{-1}. A multi-km crater on Ida therefore requires thousands of seconds to form.

Housen *et al.* (1983) furthermore show that the distance proximal ejecta travels scales with the diameter of the crater. This makes all gravity-regime craters geometrically similar in a half-space, and in principle easy to distinguish by the characteristic raised rims caused by ejecta deposition. There are complications of course. The presence of a rim does not uniquely define a gravity-regime event, since strength-regime craters can exhibit appreciable "bulking" due to an enhanced porosity in the fragmented region outside the crater. Intergranular friction governing soil stability increases with decreasing velocity, making bulking potentially more effective during slow ejecta flows on asteroids. On low-gravity targets, shaking near craters by subsequent impacts can also alter their appearances significantly.

Transition between strength and gravity regimes. If one assumes impactor density is the same as target density, and impact trajectory is normal to the surface, then the gravity-scaled impactor radius for a given crater may be derived from Housen *et al.* (1983) to be

$$r_g = 0.41\, D^{1.28} \left(\frac{g}{v_i^2}\right)^{0.28}. \tag{4}$$

The relationship between impactor size and crater size is not linear; a given population of impactors produces a population of craters with a flatter size distribution. The strength-scaled impactor required to produce the same transient crater in a zero-gravity half-space of fixed strength Y scales linearly with D:

$$r_s = 0.385\, D \left(\frac{Y}{\rho v_i^2}\right)^{0.28}. \tag{5}$$

Equating these expressions for impactor radius gives an estimate of the transition crater diameter, $D_{trans} \approx 0.80\ Y/g\rho$. The same impactor produces this size crater according to either scaling rule. Assuming a mean surface gravity of Ida ($\sim$1 cm s^{-2}), a density $\rho = 2.7$ g cm^{-3}, and a strength typical of geologic rock samples ($\sim 2 \times 10^8$ dyne cm^{-2}, Rummel 1987), the strength regime and gravity regime impactors are identical for crater diameters of 600 km. This implies that gravity scaling would never apply to Ida. If Ida is one hundredth as strong, then the predicted transition diameter is the size of Ida's largest craters. On the Moon, by comparison, g is more than two orders of magnitude larger, and density is somewhat greater, so the predicted transition crater diameter is less than 3 km for rock strength $Y = 2 \times 10^8$ dyne cm^{-2}, and for Earth, $\sim$500 m.

If one adopts the size-dependent strength of Eq. (2), this relationship changes so that for material constants typical of most rocks, gravity-regime craters can exist on low-gravity targets. Applying size-dependent strength to the scaling relation (Eq. (5)), we derive an expression for the transition diameter of a crater as a function of the Weibull exponent m and the "laboratory strength" Y_1, which we define as the average tensile strength of a 1 cm specimen of the rock. In cgs units

$$D_{trans} = \left(\frac{0.80\, Y_1}{\rho g}\right)^{m/(m+3)}. \tag{6}$$

This expression predicts a 7 km transition diameter on Ida for a laboratory strength of 2×10^8 dyne cm^{-2}. Craters of this size are few. For a different Weibull exponent ($m = 6$, typical of granite) but the same laboratory strength, the transition occurs at 1.5 km diameter. We do not know this parameter *a priori*; studies of asteroid landforms may allow its determination. The predicted transition crater diameter for the Moon, presuming $Y_1 = 2 \times 10^8$ dyne cm^{-2} and $m = 9$, is $\sim$120 m; for Earth, it is $\sim$30 m.

Implications for the cratering record. Applying Eq. (2) to Eq. (5) tells us that impactor size varies with crater diameter in the strength regime as $r_s \propto D^{1-0.28(3/m)} \approx D^{0.9}$ for basalt. Values as low as $m \approx 3$ (Ahrens and Rubin 1993) and $m \approx 2$ (Fukushima 1990) have been suggested, in which case $r_s \propto D^{0.72}$ or $D^{0.58}$. In any event, a given crater population implies a shallower impactor flux in the strength regime, not counting for other factors affecting the cratering rate, such as the masking of smaller craters by larger ones, saturation, or the degradation of pre-existing craters by seismic shaking from recent impacts (Greenberg *et al.* 1996). The opposite trend occurs in the gravity regime (Eq. (4)), where the size distribution of impactors is steeper, by a factor of 1.28, than the size distribution of craters, so particular care should be exercised in deriving impactor fluxes from the cratering record on small targets.

Material Parameters for Ida

For the purpose of our numerical models we must assume material properties for Ida. The mean density has been constrained by Dactyl's orbit (Belton *et al.* 1996) as $\rho \approx 2.6 \pm 0.6$ g cm^{-3}. Without speculating about Ida's composition, we adopt the Tillotson equation of state derived for gabbroic anorthosite from a study of lunar materials (Ahrens and O'Keefe 1977), and substitute the density, shear modulus μ, Weibull coefficients, and von Mises yield parameters determined in the laboratory for basalt (Nakamura and Fujiwara 1991; Benz and Asphaug 1994a). This choice of Weibull constants yields excellent agreement with fragment size distributions (Melosh *et al.* 1992) and fragment shapes and fracture planes (Benz and Asphaug 1994a,b) for laboratory impacts into basalt spheres and cubes. Because laboratory targets are machined from a homogeneous outcrop and are otherwise chosen for their uniform properties, they present a biased sampling of the intrinsic flaw distribution and hence a greater strength than is typical of the native rock. Ida is probably weaker than the material we model here. Adequate constitutive models and fracture constants have yet to be determined for more likely material candidates, such as chondrites or stones from our meteorite collections; having survived transport to Earth, however, meteorites present an even more biased flaw distribution. For reference, laboratory tensile strengths of several 10^8 dyn cm^{-3} are common for stony meteorites (Tsvetkov and Skripnik 1991).

Numerical Models of Small Craters

We now show that our numerical results agree with strength scaling predictions (modified by size dependence) until cratering efficiency suddenly increases for impactors larger than a few meters. Thereafter the diameter of the fractured region follows a curve scaled to a lower effective strength, although at this size gravity becomes the dominant force, even on Ida. This increased efficiency can be understood in terms of a boundary relation between the excavation flow and the expanding fracture cavity. The strength/gravity transition appears to correlate with the sizes of craters on Ida observed to be surrounded by bright annuli (see below).

We use the Lagrangian hydrocode SALE2D (Amsden *et al.* 1980) and the fracture damage scheme of Benz and Asphaug (1994b). This is the same versatile Los Alamos code that Melosh *et al.* (1992) adopted as the framework for their own impact fragmentation model; our fragmentation technique differs as described above. Impacts are modeled in axial symmetry, constraining the impactor to strike vertically. Another symmetry constraint is that radial fractures can only grow statistically in response to a hoop stress; i.e., damage is averaged over all 2π radians about the axis wherever radial cracks occur. Explicit radial cracks require 3D computations, but our 2D model computes crater size and overall damage beyond the crater in good agreement with 3D models and with laboratory data. Actual fragment shapes and crack trajectories in the far-field are not typically realistic in 2D, however.

The top boundary condition is a Lagrangian free surface, the symmetry axis is a simple freeslip, and the outer and bottom edges allow continuative outflow of wave energy, but not matter, thereby mimicking an infinite half-space. Continuative outflow makes it impractical to apply a gravity vector g, but by the time t_f that the stress wave departs from the grid, the velocity perturbation $\Delta v = g \times t_f$ is smaller than any relevant velocity, so gravity can be ignored. Gravity is important over the much longer timescale encompassing the evolution of crater ejecta, but we do not model this final stage of cratering. The overburden stress $\rho g z$ is negligible in these runs.

The stress wave responsible for fragmentation and crater excavation must be resolved in detail near the impact, but the same resolution is not required far from the crater. This permits us to use logarithmic grid spacing, with resolution falling off with a fixed power of distance. Specifically, we use $dr \propto r^{1.5}$ and $dz \propto z^{1.5}$ for the radial and vertical axes, respectively. Powerful stress waves broaden with at least this power of distance (Melosh 1989), so they are resolved throughout the calculation. With 50 × 50 cells, the finest resolution in our grid is the radius of the impactor, whereas the grid size is 600 times as large, enabling us to resolve the processes leading to the formation of the impact crater, and to study far-field stress wave phenomena.

The accurate treatment of shocks is essential. Shock dissipation governs the rate of energy deposition and the structure of the stress wave that emerges from the contact zone. Irreversible thermodynamics cause a jump in particle velocity behind the shock which establishes the cratering flow (Melosh 1985). We use an equation of state (Tillotson 1962) formulated specifically for the treatment of shock

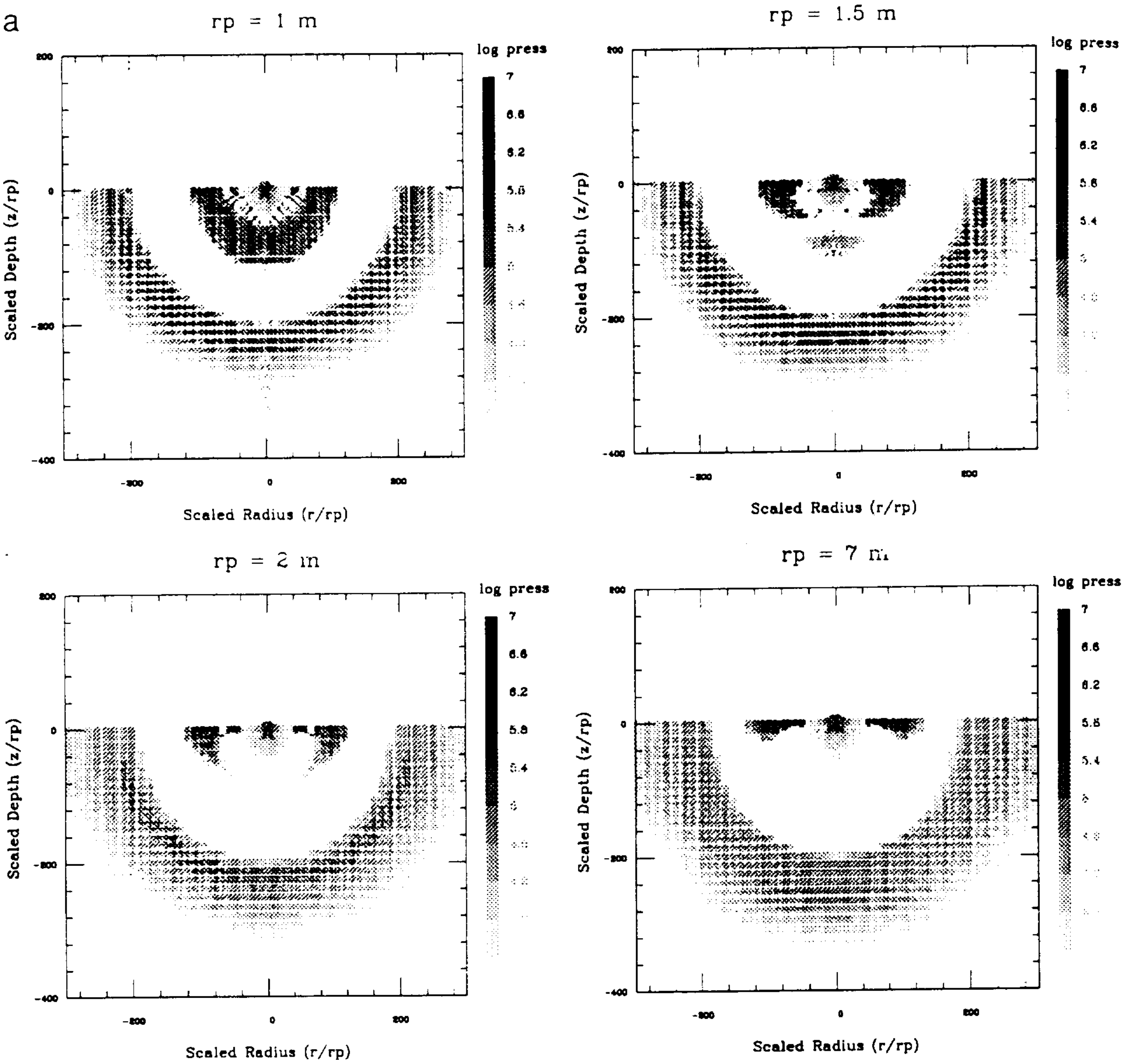

FIG. 1. Stress waves in a half-space generated by four different impactors (1, 1.5, 2, and 7 m radius) at 3.55 km sec^{-1}. These 2D plots of pressure are reflected about the symmetry axis and are scaled logarithmically from 10^3 to 10^7 Pa (10^4 to 10^8 dyn cm^{-2}). The axes are normalized to r_i and the plot times to r_i/v_i. (a) The shock wave halfway through the calculation, at 0.05, 0.075, 0.1, and 0.35 sec, respectively. Fragmentation is almost complete by this time. A second stress wave emerges for impactors smaller than ~2 m radius; it is caused by ejecta flow catching up with the rarefaction wave behind the main shock (see Fig. 3). (b) Pressures at the end of the simulation, at scaled times 0.1, 0.15, 0.2, and 0.70 sec, shaded to the same scale as before but now showing the entire grid. Note the transition in secondary wave structure.

waves generated during impact events and "point source" explosions; more accurate (and complex) equations of state are available for certain materials, although given what little is known about Ida, their use is not warranted here.

We performed eight high-resolution (50 × 50) simulations for impactors ranging in radius from r_i = 1 m to r_i = 30 m, corresponding to fracture-zone diameters from several tens of meters to several tens of kilometers (Figs. 1 and 2). Impactor size is varied by a proportional scaling of the grid. Each calculation begins at the moment of impact, with the projectile penetrating the target at v_i = 3.55 km sec^{-1}, the estimated average impact speed into Ida

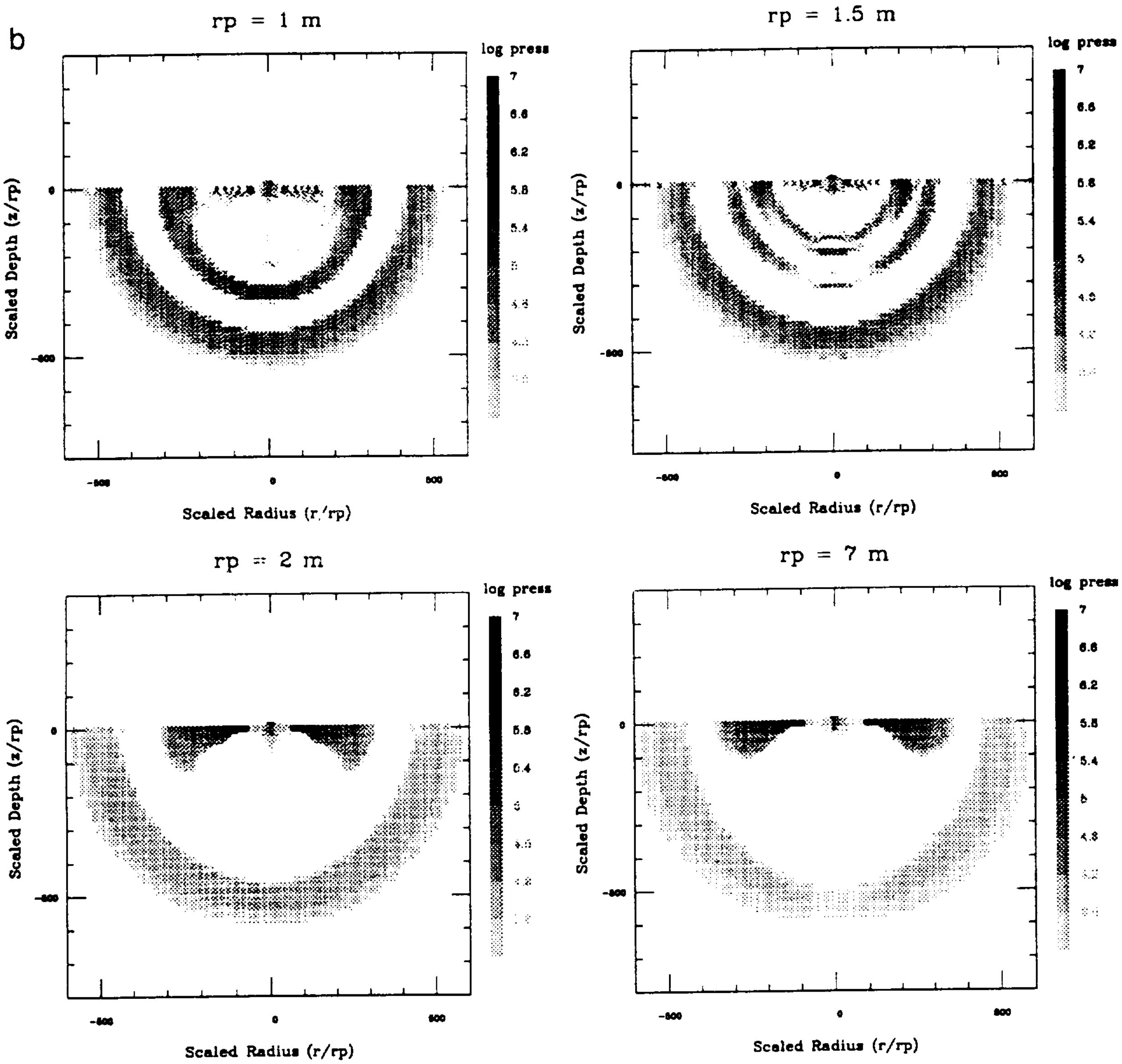

FIG. 1—*Continued*

(Bottke *et al.* 1994). Contact and compression (Melosh 1989) is completed by a few times r_i/v_i, followed by shock melting and vaporization in the contact zone. Shock waves in rock tend to form at pressures exceeding $\sim 10^{11}$ dyne cm^{-2} (Stöffler 1972); such pressures extend only to the immediate vicinity of the projectile at this modest impact speed. Yet so long as rate-dependent mechanisms such as fracture take place, the wave remains nonlinear and dissipative, dynamically modifying the material through which it propagates. Much experimental and theoretical research in this area comes from the defense industry, yet the phenomenon of stress wave attenuation in the free field of nuclear explosions, for example, continues to resist interpretation (Minster *et al.* 1991).

In the following analysis we emphasize the stage of cratering related to brittle fragmentation and fracture, since that is where our code differs from existing calculations (e.g., O'Keefe and Ahrens 1993). We do not model the final resting place of the ejecta; for this reason we speak of "fracture zone" instead of "crater," although both refer to the same thing if gravity is sufficiently small. Much of the fracture damage in the crater bowl is caused by

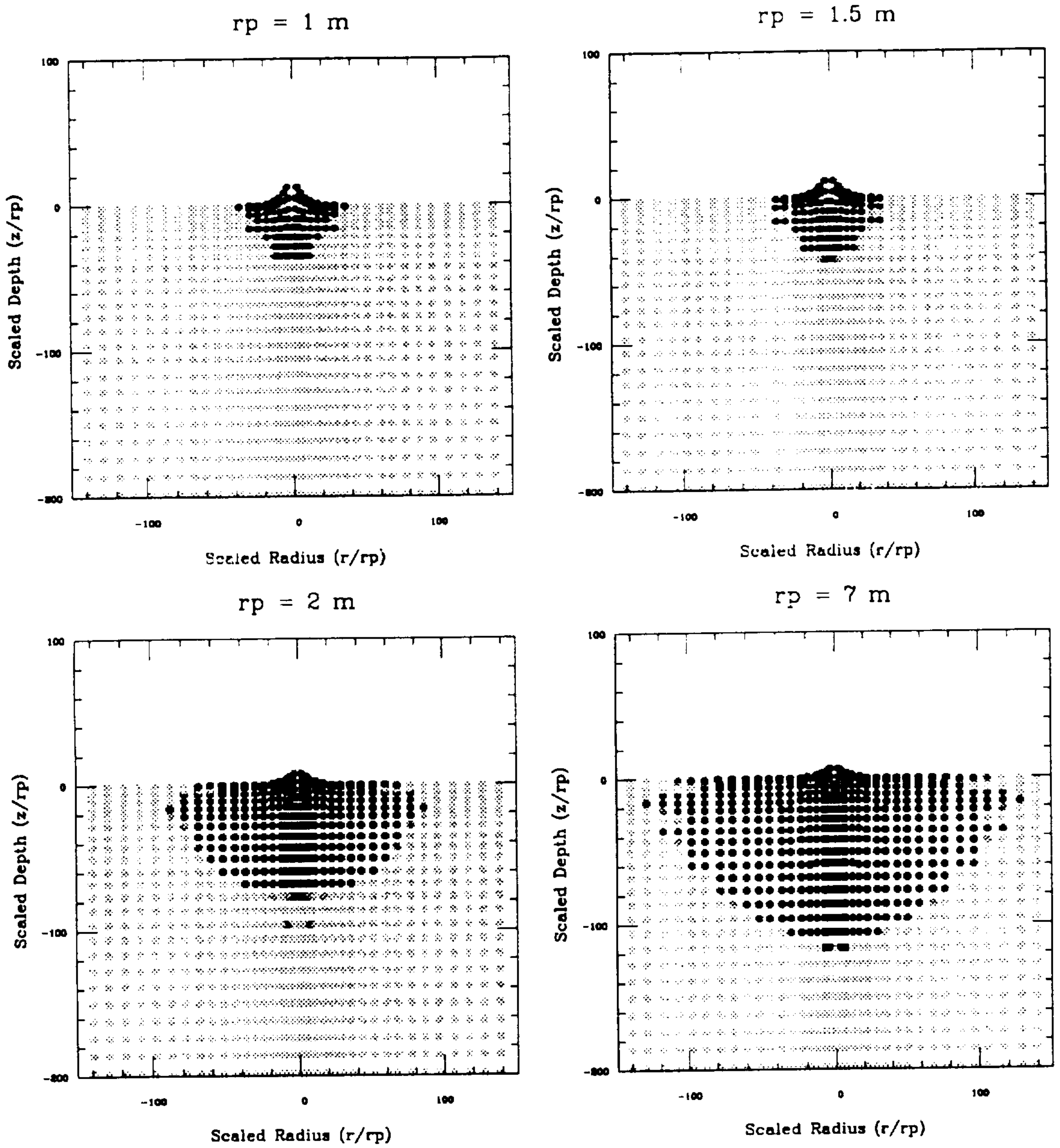

FIG. 2. A close-up view of the final damage in the simulations of Fig. 1. The diameters of the upper two craters match strength scaling predictions, when one allows for size-dependent strength. Note the sudden jump in cratering efficiency for impactors between 1.5 and 2 m in radius.

rarefaction (the "tail") following the compressive shock into the target. This process was examined directly by Fourney *et al.* (1984) with polarization images of stress orientation during fracture. Related to this mode of fragmentation in our model is an enhanced cratering efficiency beyond a certain impactor size.

2D halfspace results. All calculations end at the same scaled time $t_f = 355 r_i / v_i$, or 0.1 sec for the 1 m impactor and 3.0 sec for the 30 m impactor. Target material (Table I) and impactor speed are the same for all runs, although larger slabs contain weaker flaws by virtue of Eq. (1). Figures 1a and 1b show the stress wave (contours of pressure) caused by impactors with radii r_i = 1, 1.5, 2, and 7 m, at $t = t_f/2$ and $t = t_f$. Figure 2 shows final damage at $t = t_f$ for these events. Pressure in the primary wave is approximately invariant with changes in scale; it decays

TABLE I

Material constants for basalt Ida model

Reference density	ρ_0	2.70 g cm^{-3}
Bulk modulus	K	2.67×10^{11} dyn cm^{-2}
Shear modulus	μ	2.27×10^{11} dyn cm^{-2}
Plastic yield stress	Y_o	3.5×10^{10} dyn cm^{-2}
Weibull flaw	m	9.0
distribution constants	k	5.0×10^{24} cm^{-3}

Tillotson equation of state parameters
(see Melosh, 1989, pp. 233–234 for definitions)

B	2.67×10^{11} dyn cm^{-2}	β	5.0
a	0.5	E_o	4.87×10^{12} erg g^{-1}
b	1.5	E_{iv}	4.72×10^{10} erg g^{-1}
α	5.0	E_{cv}	1.82×10^{11} erg g^{-1}

Derived constants

Longitudinal wave speed	c_l	4.59 km sec^{-1}
Shear wave speed	c_s	2.90 km sec^{-1}
Crack growth velocity	c_g	1.84 km sec^{-1}
Young's modulus	E	5.31×10^{11} dyn cm^{-2}

approximately invariant with changes in scale; it decays with a power of scaled distance r/r_i (e.g., Melosh 1989, Rodionov *et al.* 1972). Damage has virtually ceased by $t = t_f/2$, so that remaining wave propagation occurs in an elastic medium.

Note the strong secondary compressive pulse following the primary wave for the 1 m impactor, a less coherent secondary pulse for the 1.5 m impactor, and its absence for impactors 2 m in radius and larger. In conjunction with the disappearance of this second wave, a jump occurs (Figs. 2) in the normalized diameter of the fractured region. The transition, at least for basalt at this impact velocity, corresponds to fractured zones between 100 and 200 m diameter and impact energies approaching 1 kiloton (4.1×10^{19} erg). In a number of nuclear weapons tests (e.g., Perret *et al.* 1967) a second wave radiates a fraction of a second after the first, with a peak acceleration about one-fifth as large as the first, which correlates reasonably well in both timescale and magnitude with what we observe in our simulations. (This second wave must not be confused with the spall signal, which is a reflection of the primary wave in an underground event from the free surface.) Direct comparison with nuclear tests is no simple matter because most data pertain to buried explosions rather than craters, and because material type is limited. The "Salmon Event" which Perret *et al.* (1967) describe, for instance, took place in a Mississippi salt dome. Reliable free-field measurements are generally difficult to come by, and in any case the absence of impactor momentum is probably significant at the relatively low velocities considered for Ida.

To understand this second wave, and the transition in cratering efficiency, we construct radial pressure profiles (Fig. 3) which show that for sufficiently small impactors this secondary compressive wave overtakes (and cancels) the tensile "tail" behind the primary wave, thereby hindering further fragmentation. We have not yet explored how this phenomenon depends on impactor velocity or on target parameters such as sound speed and strength. For the 1 m impactor, Fig. 3a shows the stress wave together with its rarefaction at 0.03, 0.04, 0.05, and 0.06 sec. (The bottom left frame of Fig. 3a corresponds to Fig. 1a; scatter in the pressure profile is due to stochastic failure thresholds, free surface interactions, and a small numerical spike along the symmetry axis.) Fragmented material accelerated by the shock (flagged with thin diagonal lines in the figure) launches the secondary compressive wave when it overtakes material in front of it; because damage does not reduce the bulk modulus for compression, this wave overtakes the rarefaction.

Figure 3b shows pressure profiles at the same scaled times (0.21, 0.28, 0.35, and 0.42 sec) for the 7 m impactor. The initial wave looks similar to the first; it is somewhat broader because of size and rate effects. But the next three frames reveal dramatic differences which explain the enhanced cratering efficiency. The mean velocity in the cratering flow is only half as great, according to our calculations, and the flow evidently never overtakes material in front of it, at least not at relative velocities high enough to launch a wave, until after fragmentation has ended by normal attenuation. Scale-similarity apparently breaks down because the cratering flow is emplaced at slower speed for larger impactors, whereas the primary stress and the rarefaction travel at the same rate regardless of size. We find support for this trend in a recent analysis by Housen and Schmidt (1995) of ejecta velocities and rate-dependent strength, although their work predicts a 25% reduction in flow velocity between these two cases instead of the 50% drop we observe for our choice of $m = 9$.

Comparison of numerical and scaling results. Figure 4 plots the diameter of the totally damaged region for each run (those of Figs. 1 and 2, plus a number of other impactor sizes) as well as the gravity-scaled and strength-scaled predictions for crater diameter, assuming a constant impact velocity of 3.55 km sec^{-1}. For strength scaling we incorporate size-dependence (Eq. (2)) into Eq. (5) and assume a laboratory strength of 2×10^8 dyn cm^{-2}. For comparison, we have plotted gravity-regime predictions (Eq. (4)) for Ida gravity and lunar gravity. (We assume for comparison the same impact velocity on both bodies; lunar impact

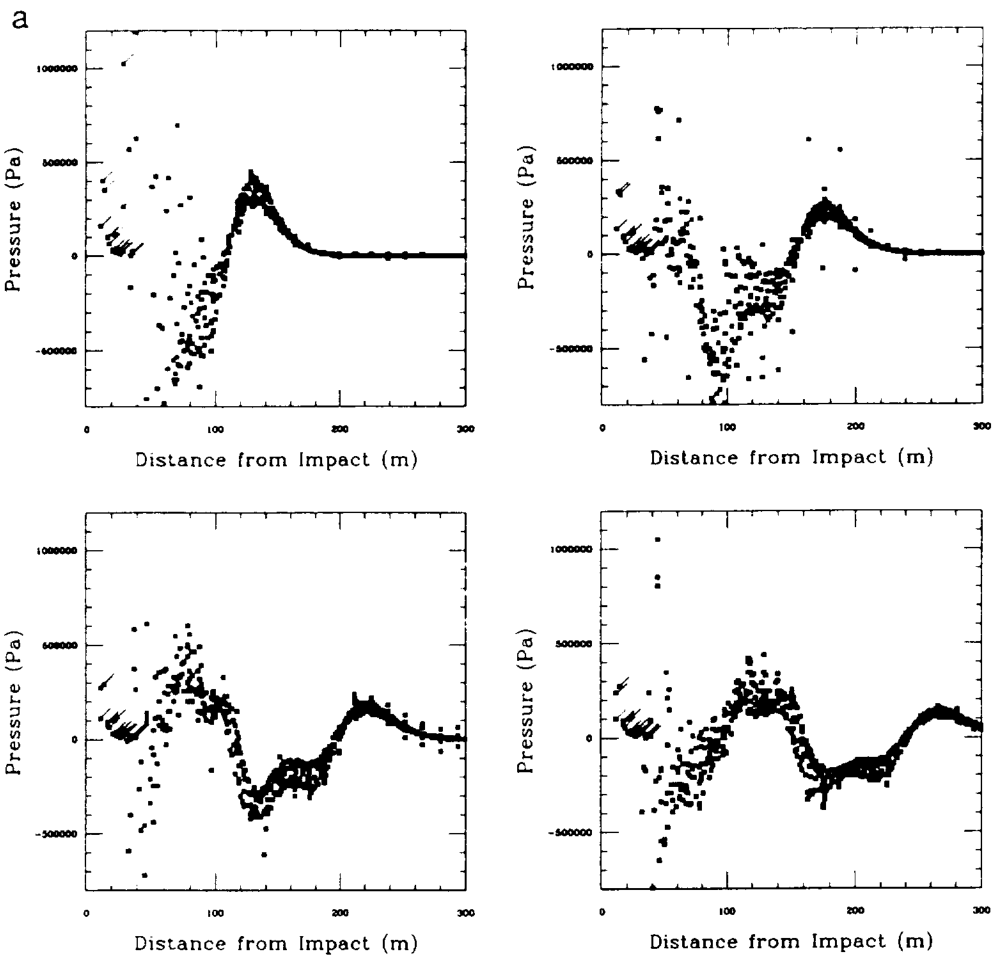

FIG. 3. Radially averaged pressure profiles for the smallest and the largest cratering impacts in Fig. 1. The maximum pressure decays with a power of distance somewhat less than 2, in approximate agreement with underground nuclear experiments (Perret *et al.* 1967; Rodionov *et al.* 1972). The compressive stress tends to be radially symmetric, whereas the tensile "tail" suffers a more heterogeneous dispersion. The ejecta flow, accelerated by the main shock, consists of totally damaged material marked by the small diagonal flags. Most of the flow is at low pressure. (a) For the 1-m impactor, the ejecta flow launches a secondary compressive wave which catches up to, and cancels, the tail behind the main shock (see text). This wave cancellation causes fracture to end prematurely. (b) Stress wave evolution for the 7-m impactor is not scale-similar to the previous example. The ejecta flow is significantly slower than before, as dictated by the lower strain rate (Housen and Schmidt 1996) for the larger impactor. Consequently, the flow does not launch a secondary compressive wave, and the tensile tail proceeds to cause a greater relative amount of fragmentation.

speeds are actually more than twice as fast.) Size-dependent strength scaling fits the numerical results for the diameter of the fracture zone rather well for impactors up to 1.5 m in radius (craters up to about 100 m in diameter), considering that the actual crater diameter must be somewhat smaller than the fracture zone. Following the jump in cratering efficiency just described, fractured regions larger than 1 km diameter once again grow parallel to the strength-scaling curve, but correspond to an effective strength about one order of magnitude lower; this is due to the resumed validity of dimensional equivalence.

The diameter of the totally fragmented region produced in our simulations (solid curve) will not change if this analysis is applied to a different planet composed of the same rock. Nor will the dotted line change for the strength-scaling prediction. The gravity scaling line moves to smaller craters (to the left) for higher gravity, so that a crossover between gravity-dominated and fracture-dominated excavation occurs for lunar crater diameters ~120 m according to Eq. (6) or ~90 m according to our simulations, although rate-dependent effects due to higher impact velocity on the Moon have been neglected. An increased fragmentation efficiency producing fracture zones larger than 100 m is not likely to affect sizes and morphologies of lunar craters.

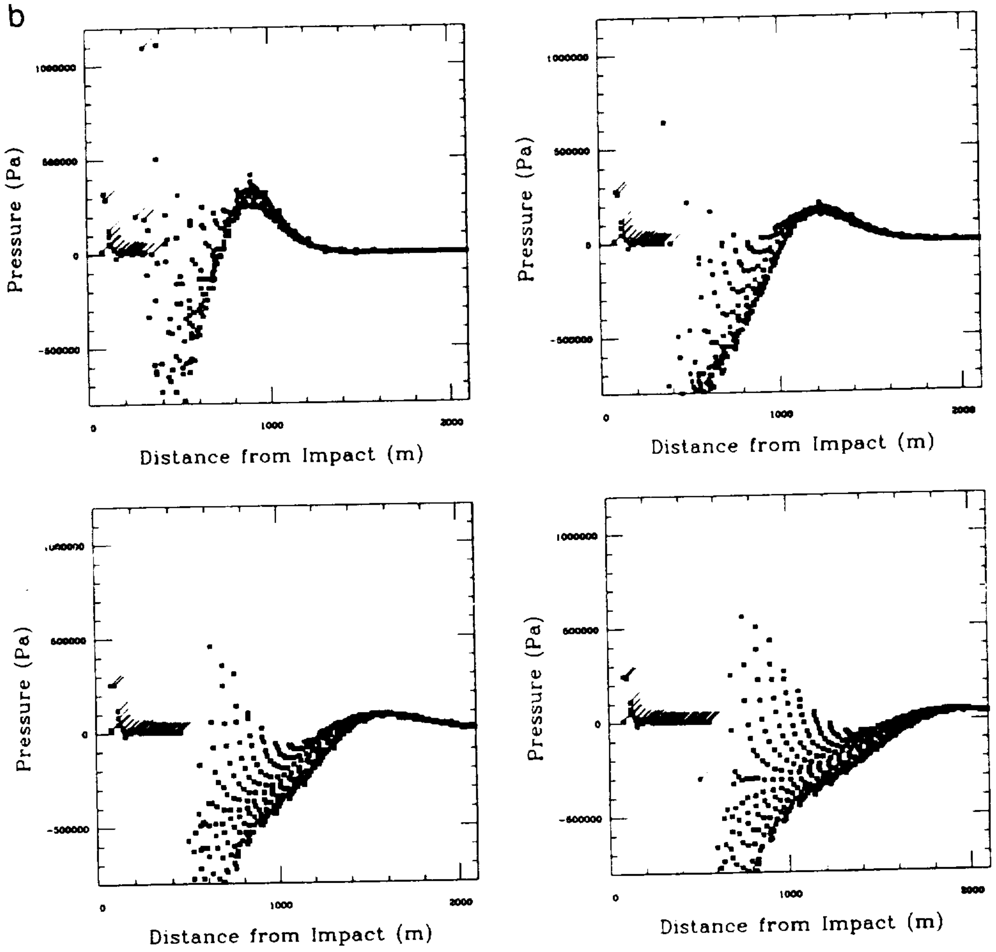

FIG. 3—*Continued*

An exciting promise of asteroids is the evidence they might reveal about impact and cratering mechanics, masked by high gravity on other worlds.

Proximal Velocities: A Model for Bright Annuli

For Ida, the diameter of the totally fragmented region (solid line in Fig. 4) crosses the gravity-scaled crater diameter at 600 m, considerably smaller than Eq. (6) predicts because of the increased cratering efficiency. This leads us to consider whether a number of craters in this size range on Ida which possess "bright annuli" may be related to strength effects. This class of craters is marked by typically undegraded morphology, bright materials in their cavities, and a bright zone surrounding them. The boundaries of these bright annuli appear irregular in some images and are often biased by pixel size or oblique viewing geometry, but to first order the term "annulus" is appropriate, in contrast to impact ejecta rays which exhibit extreme variation in radial distribution about their host crater (see Figs. 3, 4, and 7 in Sullivan *et al.* 1996). We plot the normalized diameters of several well-resolved bright annuli against their corresponding crater diameters in Fig. 5. Because bright annuli are expected to begin degrading to background characteristics the moment they are formed, the annuli we measure might be smaller than their initial diameters; we looked for the widest and most distinct annuli for each size range in order to construct Fig. 5.

Because small craters are generally the youngest, an apparent trend towards broader bright annuli (relative to crater diameter) around small craters could be attributed to evolved degradation about older, larger craters, or to the small statistics of large cratering events. In this view, bright annuli are gravity-regime *deposits* which have eroded from around larger craters and are seen around

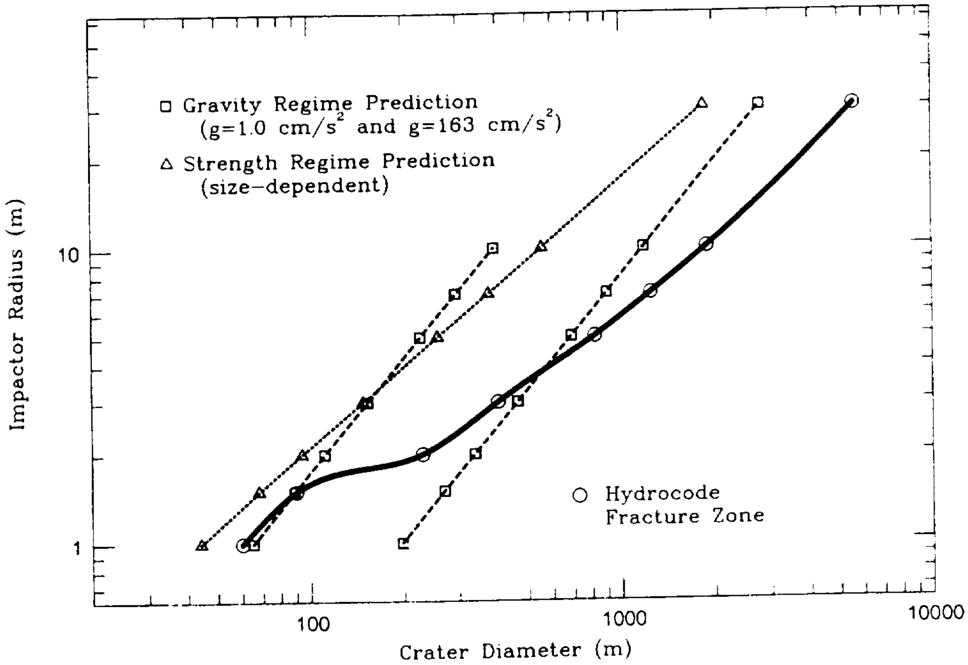

FIG. 4. We measure the diameters of the totally damaged regions for the outcomes plotted in Fig. 2. as well as the outcomes for other, larger impactors, and compare the outcomes of the hydrocode (solid line) with the predictions of strength scaling (dotted line) and gravity scaling (dashed lines for Ida and the Moon). The diameters of the fracture zone fall close to the line of the strength scaling prediction for the first two craters. The 2 m radius impactor causes considerably more damage, and the 5 m impactor damages a region larger than the gravity-scaled crater. This latter impactor would therefore produce a ~1 km crater controlled by gravity on Ida.

smaller craters simply because of their relative youth. There are a number of inconsistencies with this otherwise economical explanation. Presume that bright annuli all begin with approximately the same width and thickness relative to crater diameter—i.e., that they are scale-similar gravity regime deposits. If that is the case, then the lifetime of an annulus divided by the lifetime of its crater will be approximately constant if the rate of annulus erosion depends on size to the same degree as the rate of crater erosion. If the annuli are depositional, and if they are removed by the same impact erosion process which removes craters (and are not merely covered or weathered), then the relative states of annulus degradation and crater degradation should remain constant regardless of scale. Because larger craters are more completely within the gravity regime, their ejecta deposits should be relatively thicker, and their annuli should thus survive even longer, in contrast to observation.

If the process of annulus degradation is due to a different mechanism than mass removal by impact, we cannot presume this similarity. But if annulus degradation is a distinctly near-surface weathering phenomenon (Sullivan *et al.*, this issue), we are at a loss to explain why annulus degradation would mask bright deposits from the outside in, leaving a narrow unweathered circle around the largest, oldest bright annulus craters. Near-surface weathering will darken the annuli uniformly, regardless of the thickness of the presumed bright deposit. A third difficulty with a depositional origin relates to evidence that bright annuli may extend to sizes near the limits of image resolution. For sub-100 m craters to form in the gravity regime (required if they are to be surrounded by copious ejecta) they must be excavated from zero strength material (loose regolith) by impactors a few tens of cm across, and not in the strength regime by impactors several m in radius (Fig. 4). The problem here is that bright deposits should scale with the flux of cm-scale impactors, making Ida fresh and bright all over. All of these factors taken together argue against a depositional origin for bright annuli.

We propose instead that the trend of broad bright annuli about numerous small craters, thin bright annuli about a number of craters in the ~300 to ~600 m range, and their absence about larger craters is, at least in part, a direct manifestation of near-field *ejection* related to strength-dominated impacts. In essence, we propose that a bright annulus is created when a velocity field is established in rock which does not suffer total failure, a process comparable to the formation of spallation rings beyond the rims

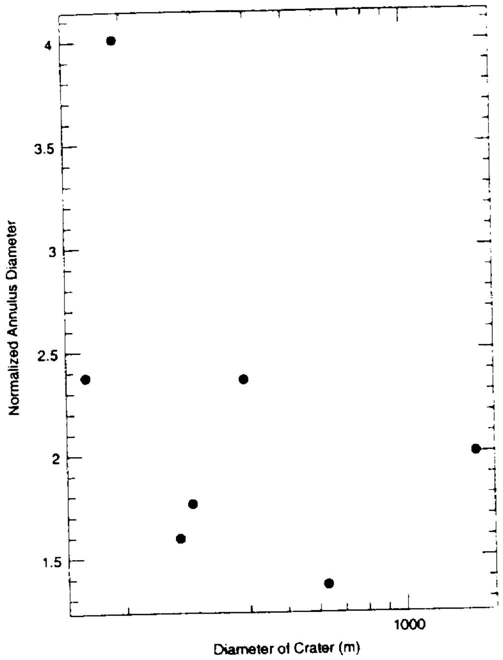

FIG. 5. The diameters of several typical bright annuli, normalized to the diameter of their corresponding crater, plotted as a function of crater diameter (Sullivan *et al.* 1996). In many cases the width of the annulus is constrained by pixel resolution, so these numbers are approximate.

of small-scale laboratory craters (see Melosh 1989, p. 15). The velocities involved here are considerably smaller, however, and actual spallation is not required since loose material is presumed to exist already on the surface.

To create a bright annulus, the impact stress wave must be powerful enough to disturb loose surface materials, but not so powerful as to totally fragment and excavate the rock. An ejection mechanism for bright-annulus craters is therefore biased towards small rocky targets, where strength may be of the same order as on the Moon, but where comparable ejecta velocities transport material ~200 times as far. Lunar craters the size of Ida's bright annulus craters are gravity scaled, and any proximal regolith disturbances get covered by ejecta. Bright areas surrounding young lunar craters of the Copernican period are certainly depositional. Smaller lunar craters would result in seismic disturbance in a comparable annulus, but the degree of ground motion would be much less than on Ida. A rare (and apparently undocumented) example of such a process occuring on Earth, analogous to our proposed mechanism for bright annuli on Ida, is the subtle brightening of cliffs near the 1.3 megaton underground nuclear explosion Boxcar in Pahute Mesa, Nevada. Fractured cliff blocks broke away which had been loosely cemented by white carbonate deposits. Within a couple of years the exposed caliche had washed away, and the cliffs resumed their normal appearance.

In Fig. 6 we compare bright annulus diameters with the radial distance to which surface velocities exceed a given speed in our 2D hydrocode results. These zones are smaller for higher velocity, since the greatest speeds occur proximal to the crater. The upper curve plots the extent of surface velocities exceeding 1 cm s^{-1}, the middle curve shows velocities exceeding 10 cm s^{-1}, and the lower curve shows velocities exceeding 1 m s^{-1}. These velocities correspond on Ida to ballistic trajectories of ~1 cm, ~1 m, and ~100 m, respectively. There is a sharp drop-off in this distance between crater diameters 100 to 300 m, corresponding to the enhanced cratering efficiency for large events.

We can infer the particle velocities responsible for bright annuli by plotting their measured diameters, normalized to their corresponding crater diameter (Fig. 5), on the same diagram (black triangles). A reasonably good correlation exists between the bright annulus data and the proximal velocity curves for velocities between 10 cm sec^{-1} and 1 m sec^{-1}. Because measured annuli may be smaller than their pristine diameters, the data should be moved upwards; given that we probably observe *some* youthful craters, an upper bound probably falls between the 1 and 10 cm sec^{-1} curves, implying that transport distances of order ~10 cm are required to produce the brightening. (The same particle velocities on the moon would move material less than 1 mm.) This length scale is much smaller than the depth of regolith on Ida (Sullivan *et al.*, this issue), yet greater than the depth to which material is darkened by space weathering. It may represent the average motion required to shake off a thin, optically altered surface veneer.

Our explanation for bright annuli does not require the jump in fragmentation efficiencies derived from our numerical models. But for the gravity regime to begin for ~1 km craters by conventional strength scaling arguments (Housen *et al.* 1983), the mechanical strength of Ida could be no more than half a bar, which is at odds with Ida's ability to support dramatic topography. (Ida's maximum internal stress is several bars.) A size-dependent strength (Eq. (6)) makes matters worse: the larger volume of Ida must be even *weaker* than the crater volume, less than 0.1 bar. If the enhanced cratering efficiency modeled by our code applies, then the gravity regime transition can occur for ~1 km craters on Ida with a size-dependent strength of 2 bars, approximately equal to its maximum topographic load.

IV. LARGE CRATERS

Since the largest craters produced by the simulations just described are comparable to the size of Ida, they must

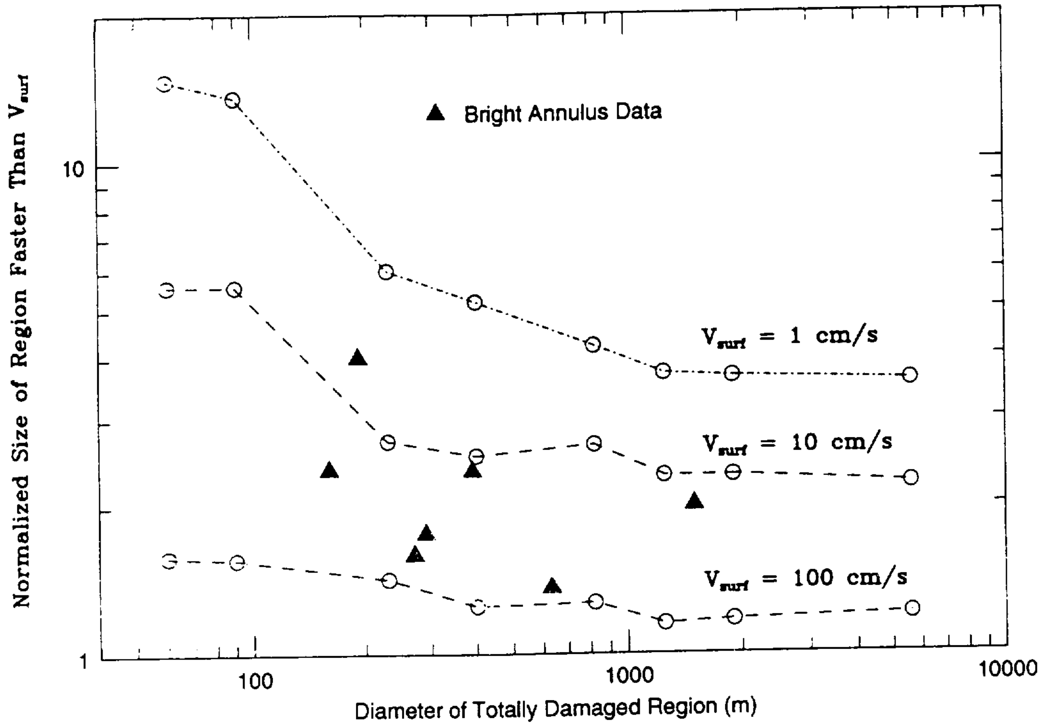

FIG. 6. For the runs plotted in Figs. 1–4, we measure the maximum distance to which a given velocity was achieved on the surface at any point during the calculation. In other words, surface materials inside these diameters were launched at velocities exceeding 1 m sec^{-1}, 10 cm sec^{-1}, or 1 cm sec^{-1}, depending on the curve, corresponding to ballistic trajectories on Ida of 100 m, 1 m, or 1 cm. This log–log plot shows that small craters forming in bedrock (1) have much higher velocities near the rim than large craters, and (2) influence the ground motion outside their bowls to a proportionately much greater extent than large craters. When the data of Fig. 5 are plotted on this diagram (triangles), there is a reasonably good correlation between the formation of bright annuli on Ida and a ground motion between 10 and 100 cm sec^{-1} (*i.e.*, trajectories ~10s of meters) proximal to a crater forming between the strength and gravity regimes.

be modeled differently to have any meaning on this asteroid. The target has significant curvature over this distance, and instead of vanishing to infinity, the impact stress encounters the target boundaries. Self-gravitational compression might conceivably hinder fragmentation at depth. The ejection phase is also complex on small targets, since crater ejecta may be launched several asteroid radii away, beneath a body whose rotation period might be comparable to the ejection timescale (Geissler *et al.*, this issue). Modification processes, such as the slumping of walls of the transient cavity to form the final crater, might exhibit dramatic asymmetry where surface gravity can vary by a factor of 2 or more over the diameter of a crater, and point in various directions. The final shapes of large craters on asteroids may be markedly different from their symmetric counterparts on sizable, spherical planets.

Grooves seem common on small planetary bodies, and are probably related to the formation of large impact structures. Phobos and Gaspra have gooves (Thomas *et al.* 1979, Veverka *et al.* 1994) and so does Ida. Although a number of ideas have been put forward to explain the grooves on Phobos, including the influence of Martian tides (Weidenschilling 1979) and gouging by slow-moving ejecta from Stickney (Wilson and Head 1989), their discovery on bodies in free space limits our range of hypothesis. The idea of impact-related stresses opening up extensive fracture grooves on Phobos was first explored in detail by Fujiwara (1991), and later by Asphaug and Melosh (1993) with a 2D numerical model similar to the one used here, and then by Asphaug and Benz (1994) who used a 3D smooth particle hydrodynamics simulation of the best-fit triaxial ellipsoid. The 3D study in particular showed how such an impact causes damage local to the crater, and comparatively little damage in the interior, and then a renewed episode of damage in the far hemisphere.

2D Models of Finite Targets

We model large impacts in 2D by making all boundaries free surfaces with the exception of the symmetry axis. A

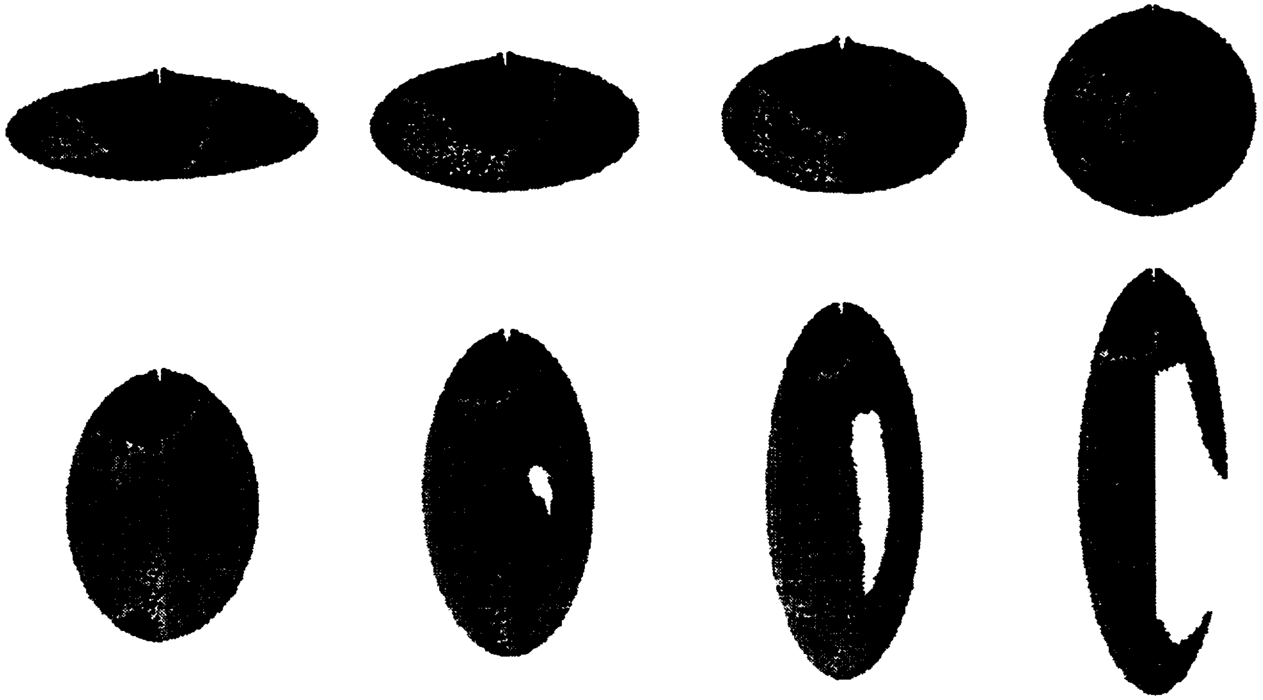

FIG. 7. Eight ellipsoidal targets of equal mass after impact by identical 7×10^{13} g projectiles at 3.55 km sec^{-1}). The mean radius of each ellipsoid is 16 km, approximately the same as Ida. Axis ratios are 1:3, 1:2, 2:3, 1:1, 3:2, 2:1, 5:2 and 3:1, from upper left to lower right. The left halves of the figures (slices down the symmetry axis) show fragmented regions ($D = 1$) as black, and intact rock ($D = 0$) as grey. The right halves show speed, from 0–1 m sec^{-1} (white), 1–2 m sec^{-1} (light grey), 2–3 m sec^{-1} (darker grey), 3–4 m sec^{-1} (darkest grey), and 4 m sec^{-1} and above (black). The net momentum imparted to the non-escaping fraction is quite small, as shown in Table II for related calculations. The profile of the damaged region flattens as the target radius of curvature decreases, implying a flatter final crater profile. Antipodal effects are minimal for slightly oblate or spherical targets which lack a geometrical focus at the antipode. Ida can be very roughly approximated as an ellipsoid between the two figures at the bottom center.

rectangular mesh with uniform grid spacing is first distorted into a hemisphere which is symmetric about its axis. This hemisphere is distorted by making $dr > dz$ or $dr < dz$ in the initial rectangular grid; upon rotation about the symmetry axis it becomes an oblate or prolate ellipsoid, respectively. A local overburden $P_{\mathrm{o}} = \frac{2}{3}\pi G\rho^2(R^2 - r^2)$, which achieves a maximum of ~2.5 bars at Ida's center ($r = 0$) and is zero at the surface ($r = R$), is added as a symmetric stress term to each fracture threshold (Eq. (A12)) at the start of the calculation. Impact stresses must first exceed the overburden, and then the local strength, to open a crack. We can neglect the dynamical effects of gravity for the same reason as before: the action of the stress wave is finished in about 10 to 20 sec, by which time gravitational acceleration has had negligible time to act.

To test the general effects of target shape on large impacts, we set up the eight hydrocode grids shown in Fig. 7, each with the same approximate volume as Ida (mean radius ~16 km) and the same constitutive model as before (Table I). We struck them with identical impactors $r_{\mathrm{i}} = 183$ m at $v_{\mathrm{i}} = 3.55$ km sec^{-1}. We ran the code to 50 sec after impact, about 10 wave crossing times. The ratio of the symmetry axis to the equatorial diameter for each case was 1:3, 1:2, 2:3, 1:1, 3:2, 2:1, 5:2, and 3:1. The best-fit triaxial ellipsoid to Ida measures $29.9 \times 12.7 \times 9.3$ km (Thomas *et al.*, this issue); the best-fit ellipsoid of revolution has axis ratio close to our 5:2 run. In axial symmetry all impacts must strike along the axis.

In the most oblate (1:3) target, the impactor causes fracture damage throughout the interior, and causes spallation on the antipodal surface. Since antipodal spall velocities are only ~1 m sec^{-1}, this material travels only a few 100 m. Antipodal spallation becomes less important for less oblate targets, and is scarcely evident for the sphere, which suffers "core-type" fragmentation, i.e., cracking around an interior concentric surface, commonly observed in laboratory impact experiments (Nakamura and Fujiwara 1991). For prolate ellipsoids (Figs. 7e–7g), antipodal fracture once again becomes important, even as the antipode becomes more distant. The reason is that a prolate ellipsoid has two foci, and if impact energy emanates from one focus it will interfere constructively at the other focus, in a

manner analogous to a whisper gallery (only more violent). For this large impactor, the effect is most pronounced for the 3:2 and 2:1 targets. Ida evidently has a geometry amenable to this type of focusing. The antipodal fractures in the most prolate targets are generally caused by hoop stresses which circle the axis of symmetry. Fractures caused by hoop stress are oriented in a direction that projects parallel to the symmetry axis, pointing longitudinally back to the crater. As was the case before, radial fractures cannot be modeled explicitly in an axially symmetric calculation, since the hoop direction $r\theta$ is not a free dimension. As a result the hydrodynamics are skewed in these regions of sparse fragmentation, and the actual crack orientations are not realistic.

Crater shape and target curvature. Many circular concavities observed on asteroids do not resemble traditional craters; we believe that this is entirely consistent with their impact excavation on a small target. Besides the effect of irregular gravity, the shape of the damaged region appears to depend on the target radius of curvature. The profiles of the fracture zones in Fig. 7 become increasingly flat as one moves from oblate to prolate targets. The right half of each image contours the maximum speed achieved during the calculation, with a contour interval of 1 m sec^{-1}. The bulk of the material inside of the fractured region is moving with velocities as low as 2–5 m sec^{-1} (compared to an escape velocity of ~18 m sec^{-1}), so we cannot hazard a further guess as to where the ejecta might land (dictating the final crater shapes). If all else is equal, however, a flatter fracture cavity will result in a flatter final crater. We infer from gravity scaling that for a surface gravity of 1 cm sec^{-2}, these impactors would excavate a 12 km crater in a half-space.

3D Models of Specific Large Impacts on Ida

Ida is poorly represented as a prolate ellipsoid (Thomas *et al.*, this issue). For this reason we now take a novel approach and construct a hydrocode grid directly from the topographic shape model in 3D. We employ the smooth particle hydrodynamics code SPH3D developed and tested extensively by Benz and Asphaug (1994a,b) and used by Asphaug and Benz (1994) to study the formation of fracture grooves on Phobos. The fragmentation model is the same as in the previous section). For symmetric cases the two codes have proven to yield approximately identical results. For a review of SPH see Benz (1990).

The geometrical procedure of creating a realistic Ida target is straightforward: we set up a cube of SPH nodes ("particles") in hexagonal closest packing, and then exclude all particles exterior to a surface map (see Fig. 2 of Thomas *et al.*, 1996). The same method as before is used to compute an approximate overburden stress, and all physical parameters are the same (Table I). We use this grid to model three of the largest impacts into Ida, and to learn whether grooves on this asteroid can be linked specifically to any of these events. For the first simulation the target is modeled with 70,000 particles, near the upper limit of resolution achievable on a modern workstation; for the two others the resolution is 35,000 particles, at the lower limit adequate for resolving the impact physics in 3D. Our physical model would be far more accurate at the scale of groove formation were we able to represent Ida at twice the linear resolution, i.e., with eight times as many particles, but such a run would require several hundred hours of cpu and ~300 Mb of core memory on a supercomputer. As it is, the following runs each take weeks of full-time cpu on a 96 Mb R4400 workstation. Table II provides the relevant initial conditions for these three runs.

FIG. 8. Three images of Ida showing the 12–15 diameter circular concavity Vienna Regio (centered 10°N, 5°E). The periphery is indicated by arrows.

TABLE II
Parameters and Results for the Four Impact Runs Done in 3D

Target	Surface g at target (cm sec^{-2})	Impactor radius (m)	Resulting crater diameter (km)	ΔV to Ida (cm s^{-1})	Δ_{rotation} to Ida (revs hr^{-1})
Vienna Regio (circular concavity)	0.7	165	~12	0.4	10^{-4}
Azzurra	1.0	150	~10	0.18	10^{-4}
Orgnac	0.8	125	~9	0.015	1.5×10^{-4}

Effects of the Vienna Regio Impact

The ~12–15 km diameter Vienna Regio concavity (centered 10°N, 5°E, near Ida's axis of elongation) does not resemble a traditional crater (Fig. 8). It lacks a distinct rim, and it lacks the symmetric profile we usually associate with impact craters. But the structure is certainly consistent with the formation of a crater in the gravity regime on a gravitationally complex, irregularly shaped, rapidly rotating body. Parallel to sub-parallel sets of well-resolved linear features, in the form of linear troughs and lines of coalescing pits (i.e. grooves), populate the opposite elongation (Pola Regio, 10°N–15°S, 150°–190°E, Fig. 9a) from Vienna Regio. These grooves resemble those found on Phobos, although they are far less prevalent. Their traces roughly trend parallel to Ida's long axis. Because Ida has probably never been geologically active, we propose that powerful stress waves from the formation of Vienna Regio, or possibly from some other large impact, were focused in the manner described above to create these features.

Vienna Regio is about the size of Stickney on Phobos. If it is an impact structure, and if Ida and Phobos have similar mechanical properties, one expects a comparable outcome, except that the impact energy dissipates over a volume several times larger than Phobos, resulting in less severe distal effects. The planar regularity of grooves on Phobos suggest the existence of tidal-induced jointing prior to the impact (cf. Weidenschilling 1979), something that could not occur on Ida. The formation of local grooves far from the impact might be enhanced by Ida's significant elongation, as suggested by Fig. 7. Surface gravity (including spin) near Vienna Regio is approximately 0.6 cm s^{-2}, so that a crater diameter of 12 km implies an impactor radius of 165 m (Eq. (4)) at 3.55 km/s. Prior to the impact we "repair" the SPH target by filling in the concavity with a spherical cap so that it better resembles the pre-impacted target; this repair work is evident in Fig. 9. The impact trajectory strikes the center of the existing concavity with a vector pointed towards the target center. The effect of alternate trajectories has not been explored.

After the moment of impact, "snapshots" taken every few seconds reveal the formation of a detached stress wave propagating into the target, which then becomes asymmetrical as it responds to boundary conditions on its way to the far end (Fig. 10). When this strong compressive wave encounters a free surface, it reflects as a tensile image (Melosh 1984). These tensile reflections can be sufficiently strong to cause immediate rupture at the surface, but in a finite target they can come to focus elsewhere. If this focused tensile stress exceeds the local strength of the rock, a crack grows. Due to Ida's irregular shape, stresses emanating from Vienna Regio come to a focus both where the Pola Regio grooves are observed (Fig. 9b), and in a region poorly imaged by the spacecraft (~30°–40°S, 320°–0°E, Fig. 11), causing localized damage far from the crater.

In the model, fracture damage in Pola Regio forms a tight cluster of about a dozen particles, instead of a field of narrower fractures extending over a larger region (Fig. 9b). This result is not as impressive as the actual geological features, nor as widespread, but a better correlation is not likely. For one thing, the actual grooves are significantly smaller than our particle dimensions (and stress release in SPH is felt two particle radii away), so that the true fracture stresses are averaged over a comparatively large region. Furthermore, the shape model from which our SPH target is derived has an accuracy of only a few hundred meters, and this difference can cause noticeable differences in wave reflection. If regions of Ida have thick regolith, the reflected wave bounces from an interior boundary instead of from the observed surface from which the shape model and our target were derived. Similarly, we may be off by as much as ~1 km in our "reparation" of the post-impact target. We have also ignored any significant internal structure (see below, however). A slightly larger impactor would probably produce more damage in this region, in better agreement with observation. We have tested Ida to failure (most of the target suffers fracture damage when stuck by a 300 m radius impactor), but a more sensitive exploration of the effect of impactor radius is probably not warranted.

Cross-sections of the target (Fig. 11) show the extent of interior damage due to the Vienna Regio impact. The totally fragmented zone is not much different from the 2D result of Fig. 7; directly beneath the impact site, near-field

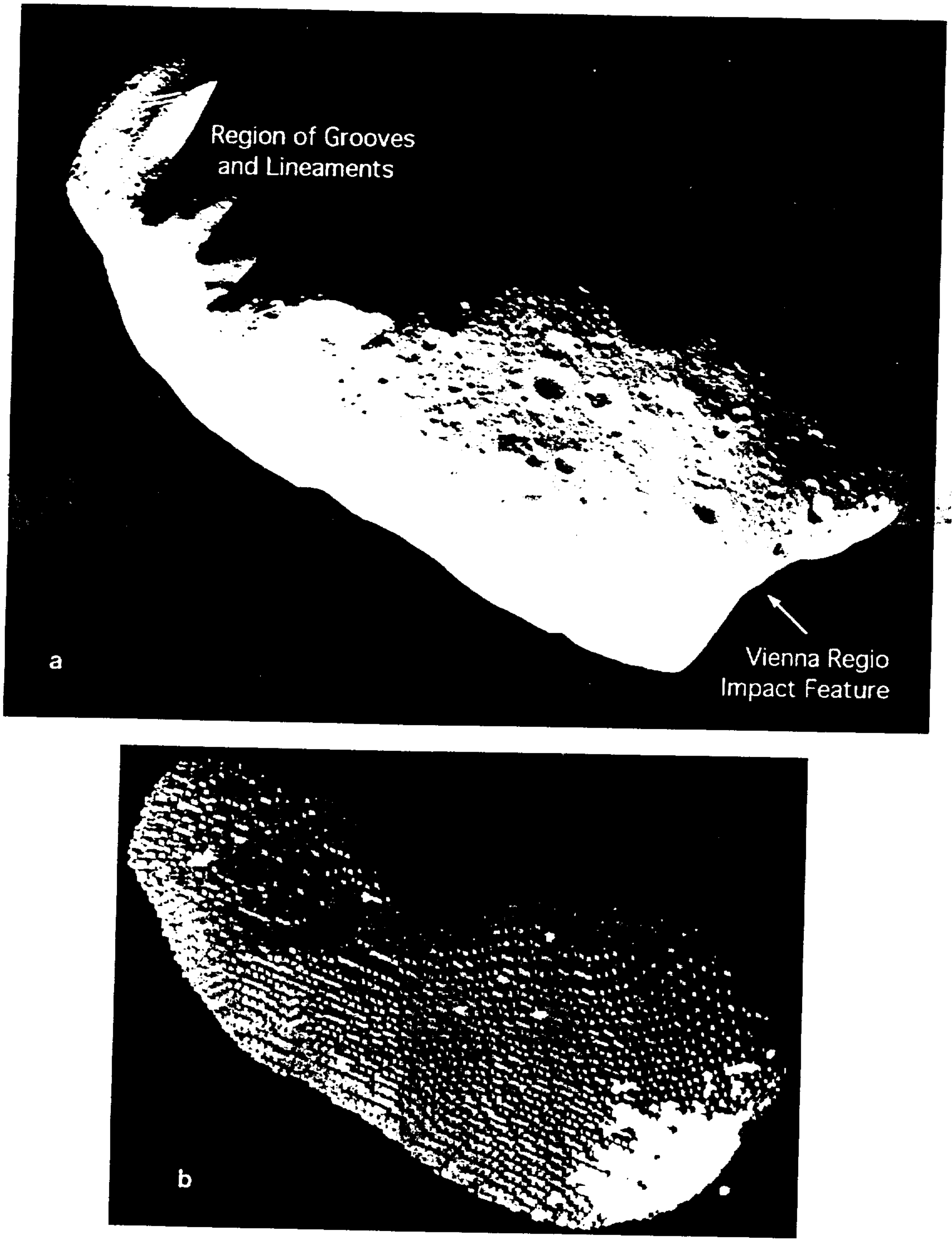

FIG. 9. (a) The five-image high resolution mosaic of Ida showing traces of the more conspicuous grooves, principally occuring in Pola Regio (upper left). Vienna Regio is seen in profile along the limb at the lower right. (b) A rendering at approximately the same perspective as (a) of the results of the 3D Vienna Regio impact model showing far-field damage clustered in about a dozen particles near the groove location. A slightly larger impactor, or a slightly weaker model Ida, would presumably result in more severe fragmentation in the same location.

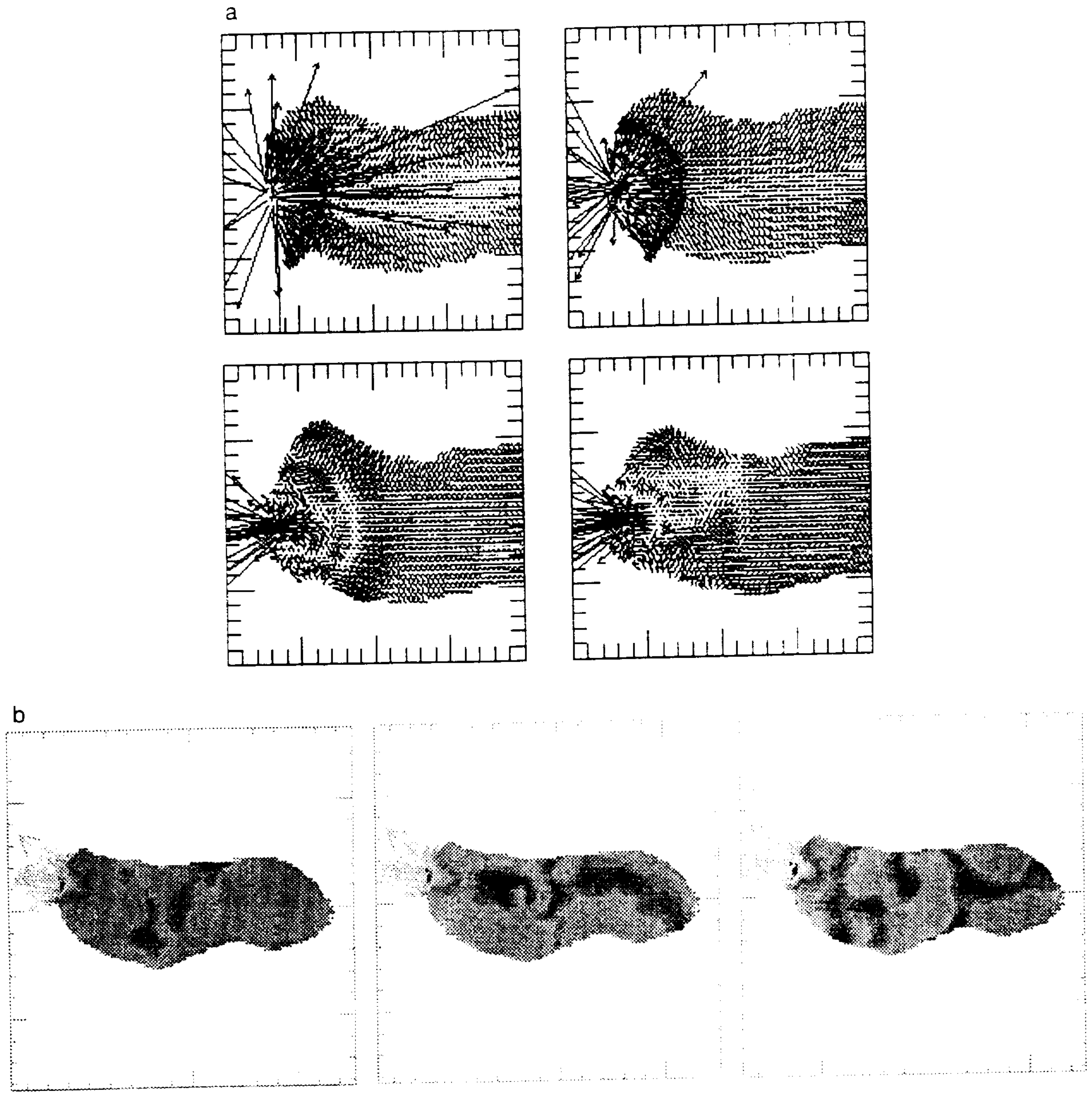

FIG. 10 (a) Cross sectional "snapshots" of the interior of the 3D SPH Ida model at 1.5, 2.0, 3.5 and 5.0 sec after the Vienna Regio impact, showing the detactment and evolution of the stress wave. These snapshots plot the particle velocities in a slice through the center of the target. (The plotting of overlapping nodes creates line patterns in the undisturbed body which should not be mistaken for vectors.) Evolution is at first similar to a 2D calculation but grows increasingly convoluted as waves reflect from free surfaces. (b) Contours of the speeds inside the same target, at times 8, 10, and 12 sec after the impact. These three figures, which include the projectile, show zero-velocity nodes as black.

damage extends about one crater diameter into the target. Far-field damage occurs only at the surface and does not penetrate beneath the surface. The difference between this result and the more extensive interior damage at the antipode of our 2D models is attributable to the perfect focusing of stress waves in axial symmetry as opposed to the more modest focusing in 3D. The interior of Ida is otherwise undamaged. Maximum velocities in the interior and at the surface are approximately the same as those contoured in Fig. 7g.

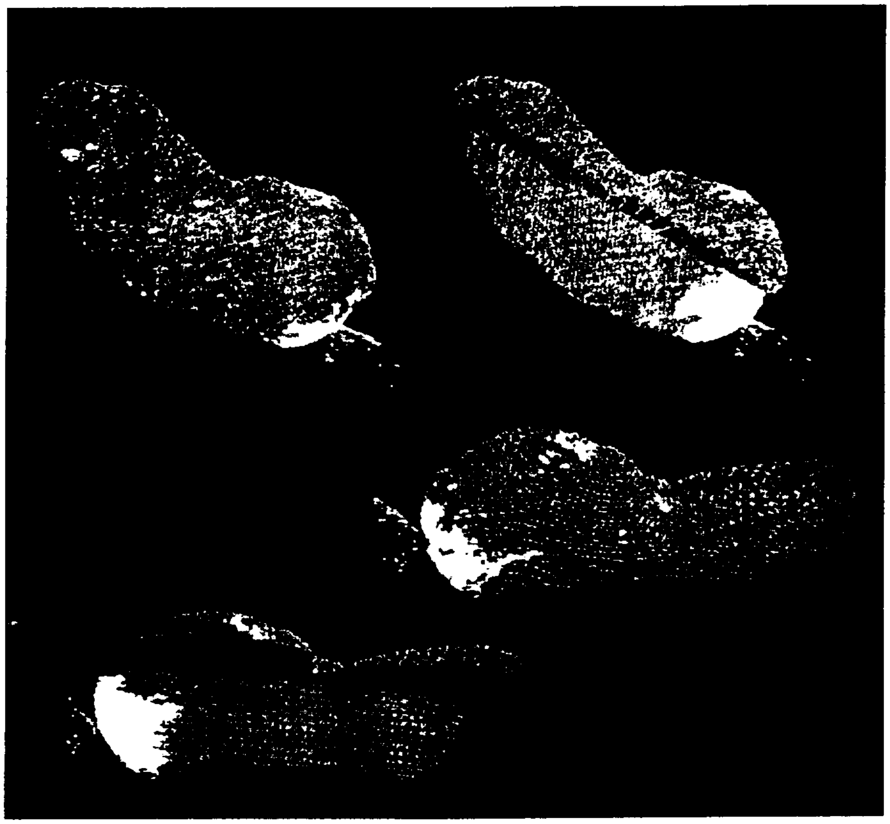

FIG. 11. Final damage (t = 15 sec) in the 3D SPH simulation of the Vienna Regio impact. The upper left figure shows a similar perspective as Fig. 9b, rotated so that damage in Pola Regio can be better presented in cross section (upper right). All damaged particles are colored white; the unfractured rock is grey. The lower right figure shows the damage to a poorly imaged region of Ida, with cross-section at lower left. Direct impact stress causes damage about one crater diameter from the impact; the deep interior remains unfractured. Cracks tend to nucleate at the free surface, where compressive waves reflect as tensile images.

Effects of Orgnac and Azzurra Impacts

Two other impacts are modeled in a similar manner. We do not first "rebuild" the pre-impact surface, as these craters (Orgnac and Azzurra) are very shallow, with a depth-diameter ratio $\lambda \approx 0.1$ (Sullivan *et al.* 1996). The ~9 km diameter crater Orgnac (5°S, 205°E), was estimated, using gravity scaling (Eq. (4)), to be formed by a 125 m radius impactor at 3.55 km s^{-1}. The ~10 km diameter crater Azzurra (30°N, 220°E), forming in somewhat higher gravity, was modeled with a 150 m impactor at the same speed (Table II). As before, the impact trajectory points towards the target center.

As in the case of Vienna Regio, reflected stresses cause far-field damage during the formation of Azzurra in the vicinity of Pola Regio where grooves are found. However, the damage calculated from this impact is less substantial than that produced by the Vienna Regio simulation (Fig. 12). Because Azzurra is morphologically well expressed, and may be genetically associated with a proximal "blue" deposit (Geissler *et al.*, 1996) whose color may be a marker of relative youth, the Pola Regio grooves (which themselves appear fresh) may have been created by the Vienna Regio impact but subsequently rejuvenated during the formation of Azzurra. Alternatively, these tectonic grooves may be the re-opening of fractures left over from Ida's parental breakup. In that case, however, there is no compelling geometrical reason for grooves to be local only to Pola Regio. Our model shows negligible far-field damage related to the creation of Orgnac (Fig. 12). For these two craters, just as in the case of Vienna Regio, near-field damage extends about one crater diameter into the target. A higher-resolution computation of the Azzurra impact, in progress, may lead to additional insight. Note in Table II that the linear and angular momenta imparted to Ida by these impacts (when one subtracts escaping material and sums over the remainder) is almost negligible.

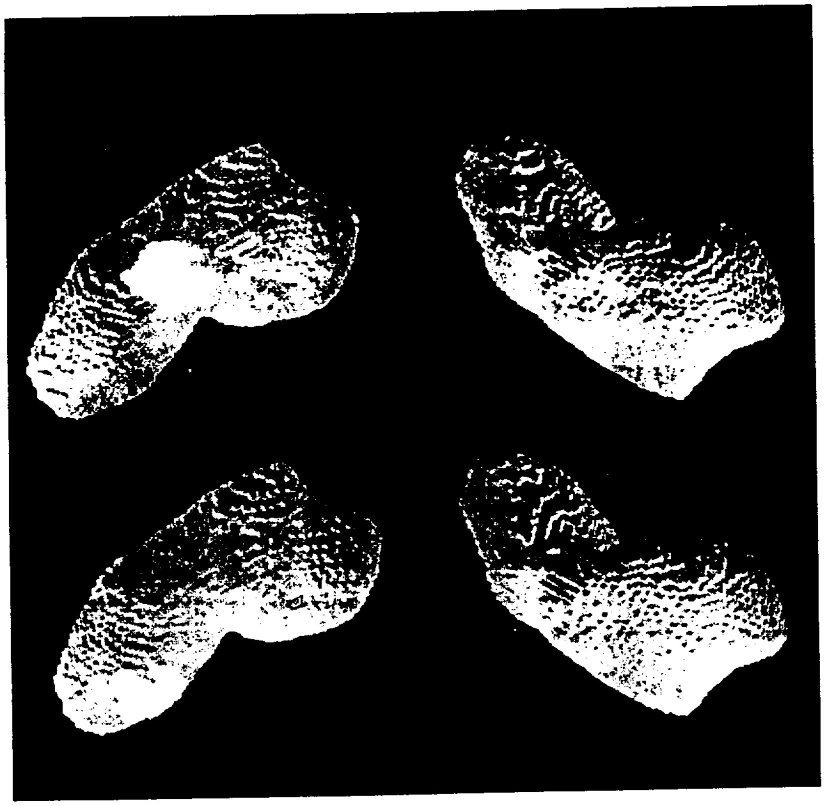

FIG. 12. Final damage to the 3D Ida model from a simulation of the Azzurra impact (upper figures) and the Orgnac impact (lower). These targets are of lower resolution than the Vienna Regio simulation; they look different because Vienna Regio has not been "repaired." The perspectives on the right are similar to Figs. 9a and b. Note a few scattered particles suffering damage within the region of the grooves caused by the Azzurra impact (upper right). There is no significant far-field damage associated with Orgnac at this model resolution.

Porosity

An impact into a target with the same bulk density but with heterogeneities (pores) on a scale comparable to the impactor creates a crater of the same *diameter* as an impact into a homogeneous target, but the stress waves dissipate and scatter without being able to open up distal fractures. We have not simulated porosity in any impacts specific to Ida, but Asphaug and Benz (1994) created a porous Phobos (Fig. 13) by removing 28% of the SPH particles, at random, from a $\rho = 2.7$ g cm^{-3} triaxial ellipsoid. They also created a non-porous Phobos using the same constitutive model but with the actual density of Phobos ($\rho = 1.95$ g cm^{-3}; Avanesov *et al.* 1989) substituted into the equation of state. They applied the same code as used here to model the formation of the large impact crater Stickney, starting with a 116 m radius impactor at 6 km s^{-1}.

In each of the two targets a fragmented region somewhat larger than Stickney was created. Figure 13 shows that the near-field damage regions are almost identical. Only in the non-porous target, however, did distal fractures appear. One of the implications of the existence of far-field fracture grooves on asteroids and satellites, apparently, is that their interior allows for the coherent transmission of stress waves. We do not mean to suggest a crystalline, monolithic interior. Irregularities and voids on a scale smaller than the width of the stress pulse (approximately the diameter of the projectile) are allowed, and so are well-connected fault planes, since a compressive stress passes across such a boundary uninterrupted. But an interior which is blocky on a larger scale—i.e., a "rubble pile"—is inconsistent with our results.

V. CONCLUSIONS

Impacts are the single most important geological process shaping Ida's surface; we have therefore examined the role they play in the formation and modification of craters and crater-related landforms, from the small craters of the strength regime to the largest planet-shaping impacts. Although we are unable to follow the evolution of these

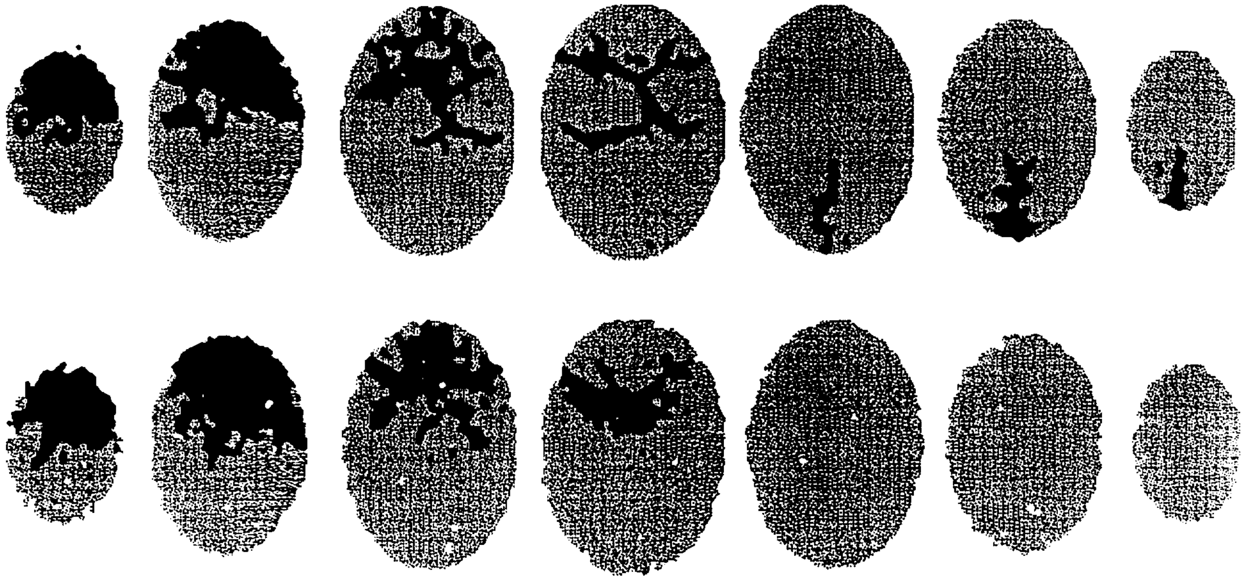

FIG. 13. In a study of the formation of grooves on Phobos resulting from the Stickney impact, Asphaug and Benz (1994) applied the same 3D SPH code to best fit a triaxial ellipsoid target. The upper row of figures shows cross-sections through their homogeneous Phobos target at the end of the simulation. The slices, at 3 km intervals, proceed from the trailing hemisphere (where the crater is seen as an extensive damaged region) to the leading hemisphere. Fracture grooves radiate from the crater, and also form in the opposite hemisphere where the impact stresses converge. The lower row of figures shows an identical sequence of cross-sections, but this time through a target with randomly distributed voids and the same bulk density. The scattering interior prohibits coherent propagation of stress waves; no far-field fracture grooves result.

craters beyond the completion of fracture damage and the emplacement of the ejecta flow, we can compare the instantaneous velocities at the end of fragmentation with surface gravity, and compare the diameters of fracture zones with the predictions of gravity scaling, to arrive at four principal findings:

(1) *Bright annuli around small craters on Ida are better explained by ejection than deposition.* The excavation of these craters is largely governed by material strength. Because surface gravity is low, crater ejecta moves too fast to form a proximal depositional ring. An impact into a strength-dominated substrate, on the other hand, causes seismic disturbances capable of removing, overturning or shaking an annulus of weathered material beyond the fragmentation rim. Comparison of our numerical models with the data suggests that bright annuli are created by seismic motions of several cm $\sec^{-1}$, launching material tens of meters. The lack of annuli for craters larger than ~1 km diameter is consistent with our prediction that gravity scaling applies for those craters.

(2) *Large circular concavities can be formed directly by impacts.* Nothing in our modeling suggests any impact mechanism other than cratering which can excavate large circular concavities from an asteroidal target. They are not spallation scars: even if a distant region suffers disruption, as in Fig. 7a, the particle velocity is not sufficient for transport away from the region. Instead, we find that these concavities can be directly attributed to cratering impacts. Their odd shapes are due to the target's comparatively small radius of curvature, and to the substantial variation in surface gravity across the diameter of the transient cavity.

(3) *The grooves of Pola Regio may have been created by the impact that formed Vienna Regio.* Far-field stress wave focusing causes local damage in the appropriate region of Ida when we simulate the impact responsible for the Vienna Regio concavity. Because of their relative youth, these grooves may have been rejuvenated during the formation of Azzurra, which also led to focused, though less powerful, seismic stresses at that location. It is also possible that Azzurra reopened fractures resulting from the formation of Vienna Regio or the Koronis parent body's breakup.

(4) *If the Pola Regio grooves are the result of a distant cratering event, then Ida must have been mechanically coupled.* A rubble-pile interior would attenuate the impact stress and prevent far-field fracture from occurring. Because no currently recognized impact feature on Ida could

have disrupted the asteroid to great depth since the Koronis breakup, Ida probably maintains a coherent deep interior today.

APPENDIX

An understanding of what our results do and do not imply requires some knowledge of how we calculate our answers; otherwise our conclusions spring out of a black box. While most of the motivations, justifications, and reservations regarding our model are presented in the text, what follows is a sufficient basis for reproducing our results.

Hydrocodes integrate the partial differential equations governing energy, mass, and momentum conservation, together with an equation of state relating stress (pressure), strain (density), and temperature (internal energy). Because analytical solutions to these so-called continuum equations exist for only a few exceptionally symmetric and idealized cases, these equations are solved by converting derivatives into finite differences, so that $dt \rightarrow t_{n+1} - t_n$, $dx \rightarrow x_{n+1} - x_n$, and so on. In the simplest terms, the initial conditions at time t_0 (together with the boundary conditions) are evolved to $t_1 = t_0 + dt$ by computing a stress term inside each finite volume (a "cell" or "particle") when it is deformed by a velocity gradient. This stress then modifies the velocities, which become a new deformation when multiplied by dt. These deformations cause new stresses which take us to the subsequent timestep t_2, and so on. Many finite difference schemes exist (see Benz 1989), and some are better suited than others to any particular class of problems. The main task is to arrive at stable and accurate solutions; this is achieved by limiting the timestep dt and the grid size dx, at the cost of machine time, so as to satisfy a number of stability and accuracy criteria which are beyond the scope of this discussion.

The high-energy and low-energy phases are the easiest to model, since at high energy (at the impact locus, for instance) interactions generally take place in the vapor phase, while at the lowest energies stress is linearly related to strain by Hooke's law. The transition between these regimes is not just a matter of melting and vaporization; solid-state mechanisms such as plastic yielding and brittle fragmentation are central to cratering but tend to resist simplification. Shock waves must be treated with particular care (cf. von Neumann and Richtmyer 1950) since they are responsible for much of the fragmentation associated with crater formation, all of the melting and vaporization, as well as the emplacement of the ejeca flow.

Equations for an Elastic–Perfectly Plastic Strength Model

The conservation equations solved by hydrocodes can be found in most standard textbooks. The first describes mass conservation,

$$\frac{d\rho}{dt} + \rho \frac{\partial}{\partial x^\alpha} v^\alpha = 0 \tag{A1}$$

where d/dt is the Lagrangian time derivative, ρ is the density, and x^α and v^α are the positions and velocities. Superscripts here define the spatial indices, where we assume the usual summation rule. The next equation describes the conservation of momentum (no gravity)

$$\frac{dv^\alpha}{dt} = \frac{1}{\rho} \frac{\partial}{\partial x^\beta} \sigma^{\alpha\beta}, \tag{A2}$$

where $\sigma^{\alpha\beta}$ is the stress tensor given by

$$\sigma^{\alpha\beta} = -P\delta^{\alpha\beta} + S^{\alpha\beta}, \tag{A3}$$

where P is the pressure and $S^{\alpha\beta}$ the traceless deviatoric stress tensor and $\delta^{\alpha\beta}$ is the Kroneker symbol. Finally, the conservation of energy u is given by

$$\frac{du}{dt} = -\frac{P}{\rho} \frac{\partial}{\partial x^\alpha} v^\alpha + \frac{1}{\rho} S^{\alpha\beta} \dot{\varepsilon}^{\alpha\beta}, \tag{A4}$$

where $\dot{\varepsilon}^{\alpha\beta}$ is the strain rate tensor,

$$\dot{\varepsilon}^{\alpha\beta} = \frac{1}{2} \left(\frac{\partial}{\partial x^\beta} v^\alpha + \frac{\partial}{\partial x^\alpha} v^\beta \right). \tag{A5}$$

The time evolution of $S^{\alpha\beta}$ still needs to be specified for materials with strength. We adopt Hooke's law and write

$$\frac{dS^{\alpha\beta}}{dt} = 2\mu \left(\dot{\varepsilon}^{\alpha\beta} - \frac{1}{3} \delta^{\alpha\beta} \dot{\varepsilon}^{\gamma\gamma} \right) + \text{rotation terms}, \tag{A6}$$

where μ is the shear modulus. In the simplest case, assuming small angles, the rotation terms become $-SR - RS$, where R is given by

$$R^{\alpha\beta} = \frac{1}{2} \left(\frac{\partial}{\partial x^\beta} v^\alpha - \frac{\partial}{\partial x^\alpha} v^\beta \right). \tag{A7}$$

Equations (A1)–(A7) can be solved if we specify an equation of state, $P = P(\rho, u)$, and describe perfectly elastic materials. But for actual materials a critical stress always exists that results in permanent deformation. Plastic behavior beyond this critical stress is introduced using the von Mises criterion which limits the deviatoric stress tensor by

$$S^{\alpha\beta} \rightarrow f S^{\alpha\beta}, \tag{A8}$$

where f is computed from

$$f = \min \left[\frac{Y_0^2}{3J_2}, 1 \right], \tag{A9}$$

where J_2 is the second invariant of the deviatoric stress tensor

$$J_2 = \frac{1}{2} S^{\alpha\beta} S^{\alpha\beta}, \tag{A10}$$

and Y_0 is a material dependent yield stress which decreases with increasing temperature. Beyond the melting point $Y_0 = 0$.

Fracture

Continuum fracture models can lead to serious inconsistencies between hydrodynamics and fragmentation unless fractures are smaller than the code resolution. To resolve this inconsistency Benz and Asphaug (1994a,b) derived a method based on the existence and growth of ***explicit*** flaws, populated according to the Weibull probability distribution discussed in the main text,

$$n(\varepsilon) = k\varepsilon^m, \tag{A11}$$

where n is the number, per unit volume, of flaws that have activation thresholds at or below a given strain ε, and k and m are material constants. (Note that stress can be used in place of strain in the Weibull distribution, but it must be divided by an elastic modulus to provide a dimensionless number.)

Following this method, we establish stochastic initial conditions by distributing N_f activation strains (flaws) in a uniformly random manner among all the hydrocode "cells" (or "particles" in an SPH simulation) until each has been assigned at least one flaw. If each cell has equal volume, then for each flaw j, $1 \leq j \leq N_f$, a cell i is chosen at random (with replacement) and attributed the corresponding activation threshold,

$$\varepsilon_{i,j}^{\text{act}} = \left[\frac{j}{kV}\right]^{1/m}. \tag{A12}$$

which follows from (A11). If the number of cells in the hydrocode grid is N_{cell}, each is assigned on average $n_i^{\text{tot}} \approx \ln(N_{\text{cell}})$ flaws by this method. Because it is not a consecutive assignment, a typical cell receives numerous flaws with a wide range of thresholds. If the cells are not of equal volume, as in most 2D simulations, cells are chosen at random by weighting them according to their volume V_{cell}, so that larger cells get assigned flaws more frequently. Damage is approximately radially symmetric about the impact point in our axially symmetric calculations (Fig. 2), attesting to the fact that equal subvolumes of the target are assigned the same flaw statistics regardless of resolution. The use of different seeds in the random number generator produces different flaw assignments, so ideally an average would be compiled over several runs. In practice the difference is of little consequence compared to other uncertainties, such as target shape, density fluctuations, etc.

Accumulation of Damage

The assumptions for crack growth and stress release are essentially those of Grady and Kipp (1980). A flaw becomes active once the effective local strain (the stress, after yielding, divided by the elastic modulus) has reached the flaw's tensile activation threshold. It then grows at constant velocity c_g, which is approximately 0.4 times the speed of a longitudinal elastic wave (Lawn and Wilshaw 1975). The half-length of a growing crack is therefore

$$a = a_0 + c_g(t - t'), \tag{A13}$$

where t' is the crack activation time. We assume that the initial crack length a_0 is negligible. A local variable D ("damage"), $0 \leq D \leq 1$ (Grady and Kipp 1980), is used to compute stress-release due to the growth of cracks, and this released stress is used in subsequent evaluations of the effective local strain. In one dimension, damage expresses a reduced strength only under tension,

$$\sigma_D = \sigma(1 - D), \tag{A14}$$

where σ is the elastic stress in the absence of damage and σ_D is the damage-relieved stress.

A crack relieves stress in a neighborhood approximately equal to a circumscribing sphere (Walsh 1965); thus, D is defined in a local region V_s as the fractional volume that is relieved of stress by local growing cracks.

$$D = \tfrac{4}{3}\pi a^3 / V_s. \tag{A15}$$

We now depart from Grady–Kipp theory by performing explicit integrations over all active flaws in a cell. Equation (A15) leads to a simple differential equation for the rate of increase of damage from one flaw,

$$\frac{dD^{1/3}}{dt} = \frac{c_g}{R_s}, \tag{A16}$$

where $R_s = (3V_s/4\pi)^{1/3}$ is the mean radius of the volume element in which a crack of half-length a is growing. In an elemental subvolume V_s, damage continues to accumulate once the activation threshold has been exceeded, regardless of subsequent stress release. Over a larger volume, such as a hydrocode cell containing many flaws, or a region in a target containing a number of hydrocode cells, damage in fact ceases when the strain relaxes since no new flaws become active. Rate dependence is therefore automatically included: at low rates of loading, the stress relaxes before additional (stronger) flaws become active. At high rates of loading, on the other hand, fracture is too slow to relieve the growing stress and additional flaws are required.

In multidimensions, we compute a scalar approximation to the actual strain, and damage applies to tensile as well as shear loads. A local effective tensile strain ε_i is computed in each cell $i = 1, \ldots, N_{\text{cell}}$ from the maximum tensile stress σ_i^t (possibly already reduced by damage and yielding) after a principal axis transformation (Melosh *et al.* 1992) according to the relation

$$\varepsilon_i = \frac{\sigma_i^t}{(1 - D_i)E}, \tag{A17}$$

where D_i is the local value of the damage, $E = 9K\mu/(3K + \mu)$ is Young's elastic modulus, and K is the bulk modulus. This transformation enables the approximate modeling of shear failure, since a shear strain decomposes onto one tensile and one compressive principal axis. A more direct model for shear failure based on the Mohr–Coulomb criterion has been coded but not calibrated.

The use of Young's modulus ensures that the system reduces to its 1D form in uniaxial stress events. If ε_i exceeds any of the thresholds $\varepsilon_{i,j}^{\text{act}}$ contained in cell i, damage associated with that cell accumulates at a rate given by Eq. (A16) multiplied by the number n_i of active flaws. Damage can accumulate in a given timestep to a maximum value given by

$$D_i^{\max} = \left(\frac{n_i}{n_i^{\text{tot}}}\right)^{1/3}, \tag{A18}$$

where n_i^{tot} is the total number of flaws that were assigned to cell i. A necessary condition for a given cell to reach a totally damaged state is that all internal flaws are activated; this latter condition is required to ensure resolution independence. Once the activation of several flaws takes place, further regional stresses concentrate in the damaged cell, rapidly activating the remainder of the flaws if strain rate is constant. On the other hand, if the regional strain relaxes, the cell remains only partially damaged. In a dynamic event, damage by and large jumps rather rapidly from 0 to 1.

ACKNOWLEDGMENTS

Peter Thomas made much of this work possible by providing his 2° and 5° shape models of Ida. We thank J. N. Cuzzi for use of high-performance computational facilities at NASA Ames, W. B. McKinnon for key ideas toward a more concise and coherent development, K. Zahnle for insights into the halfspace calculations, and an anonymous referee. E. Asphaug and W. Benz were supported by NASA Grant NAGW-3904, and E. Asphaug was also supported by the National Research Council. D. Morrison and J. M. Moore were supported through the Galileo Interdisciplinary Science effort, M. Nolan was supported by NASA Grant NAGW-1029, and R. Sullivan was supported by the Galileo Solid State Imaging Team.

REFERENCES

Ahrens, T. J., and J. D. O'Keefe 1977. Equations of state and impact-induced shock wave attenuation on the moon. In *Impact and Explosion*

Cratering (D. J. Roddy, R. O. Pepikn, and R. B. Merrill, Eds.), pp. 639–656. Pergamon Press, New York.

Ahrens, T. J., and Rubin, A. M. 1993. Impact-induced tensional failure in rock. *J. Geophys. Res.* **98**, 1185–1203.

Amsden, A. A., H. M. Ruppel, and C. W. Hirt 1980. *SALE: A Simplified ALE Computer Program for Fluid Flow at All Speeds*. Los Alamos Scientific Laboratory Report LA-8095.

Asphaug, E. 1993. *Dynamic Fragmentation in the Solar System: Applications of Fracture Mechanics and Hydrodynamics to Questions of Planetary Evolution*. Ph.D. Dissertation, University of Arizona.

Asphaug, E., and H. J. Melosh 1993. The Stickney impact of Phobos: A dynamical model. *Icarus* **101**, 144–164.

Asphaug, E., and W. Benz 1994. The surface and interior of Phobos. In *LPSC XXV Abstracts*, pp. 43–44.

Avanesov, G. A., B. I. Bonev, F. Kempe, A. T. Bazilevsky, V. Boycheva, K. N. Chikov, M. Danz, D. Dimitrov, T. Duxbury, P. Gromatikov, D. Halmann, J. Head, V. N. Heifets, V. Kolev, V. I. Kostenko, V. A. Kottsov, V. M. Krasavtsev, V. A. Krasikov, A. Krumov, A. A. Kuzmin, K. D. Losev, K. Lumme, D. N. Mishev, D. Mohlmann, K. Muinonen, V. M. Murav'ev, S. Murchie, B. Murray, W. Neumann, L. Paul, D. Petkov, I. Petuchova, W. Possel, B. Rebel, Yu. G. Shkuratov, S. Simeonov, B. Smith, A. Totev, Yu. Uzunov, V. P. Fedotov, G. G. Weide, H. Zapfe, B. S. Zhukov, and Ya. L. Ziman 1989. Television observations of Phobos. *Nature* **341**, 585–587.

Belton, M. J. S., J. Veverka, P. Thomas, P. Helfenstein, D. Simonelli, C. Chapman, M. E. Davies, R. Greeley, R. Greenberg, J. Head, S. Murchie, K. Klaasen, T. V. Johnson, A. McEwen, D. Morrison, G. Neukum, F. Fanale, C. Anger, M. Carr, and C. Pilcher 1992. Galileo encounter with 951 Gaspra: First pictures of an asteroid. *Science* **257**, 1647–1652.

Belton, M. J. S., C. R. Chapman, J. Veverka, K. P. Klaasen, A. Harch, R. Greeley, R. Greenberg, J. W. Head III, A. McEwen, D. Morrison, P. Thomas, M. E. Davies, M. H. Carr, G. Neukum, F. P. Fanale, D. R. Davis, C. Anger, P. J. Gierasch, A. P. Ingersoll, and C. B. Pilcher 1994. First images of 243 Ida. *Science* **265**, 1543–1547.

Belton, M. J. S., C. R. Chapman, K. P. Klaasen, A. P. Harch, P. C. Thomas, J. Veverka, A. S. McEwen, and R. T. Pappalardo 1996. Galileo's encounter with 243 Ida: An overview of the imaging experiment. *Icarus* **120**, 1–19.

Benz, W. 1989. An introduction to methods in computational hydrodynamics. In *Computational Methods in Astrophysical Fluid Dynamics* (C. de Loore, Ed.). Springer-Verlag, Berlin.

Benz, W. 1990. Smooth particle hydrodynamics: A review. In *Numerical Modeling of Nonlinear Stellar Pulsation: Problems and Prospects* (J. R. Buchler, Ed.). Kluwer Academic, Dordrecht.

Benz, W., and E. Asphaug 1994a. Impact simulations with fracture. I. Method and tests. *Icarus* **107**, 98–116.

Benz, W., and E. Asphaug 1994b. Simulations of brittle solids using smooth particle hydrodynamics. *Comput. Phys. Comm.* **87**, 253–265.

Binzel, R. P., and S. Xu 1993. Chips off Vesta. *Science* **260**, 186–191.

Bottke, W. F., M. C. Nolan, R. Greenberg, and R. A. Kolvoord 1994. Velocity distributions among colliding asteroids. *Icarus* **107**, 255–268.

Buckingham, E. 1914. On physically similar systems: Illustrations of the use of dimensional equations. *Phys. Rev. IV* **4**, 345.

Chapman, C. R., G. Neukum, J. Veverka, and M. J. S. Belton 1993. Cratering on Gaspra. In *LPSC XXIV Abstracts*, pp. 269–270.

Davis, D. R., C. R. Chapman, R. Greenberg, S. J. Weidenschilling, and A. W. Harris 1979. Collisional evolution of asteroids: Populations, rotations, and velocities. In *Asteroids* (T. Gehrels, Ed.), pp. 528–557. Univ. of Arizona Press, Tucson.

Farinella, P., P. Paolicchi, and V. Zappala 1982. The asteroids as outcomes of catastrophic collisions. *Icarus* **52**, 409–433.

Fourney, W. L., D. C. Holloway, and D. B. Barker 1984. Model studies of fragmentation. In *Mechanics of Oil Shale* (K. P. Chong and J. W. Smith, Eds.), pp. 337–388. Elsevier, New York.

Fujiwara, A. 1982. Complete fragmentation of the parent bodies of Themis, Eos, and Koronis families. *Icarus* **52**, 434–443.

Fujiwara, A. 1991. Stickney-forming impact on Phobos: Crater shape and induced stress distribution. *Icarus* **89**, 384–391.

Fujiwara, A., P. Cerroni, D. Davis, E. Ryan, M. DiMartino, K. Holsapple, and K. Housen 1989. Experiments and scaling laws for catastrophic collisions. In *Asteroids II* (R. P. Binzel, T. Gehrels, and M. S. Matthews, Eds.), pp. 240–265. Univ. of Arizona Press, Tucson.

Fukushima, K. 1990. Scale effects on underground excavations. In *Scale Effects in Rock Masses* (A. P. Cunha, Ed.), pp. 209–219. Balkema, Rotterdam.

Gault, D. E., E. M. Shoemaker, and H. J. Moore 1963. *Spray Ejected from the Lunar Surface by Meteoroid Impact*. NASA TN D-1767.

Geissler, P., J.-M. Petit, D. Durda, R. Greenberg, W. F. Bottke, M. C. Nolan, and J. Moore 1996. Erosion and ejecta reaccretion of 243 Ida and its moon. *Icarus* **120**, 140–157.

Grady, D. E., and M. E. Kipp 1980. Continuum modelling of explosive fracture in oil shale. In *Int. J. Rock Mech. Min. Sci. Geomech. Abstr.*, Vol. **17**, pp. 147–157.

Greenberg, R., M. C. Nolan, W. F. Bottke, R. A. Kolvoord, and J. Veverka 1994. Collisional history of Gaspra. *Icarus* **107**, 84–97.

Greenberg, R., W. F. Bottke, M. C. Nolan, P. Geissler, J.-M. Petit, D. Durda, E. Asphaug, and J. Head 1996. Collisional and dynamical history of Ida. *Icarus* **120**, 106–118.

Holsapple, K. A. 1981. Coupling parameters in cratering. *Eos Trans. Am. Geophys. Union*, Vol. **62**, p. 944, Abstract.

Holsapple, K. A. 1993. The scaling of impact processes in planetary sciences. *Ann. Rev. Earth Planet. Sci.* **21**, 333–373.

Holsapple, K. A., and R. M. Schmidt 1982. On the scaling of crater dimensions. 2. Impact processes. *J. Geophys. Res.* **87**, 1849–1870.

Housen, K. R., L. L. Wilkening, C. R. Chapman, and R. Greenberg 1979. Asteroid regoliths. *Icarus* **39**, 317–351.

Housen, K. R., R. M. Schmidt, and K. A. Holsapple 1983. Crater ejecta scaling laws: Fundamental forms based on dimensional analysis. *J. Geophys. Res.* **88**, 2485–2499.

Housen, K. R., and R. M. Schmidt 1996. Ejecta velocities for cratering in rock. *Icarus*, submitted.

Jaeger, J. C., and N. G. W. Cook 1969. *Fundamentals of Rock Mechanics*. Chapman & Hall, London.

Lawn, B. R., and T. R. Wilshaw 1975. *Fracture of Brittle Solids*. Cambridge Univ. Press, New York.

Lucy, L. B. 1977. A numerical approach to the testing of the fission hypothesis. *Astron. J.* **82**, 1013–1024.

Melosh, H. J. 1987. High-velocity solid ejecta fragments from hypervelocity impacts. *Int. J. Impact Eng.* **5**, 483–492.

Melosh, H. J. 1989. *Impact Cratering: A Geologic Process*. Oxford Univ. Press, New York.

Melosh, H. J., E. V. Ryan, and E. Asphaug 1992. Dynamic fragmentation in impacts: Hydrocode simulation of laboratory impacts. *J. Geophys. Res.* **97**, 14,735–14,759.

Minster, J. B., S. M. Day, and P. M. Shearer 1991. The transition to the elastic regime in the vicinity of an underground explosion. In *Explosion Source Phenomenology* (S. R. Taylor, H. J. Patton, and

P. G. Richards, Eds.), Geophysical Monograph 65, Am. Geophys. Union, Washington, DC.

Murphy, J. R. 1991. Free-field seismic observations from underground nuclear explosions. In *Explosion Source Phenomenology* (S. R. Taylor, H. J. Patton, and P. G. Richards, Eds.). Geophysical Monograph 65, Am. Geophys. Union, Washington, DC.

Nakamura, A., and A. Fujiwara 1991. Velocity distribution of fragments formed in a simulated collisional disruption. *Icarus* **92**, 132–146.

Nolan, M. C., E. Asphaug, and R. Greenberg 1993. Numerical simulation of impacts on small asteroids. *Bull. Am. Astron. Soc.* **24**, 959–960.

Nolan, M. C., E. Asphaug, H. J. Melosh, and R. Greenberg 1995. Impact craters on asteroids: Does gravity or strength control their size? *Icarus*, submitted.

O'Keefe, J. D., and T. J. Ahrens 1993. Planetary cratering mechanics. *J. Geophys. Res.* **98**, 17,011–17,028.

Perret, W. R., R. L. Rutter, F. K. Millsap, A. D. Thornbrough, and G. J. Hansen 1967. *Free-Field Particle Motion from a Nuclear Explosion in Salt, Part I, Project Dribble, Salmon Event*, Sandia Corporation VUF-3012.

Rinehart, J. S. 1965. The dynamic strength of rock. In *Proc. 7th US Symp. Rock Mech.* Pennsylvania State University.

Rodionov, V. N., V. V. Adushkin, V. N. Kostyuchenko, V. N. Nikolaevskii, A. N. Romashov, M. A. Sadovskii, and V. M. Tsvetkov 1972. *Mechanical Effect of an Underground Explosion*. UCRL-Trans-10676, Peaceful Applications TID-4500.

Rummel, F. 1987. Fracture mechanics approach to hydraulic fracturing stress measurements. In *Fracture Mechanics of Rock* (B. K. Atkinson, pp. 217–240. Academic Press, London.

Schmidt, R., and K. Housen 1995. Problem solving with dimensional analysis. *Ind. Physicist* **1**, 21–24.

Stöffler, D. 1972. Deformation and transformation of rock-forming minerals by natural and experimental shock processes. *Fortschr. Mineral.* **49**, 50–113.

Sullivan, R., R. Greeley, R. Pappalardo, E. Asphaug, J. M. Moore, D. Morrison, M. J. S. Belton, M. Carr, C. R. Chapman, P. Geissler, R. Greenberg, James Granahan, J. W. Head III, R. Kirk, A. McEwen, P. Lee, P. C. Thomas, and J. Veverka 1996. Geology of 243 Ida. *Icarus* **120**, 119–139.

Thomas, P., and J. Veverka 1979. Grooves on asteroids: A prediction. *Icarus* **40**, 394–405.

Thomas, P., J. Veverka, A. Bloom, and T. C. Duxbury 1979. Grooves on Phobos: Their distribution, morphology, and possible origins. *J. Geophys. Res.* **84**, 8457–8477.

Thomas, P., M. J. S. Belton, B. Carcich, C. R. Chapman, M. E. Davies, R. Sullivan, and J. Veverka, 1996. The shape of Ida. *Icarus* **120**, 20–32.

Tillotson, J. H. 1962. *Metallic Equations of State for Hypervelocity Impact*. General Atomic Report GA-3216.

Tsvetkov, V. I., and A. Ya. Skripnik 1991. Atmospheric fragmentation of meteorites according to the strength theory. *Sol. Syst. Res.* **25**, 273–279.

Veverka, J., P. Thomas, T. V. Johnson, D. Matson, and K. Housen 1986. The physical characteristics of satellite surfaces. In *Satellites* (J. A. Burns and M. Matthews, Eds.), pp. 342–402. Univ. of Arizona Press, Tucson.

Veverka, J., P. Thomas, D. Simonelli, M. J. S. Belton, M. Carr, C. Chapman, M. E. Davies, R. Greeley, R. Greenberg, J. Head, K. Klaasen, T. V. Johnson, D. Morrison, and G. Neukum 1994. Discovery of grooves on Gaspra. *Icarus* **107**, 72–83.

von Neumann, J., and R. D. Richtmyer 1950. A method for the numerical calculation of hydrodynamic shocks. *J. Appl. Phys.* **21**, 232–237.

Walsh, J. B. 1965. The effect of cracks on the uniaxial elastic compression of rocks. *J. Geophys. Res.* **70**, 399–411.

Weibull, W. A. 1939. A statistical theory of the strength of materials. *Ingenioersvetenskapsakad. Handl.* **151**, 5–45.

Weidenschilling, S. J. 1979. A possible origin for the grooves of Phobos. *Nature* **282**, 697–698.

Wilson, L., and J. W. Head 1989. Dynamics of groove formation on Phobos by ejecta from Stickney. In *LPSC XX Abstracts*, pp. 1211–1212.

Meteoritics & Planetary Science 32, 965–980 (1997)

Impact origin of the Vesta family

ERIK ASPHAUG

SETI Institute/NASA Ames, MS 245-3, Moffett Field, California 94035, USA
Author's e-mail address: asphaug@cosmic.arc.nasa.gov

(Received 1996 December 20; accepted in revised form 1997 August 27)
(Presented at the Workshop on Vesta and the HED Meteorites, Houston, Texas, USA, 1996 October 16–18)

Abstract–The compelling petrographic link (Consolmagno and Drake, 1977; Gaffey, 1983) between basaltic achondrite meteorites and the ~530 km diameter asteroid 4 Vesta has been tempered by a perceived difficulty in launching rocks from this asteroid's surface at speeds sufficient to bring them to Earth (Wasson and Wetherill, 1979) without obliterating Vesta's signature crust. I address this impasse in response to recent imaging (Zellner *et al.*, 1996; Dumas and Hainaut, 1996) of a ~450 km impact basin across Vesta's southern hemisphere (Thomas *et al.*, 1997) and model the basin-forming collision using a detailed two-dimensional hydrocode with brittle fracture including self-gravitational compression (cf., Asphaug and Melosh, 1993). A ~42 km diameter asteroid striking Vesta's basaltic crust (atop a denser mantle and iron core) at 5.4 km/s launches multikilometer fragments up to ~600 m/s without inverting distal stratigraphy, according to the code. This modeling, together with collisional, dynamical, rheological and exposure-age timescales (Marzari *et al.*, 1996; Welten *et al.*, 1996), and observations of V-type asteroids (Binzel and Xu, 1993) suggests a recent (<~1 Ga) impact origin for the Vesta family and a possible Vesta origin for Earth-approaching V-type asteroids (Cruikshank *et al.*, 1991).

INTRODUCTION

A maturing body of evidence suggests that the geologically diverse main belt asteroid 4 Vesta is the ultimate parent body of the basaltic achondrite meteorites: howardites, eucrites and diogenites (HED). If HED meteorites come from Vesta, then diogenites (mostly orthopyroxene and occasional olivine) sample the deeper crust and mantle, and eucrites (mostly plagioclase and pigeonite) sample the surface (cf., Consolmagno and Drake, 1977; Gaffey and McCord, 1978). Howardites (polymict eucrite-diogenite breccias) presumably sample an intermediate zone or consist of material that was reaccreted and reprocessed following ejection from the parent body. If these meteorites, which constitute ~6% of all discovered falls, come from the last surviving differentiated main-belt asteroid, why are they so abundant, and how are they genetically related to the Vesta family (Binzel and Xu, 1993) or to Earth-approaching V-type asteroids (Cruikshank *et al.*, 1991)?

Reflectance spectra of basaltic achondrite meteorites are characterized by distinct olivine-pyroxene absorptions ~1 μm and a shallower, broader ~2 μm pyroxene absorption along a continuum that slopes red at visible wavelengths (Gaffey and McCord, 1978). Among large asteroids, these spectra are matched only by Vesta (Zellner *et al.*, 1985; Bell *et al.*, 1988) with other matches constituting (by definition; Tholen, 1984) the V taxonomic class. Oxygen isotopic ratios of HED meteorites follow a common fractionation line that is distinct from either Earth-Moon or Mars, and this effectively rules out origin from a terrestrial parent. (Venus and Mercury are ruled out by the absence of robust delivery mechanisms.) The prolific abundance of HED falls (Graham *et al.*, 1985; Sears and Dodd, 1988) requires either a source body with a large impact cross-section (Vesta itself) or numerous smaller V-type main-belt sources, or else one or more V-type Earth-approachers. Cruikshank *et al.* (1991) showed (3551) Verenia, (3908) 1980 PA, and (4055) Magellan to be suitable parent-body candidates: perihelion distances (1.07, 1.04, and 1.23 AU, respectively), and inclinations (10°, 2° and 24°) make the route to Earth dynamically favorable, particularly from 1980 PA.

This last candidate is particularly intriguing, considering that only three other radar-detected near-Earth asteroids have comparable surface roughness (L. Benner, pers. comm.), as evidenced by its strong circular polarization ratio $\mu_c \approx 0.75$ (Ostro *et al.*, 1991) at 3.5 and 13 cm wavelengths. This rough surface may be indicative of a recent disruptive impact (shattering and removal of fine debris) or cratering and production of ejecta blocks. Because of perceived dynamical difficulties in launching kilometer-scale rocks into Earth-approaching orbits from Vesta, Cruikshank *et al.* (1991) proposed Magellan, Verenia and 1980 PA to be remnants of a long-disrupted cousin of Vesta and not fragments from the goddess herself, who according to the myths had no offspring. I present modeling that shows how these asteroids can derive from Vesta; the basaltic achondrite meteorites might in turn derive from them. As noted by Mitchell *et al.* (1996), Vesta is itself significantly more radar-rough than the lunar surface ($\mu_c \approx 0.24$ at 13 cm and $\mu_c \approx 0.32$ at 3.5 cm), which is consistent with a body scarred by a particularly violent impact history.

Cosmic-ray exposure ages of HED meteorites range from 10 to 100 Ma (Heymann *et al.*, 1969; Drake, 1979). These ages now appear to cluster at ~22 and 38 Ma (Welten *et al.*, 1993, 1996) with little or no correlation, curiously, between age and petrographic type. These ages are not particularly great (somewhat longer than typical exposure ages of SNC meteorites from Mars); but given Vesta's location far from any planetary resonance (a = 2.36 AU, e = 0.09, i = 7°), a delivery timescale of <~100 Ma requires a chaotic "fast track" dynamical route from Vesta to Earth that utilizes Jupiter resonances (Wisdom, 1983). This makes meteorite delivery possible from Vesta, but it does not explain how 6% of *all* meteorite falls should come from a single asteroid residing in the dynamically remote center of the main belt. One would expect comparably prolific delivery from any number of other main-belt locations. Calculations by Wetherill (1985, 1987) show that the yield at Earth of impact ejecta from Vesta is orders of magnitude lower than what is needed to explain HED abundances. Comparatively brief cosmic-ray exposure ages, together with Vesta's unfavorable dynamical location, suggest a V-type source body either near Earth (Cruikshank *et al.*, 1991) or near an "escape hatch" resonance. Binzel and Xu (1993) calculate an ejection velocity of at least ~680 m/s (including escape velocity) required for Vesta surface material to reach the 3:1 Kirkwood gap (at 2.5 AU) and at least ~830 m/s to reach the ν_6 resonance that intersects the ecliptic at 2.2 AU. If we are prepared to accept that most or all HED meteorites derive from an intermediate source body (or bodies) ultimately launched from Vesta, the dynamical problem reduces to one of ejecting multikilometer pieces of Vesta at these speeds without obliterating or otherwise masking her crust.

Research concerning Vesta and the HED meteorites has gathered considerable momentum following Binzel and Xu's (1993) demonstration that most (if not all) of the Vesta dynamical family consists of asteroids spectrally similar to Vesta and the basaltic achondrites. Interpretation of recent Hubble Space Telescope (HST) and speckle interferometric images (Zellner *et al.*, 1996; Dumas and Hainaut, 1996) bring a new focus to the discussion, for these images reveal a central-peaked impact basin 460 km across (Thomas *et al.*, 1997) dominating Vesta's southern hemisphere. By modeling the impact responsible for this basin, using a modern impact hydrocode with explicit brittle fracture and gravitational self-compression (Asphaug and Melosh, 1993; Benz and Asphaug, 1994; Asphaug *et al.*, 1996a), I now show that the required collision launches multikilometer fragments at speeds exceeding escape velocity by hundreds of meters per second. We therefore *expect* to find multikilometer V-type asteroids in the dynamical environment of Vesta, and out near the resonances, and perhaps even in orbits approaching Earth, if this impact occurred recently enough for the ejected asteroids not to be eroded into small sizes by collisions (Burbine *et al.*, 1996; Marzari *et al.*, 1996). A consequent issue worth further study, but beyond the scope of this paper, is the apparent ease with which asteroids (large differentiated ones at any rate) swap material.

AN IMPACT BASIN ON VESTA

Evidence for the cataclysmic disruption of dozens of differentiated planetesimals has been inferred from the petrographic diversity of iron meteorites (*e.g.*, Keil *et al.*, 1994). These are presumed to derive from cores of disrupted primordial bodies, with Psyche and a dozen other metal-rich large asteroids constituting final relics from an epoch of violence that Vesta was lucky to survive (Davis *et al.*, 1985; Chapman *et al.*, 1989). If the catastrophic disruption of Vesta's siblings produced V-type Earth-approaching asteroids (Cruikshank *et al.*, 1991) and ultimately the basaltic achondrite meteorites, their disruption should also have subjected Earth to a comparably prolific bombardment of mantle material and populated the heavens with mantle-derived asteroids. Mantle-derived meteorites and asteroids appear to be scarce, however (Chapman, 1986; Bell *et al.*, 1989), and this discrepancy suggests basaltic achondrite ejection from a crustal source region that did not excavate much mantle rock (*i.e.*, a cratering impact into a differentiated parent body). The fate of the crusts and mantles of the catastrophically disrupted siblings of Vesta seems to be one of comminution over billions of years (in order to explain the disappearance of mantle rock; Burbine *et al.*, 1996), and this leads to the conclusion that the cratering origin for existing crustal fragments (V-type asteroids) must have been comparatively recent.

Evidence and Implications

Gaffey's (1983) rotationally-resolved spectral map, centered around the ~2 μm pyroxene band, provided the first direct evidence for a basin-forming impact on Vesta. This map reveals either a single ~100 km diameter olivine concentration (~3% of the disk-averaged surface) or a larger, less distinct feature (Gaffey, pers. comm., 1994). Current analyses of groundbased spectrometry have led to a "spot model" geology for Vesta with similar characteristics (Gaffey, 1997), and the most likely scenario is one or more regions of exposed mantle within the center of (or in the ejecta deposit from) a much larger basin. Several large lunar craters have exposed olivine-rich interiors, so this is not surprising. During the favorable 1996 May apparition of Vesta, a sequence of ~36 km/pixel five-color images were obtained with the Hubble WFPC2 (Zellner *et al.*, 1996; Thomas *et al.*, 1997) placing almost 16 pixels across the diameter of Vesta. The most prominent feature revealed by shape models (Thomas *et al.*, 1997) fitted to 1996 and 1994 HST images of Vesta is a huge 460 km impact basin centered near the south pole of the 289 × 280 × 229 ± 5 km reference ellipsoid, with correlated enhancements in 1 μm absorption. Groundbased speckle interferometry imaging (Dumas and Hainaut, 1996) refines earlier albedo maps (Cellino *et al.*, 1987) and speckle images (Drummond *et al.*, 1988; McCarthy *et al.*, 1994) and yields a profile for Vesta that is consistent in shape and phase with HST results.

A 460 km diameter central-peak crater with 13 km average depth from floor to rim (Thomas *et al.*, 1997) constitutes a significant departure from equipotential on Vesta and may have undergone viscous topographic relaxation since its formation. The persistence of a ~3% depth/diameter ratio in a planetwide basin allows a crude analysis of rheology and timescale. The Maxwell relaxation timescale τ for topography of wavelength λ on a planet with mantle/crustal density ρ, gravitational acceleration g, and viscosity η is

$$\tau \approx \frac{8\eta}{\rho g \lambda} \qquad \text{Eq. (1)}$$

(Melosh, 1989). For $\rho \approx 3$ g/cm^3 (in the upper rock) and $g \approx 30$ cm/s^2, Eq. (1) reduces (in cgs units) to $\tau \approx 2 \times 10^{-9}\eta$ for $\lambda = 460$ km. A viscosity $\eta \approx 10^{25}$g/cm/s, comparable to inferred upper mantle/crustal rheologies on terrestrial planets, gives $\tau \approx 600$ Ma, which is roughly consistent with survival timescales for ~5 km asteroids that may have derived from such a crater (the Vesta family) and with estimates (Marzari *et al.*, 1996) for the dynamical age of the Vesta family. Viscosity is widely uncertain, however, as is the collisional lifetime of a ~5 km asteroid, so this is nothing more than a consistency check.

Impact Scaling of the Crater

The 460 km final basin, relaxed or not, must be distinguished from the considerably smaller *transient* cavity that exists only during impact and whose diameter is applicable to impact scaling laws (Housen *et al.*, 1983) from which the size and speed of the impactor are derived. The hemispheric transient cavity undergoes gravitational rebound shortly after impact and widens into a "final" crater over the course of a few minutes or hours, depending on its size and the planet's gravity. Viscous relaxation, Eq. (1), thereafter widens the crater further, over hundreds of millions or billions of years, into the feature seen today on Vesta. Given the uncertainties, an expansion factor of 50% probably overestimates the size of the transient cavity, which I hereafter assume to have been of diameter $D \approx 300$ km.

This is a huge bite out of Vesta; nevertheless, craters of similar relative dimension (transient crater diameter ≈ target radius) are found elsewhere in the solar system. Consider the ~10 km diameter crater Stickney on the Martian moon Phobos: though it may seem imprudent to directly compare a minor satellite with an asteroid whose surface gravity is 50× greater, Stickney was a gravity-regime event, albeit marginally so. Asphaug and Melosh (1993) proved that Stickney could not have been a strength-controlled crater by deriving an irreconcilable conflict between strength-scaling for crater diameter and strength-scaling for catastrophic disruption. Namely, in the strength regime, Stickney's creation would have disrupted Phobos, so a crater of that size could never form. Gravity-scaling, on the other hand, leads to a picture of Stickney that is self-consistent in terms of scaling and also consistent with our understanding of rock fracture and fragmentation, crater bowl evolution, and regolith emplacement. Recent work by Thomas (unpubl. data, 1997) supports this result. The comparison between Vesta and Stickney is important because gravity-regime cratering impacts are scale-similar in the excavation stage (Housen *et al.*, 1983); thus, the survival of Phobos following the excavation of Stickney shows that Vesta would have been in no danger of obliteration during a comparable planet-shaping impact episode. More precisely, the survival of pre-Stickney stratigraphy on Phobos shows that the crust of Vesta distant from the crater epicenter would be in no danger of overturning or of loss en masse into space, a fact that is validated numerically below. See Asphaug and Benz (1994), Ryan and Melosh (1995), Asphaug *et al.* (1996a), Nolan *et al.* (1996) and Love and Ahrens (1996) for related numerical and analytical studies of gravity effects on small worlds.

BALLISTICS: IMPACT AND FRAGMENT EJECTION

Ongoing observations by the Small Main-Belt Asteroid Spectroscopic Survey (Binzel and Xu, 1993; Xu *et al.*, 1995) have substantially expanded the known Vesta family, which now includes ~250 asteroids ranging up to ~10 or more km in diameter. The sizes so far observed are truncated at ~4 km by the survey's threshold magnitude ($M_v \approx 19.5$). The majority of V-type asteroids measured by the survey have semimajor axes similar to Vesta (2.36 AU) and extend from the ν_6 secular resonance (interior to Vesta) out to the 3:1 resonance at 2.50 AU. These observations of V-type asteroids apparently trailing from Vesta, some in dynamical proximity to Earth, are thought by some to be a "smoking gun" linking HED achondrites to Vesta. If that is the case, a ballistics analogy is appropriate: we have at our disposal a fundamental data set for large-scale impact in an utterly unknown yet crucially important size regime.

These data include a size distibution inferred from small asteroid albedos (albeit subject to collisional erosion) for the Vesta family (Zappalà *et al.*, 1995), a velocity distribution similarly inferred from proper elements (Marzari *et al.*, 1996), depths of ejection inferred from spectra, with the more mafic asteroids representing samples from the deeper crust and mantle (Drake, 1979), and hand samples from the ejecta in the form of meteorites (Hewins and Newsom, 1988; Keil *et al.*, 1994 and others). It is prudent to temper this enthusiasm with the recognition that the "experiment" took place maybe one billion years ago (Marzari *et al.*, 1996; Binzel and Xu, 1993); nevertheless, such an integral complement of impact outcomes is almost never achieved during the course of even the most carefully conceived laboratory experiment. When more completely understood and appreciated, the Vesta family and the HED meteorites might allow us to answer the most stubbornly persistent questions regarding planetary cratering mechanics at a size and time scale many orders of magnitude larger than can be observed in the laboratory. These reasons alone warrant a renewed observational focus on Vesta and her kin and a host of impact models more detailed than are feasible at present.

Size of the Impactor

The primary considerations for impact modeling are impactor mass and velocity, and target structure. Characteristics of the impactor can be derived through an application of gravity-regime crater scaling (Housen *et al.*, 1983) simplified by assuming equal density for the impactor and the target crust. This is not a bad assumption, considering that the density inferred for asteroid 243 Ida ($\rho = 2.6 \pm 0.6$ g/cm^3; Belton *et al.*, 1996) is to within error the same as basalt, not to imply that Ida or candidate Vesta impactors are made of basalt. Uniform gravity g is implicit to the scaling relation, which yields impactor radius

$$r_p = 0.41 D^{1.28} g^{0.28} v_i^{-0.56} \qquad \text{Eq. (2)}$$

where v_i is the impact speed (presuming normal incidence). If the bulk density of Vesta is $\rho \approx 4$ g/cm^3, then $g \approx 30$ cm/s^2, yielding a 21 km radius projectile traveling at 5.4 km/s, using the nominal impact speed at Vesta calculated by Farinella and Davis (1992) and assuming excavation within a 2.7 g/cm^3 outer layer. This bulk density is within the range 3.1 g/cm^3 to 4.7 g/cm^3 allowed by Vesta's shape (Thomas *et al.*, 1997) and mass (Standish and Hellings, 1989). The specific velocity has no great effect provided $r_p v_i^{0.56}$ remains constant and so long as the impact is faster than the sound speed in rock. Scaling to a higher velocity will facilitate comparison with Martian cratering (below) for which impact speed is ~50% faster. The possibility of a lower-density impactor (*i.e.*, a comet) at higher velocity has been considered elsewhere (Asphaug *et al.*, 1993), but it does not appear to yield either more or faster multikilometer ejecta, at least not on the basis of low-resolution models. For the record, strength-scaling yields an ~1800 km diameter crater for this impactor striking basalt, assuming a size-dependent strength as dictated by the Weibull flaw distribution (Asphaug *et al.*, 1996a), which assures us that gravity controls this crater. Even if size-dependence of strength is ignored, the strength-scaled crater resulting from this impactor is appreciably larger than the diameter of Vesta.

To put this impact into the context of familiar objects, we are trying to understand what happens when an asteroid somewhat larger than asteroid 243 Ida strikes Vesta faster than the speed of sound in rock. The penetration phase (a few projectile-crossing times) would take >10 s, which is in dramatic contrast to the microsecond penetration time scales of the laboratory. A reader standing on Vesta's surface antipodal to the impact would have time to read the entire abstract of this paper, skim through the remainder and glance at the figures (a couple of minutes) from the moment of contact until being thrown a few kilometers above the surface. For these reasons, material response cannot be reliably understood by direct extrapolation from laboratory impact experiments in which the relevant processes (shock propagation, fracture, and fragment acceleration) are finished between one frame and the next of a high-speed research camera (cf., Nakamura and Fujiwara, 1991). Considering that strain rates antipodal to major asteroidal impacts are more akin to earthquakes than true shocks, we need models that calculate all phases of impact correctly, from the vaporization of jetted material in the contact zone to the opening of seismic fractures minutes later.

Spallation Models

The only known mechanism thought possible for launching multikilometer fragments from an airless body at hundreds of meters per second is spallation, whereby an impact stress pulse of large amplitude (a shock) interferes with its own tensile image as it reflects from the free surface boundary. Stresses cancel in the interference zone, hence the low shock levels and large fragments; whereas, stress *gradients* double, leading to enhanced accelerations. A common misperception is that spallation has something to do with material being launched from the "back side" of a target. This scenario is appropriate for armor penetration but has little to do with most planetary impacts, where the spall zone is an annulus one or two projectile radii from the impact center. The shock wave in a planetary impact radiates from an "equivalent depth of burst" several projectile radii beneath the surface, where the impactor deposits the bulk of its energy, and a component of this energy radiates upwards to the free surface, resulting in an interference zone where spallation occurs. See Melosh (1984, 1987) for the mathematical development of this model. Unfortunately, analytical expressions based on this picture of stress wave interference yield unsatisfactory results when applied to Vesta. Assuming a spall thickness of 3 km and an ejection velocity of 500 m/s (the smallest possible values for each), Binzel and Xu (1993) calculated from Melosh (1987) that a ~200–300 km diameter impactor was required, which far exceeds the catastrophic disruption threshold for Vesta. Davis *et al.* (1994) calculate that Vesta can survive impactors up to ~100 km diameter. For more realistic maximum spall thicknesses and ejection velocities (8 km, 500 m/s), the required impactor turns out to be larger than Vesta.

Our overall understanding of spallation appears to be qualitative; nevertheless, the subprocesses responsible for spallation (impact shock, stress wave interference, tensile fracture, *etc.*) can now be modeled with sufficient accuracy to incorporate them into numerical hydrocodes, which in turn can directly reproduce laboratory impact spallation experiments (Melosh *et al.*, 1992; Benz and Asphaug, 1994). With this capability, one is tempted to put the numbers characterizing the hypothesized impact into a computer model and get on with it, but our codes have only been directly tested at size and time scales (centimeters, microseconds) relevant to the laboratory. Furthermore, as demonstrated below, the outcome is sensitive to the initial conditions (*e.g.*, rheological layering) assumed for Vesta. In order to make the impact scenario for Vesta family asteroids palatable to those distrustful of hydrocodes, I precede my simulations with an analysis of a comparable impact on Mars, for which fragment sizes and speeds have been calibrated empirically.

A MARTIAN ANALOGUE: LYOT

Vickery (1986, 1987) measured the distances and diameters of secondary craters surrounding a sampling of primary craters on Mars, Mercury and the Moon, and calculated speeds (assuming a 45° ejection angle) of fragments ejected from the primary. These velocities, together with the diameters of the secondary craters formed by reimpacting fragments, provide fundamental estimates for the size-velocity distribution of ejecta. The success of this method depends on the validity of assuming 45° ejection and on the extent to which we know how to scale crater diameters for secondaries, which form in these cases at distinctly subsonic speeds. Gault and Wedekind (1969) and Fujiwara *et al.* (1989) show that impact efficiency is significantly reduced for velocities below the sound speed, which implies that Vickery's results for fragment diameter *vs.* velocity underestimate the size of ejecta blocks. Furthermore, ejection angle seems to vary with block size (F. Hörz, pers. comm.), and a 45° ejection minimizes the velocity required for a block to travel a given distance. Hence, Vickery's results may underestimate velocity as well, although distances were measured from the center of the primary rather than from the rim.

While all of the secondary crater fields studied by Vickery showed one or more instances of large blocks ejected at high speed (1 km fragments were launched at 500 m/s from craters as small as 26 km), the 227 km diameter crater Lyot in the northern plains of Mars (Vickery, 1987) may be particularly relevant to cratering on Vesta. Confirmed secondaries around Lyot were formed from blocks up to 2.5 km diameter (or larger) traveling at speeds of ~800 m/s (see Fig. 1). More than 50 secondaries from Lyot were formed by blocks >1 km, and all of these were traveling faster than 750 m/s. Blocks up to ~1.5 km diameter were ejected at speeds of 1 km/s or more; beyond this speed (*i.e.*, distance from the primary), secondary craters are not reliably distinguished from the background population. If these sizes are underestimates, fragments as large as Vesta family members were ejected during the creation of Lyot and at speeds approaching 1 km/s.

If the Lyot impactor (or its equivalent scaled to a lower velocity) struck Vesta instead of Mars, a similar size-velocity distribution of fragments might result, particularly if Vesta's basaltic crust is rheologically similar to the Martian northern plains. On the basis of Fig. 1, large fragments from the basaltic surface of Vesta would reach the resonances, or even near-Earth space, were such an impactor to strike. Target curvature might further enhance the sizes and speeds of fragments (Schultz *et al.*, 1986; Asphaug *et al.*, 1996a). A larger crater would certainly result in the lower gravity: applying constant r_p and v_i to Eq. (1) yields $D \propto g^{-0.22}$, or $D_{vesta}/D_{mars} \approx 1.7$, all else assumed equal. Using the same relaxation factor as before, we get an upper limit on transient crater diameter for Lyot, $D_{mars} \approx 150$ km. This in turn gives an upper limit for the transient cavity diameter $D_{vesta} \approx 270$ km. This diameter is close to the transient cavity size inferred earlier for the recently imaged southern basin, so multikilometer asteroids are likely to have originated from Vesta during its formation.

A recognized ambiguity in the secondary crater data is that secondary impactors may consist of aggregates following identical trajectories rather than unfragmented blocks. Of course, the same may also hold true for the asteroids comprising the Vesta family. While the Vesta family spectra are consistent with derivation from discrete units of Vesta's surface or subsurface, some appearing more mafic and others more basaltic, they may in fact be "rubble-pile" asteroids assembled from clustered ejecta fragments. Future detailed radar and multispectral observations of candidate Earth-approachers such as 1980 PA (Ostro *et al.*, 1991; Cruikshank *et al.*, 1991) may shed some light on this issue, if it turns out to be a Vesta fragment. The maximum relative velocity for debris that would clump gravitationally into an asteroid a few kilometers in diameter is a few meters per second, compared with their ~500 m/s ejection speed from Vesta, so a velocity divergence $\Delta v/v_{ej}$ of up to ~1% is allowed in the formation of such clusters. This could explain how large objects can survive brutal acceleration (in effect, they do not survive) but raises questions about the acceleration of fragments along nearly identical trajectories. Because axisymmetric impact simulations cannot model azimuthal clustering, such issues will have to wait for high-resolution three-dimensional computations, new analytical insights, and continued experimentation (cf., Martelli *et al.*, 1993).

HYDROCODE SIMULATIONS

Secondary craters around Lyot on Mars confirm that large, fast ejecta will result when a comparable impact occurs on Vesta. But how much of Vesta's crust is lost during such an episode? According to Davis *et al.* (1985), a ~42 km diameter impactor at 5.4 km/s provides <~10% of the energy required to catastrophically disrupt Vesta, and hence Vesta survives (in the sense that more than half its mass remains behind). Disruption scaling says nothing specific about retention of crust, however. The survival of severely impacted small bodies such as Phobos and Mathilde notwithstanding, numerical hydrocodes are of great benefit at this stage. Besides addressing details such as ejection velocity and fragment size as a function of position in the target, hydrocodes enable us to model target layering and composition, something that can be studied in considerably more detail than before thanks to improved codes running on faster machines.

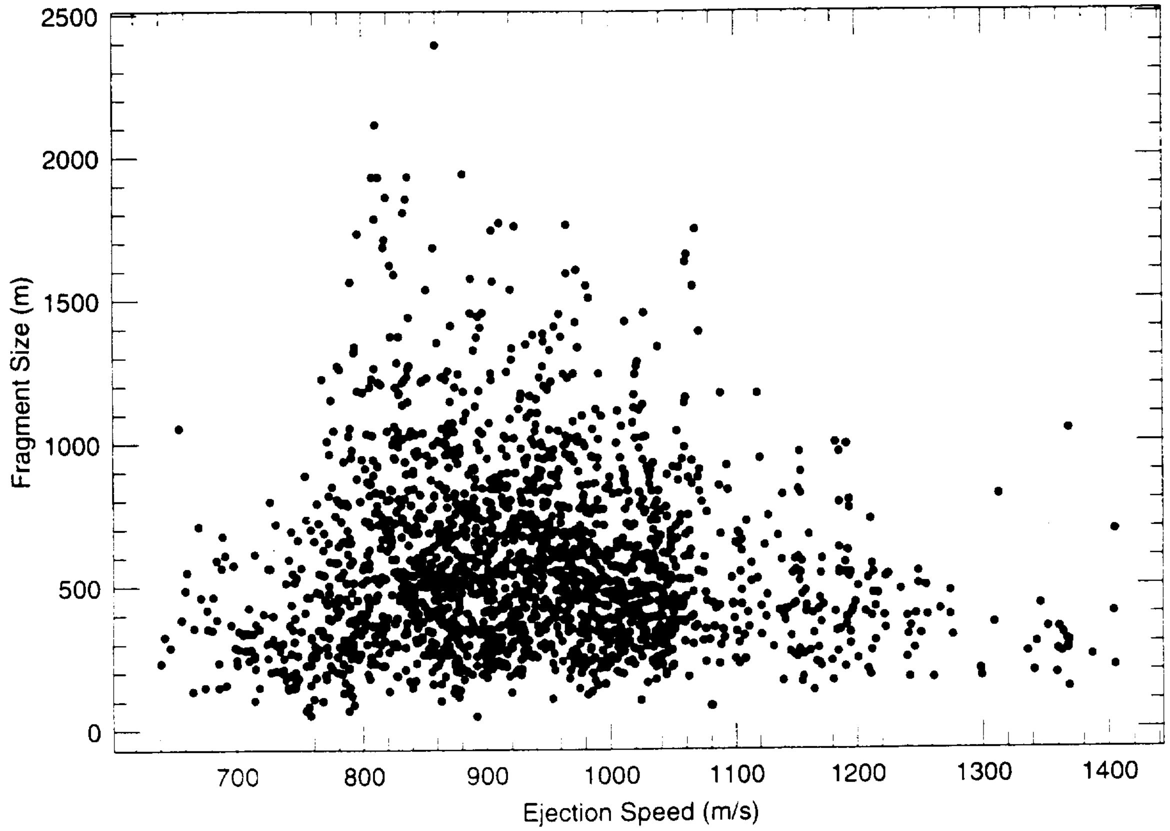

FIG. 1. Size-velocity data from Vickery (1987) inferred for secondaries produced during the formation of the 227 km impact crater Lyot in the northern plains of Mars. These estimates may represent lower bounds to fragment size. Slower, larger fragments relevant to Vesta might have landed within the boundary of the final crater and been unobservable. Data courtesy of A. M. Vickery.

Generally speaking, a hydrocode integrates the system of coupled partial differential equations governing the conservation of mass, momentum and energy. Explicit integrations proceed forward over discrete timesteps, assuming finite-difference approximations to the spatial derivatives (*e.g.*, Δt, Δx, Δy, and Δz. A finite volume element bounded by $\Delta x \times \Delta y \times \Delta z$ is called a "cell" of the calculation. (In two dimensions, a cell is usually either bounded by $\Delta x \times \Delta y \times 1$ in planar symmetry or $\Delta x \times \Delta y \times r\Delta\theta$ in axisymmetry, employed below.) An equation of state relating pressure, energy and density formally closes the system of equations, although a constitutive equation such as Hooke's law is required for solids, together with a yielding relation (plasticity or brittle fracture) that may itself depend on internal energy and stress. The Tillotson (1962) equation of state is employed in this study (see Table 1 and Melosh, 1989). The constitutive and yielding relations determine the stress tensor, of which pressure (from the equation of state) comprises the trace. In the case of impacts and other hypervelocity phenomena, shock waves (discontinuous by definition) must be "smeared out" using artificial viscosity (von Neumann and Richtmyer, 1950). Much recent effort (Melosh *et al.*, 1992; Asphaug and Melosh, 1993; Benz and Asphaug, 1994, 1995; Mandell and Wingate, 1994) has been devoted to the task of deriving stable and accurate systems of equations describing the impact failure of brittle solids, and the field remains a young and active one.

The code used here is an explicit Lagrangian integrator (Amsden *et al.*, 1980) with a yielding and fragmentation model. Details are found in Asphaug *et al.* (1996a) and the appendix therein. While this code and its relatives have been extensively tested against controlled laboratory experiments (Melosh *et al.*, 1992; Benz and Asphaug, 1994, 1995), it remains imprudent to blindly trust these calibrations across ~6 orders of magnitude in size. Detailed studies of astronomical "targets" such as Ida, Phobos, Vesta, Toutatis and Mathilde enable increasingly reliable extrapolations, and the present work (with its caveats) is an early effort in that direction. Underground nuclear tests provide some leverage of code results to scales where geological rock properties dominate (faults and joints, lithostatic compaction, *etc.*), and the particle velocities derived from this code are in good agreement with weapons tests for a variety of bedrock types on scales of kilometers (Asphaug and Melosh, 1993). Nonetheless, the nominal Lyot impactor carried an energy of half a billion megatons, which is far beyond the scope of any simple extrapolation.

TABLE 1. Elastic constants and Weibull parameters.

Layer	Material	K dyn/cm^2	μ dyn/cm^2	ρ g/cm^3	m	k cm^{-3}
crust/impactor	basalt	2.67×10^{11}	2.67×10^{11}	2.7	9.0	4.0×10^{29}
upper mantle	anorth. lpp	7.10×10^{11}	2.67×10^{11}	2.9	3.0	1.4×10^{12}
lower mantle	anorth. hpp	2.40×10^{12}	2.67×10^{11}	4.0	9.1	5.0×10^{22}
core	iron	1.28×10^{12}	2.67×10^{11}	7.9	—	—

See Melosh *et al.* (1992) for a compilation of Weibull fracture coefficients and Tillotson equation of state parameters for these and other rock types. The shear modulus for anorthosite is presumed sufficiently close to that of basalt given the grosser approximations being made regarding mantle rock. Fracture is not computed for the core, whose deformation and stress state is modeled according to an elastic-plastic relation.

Damage and Fragment Statistics

Damage is computed using the method of Benz and Asphaug (1995), which is founded on the same underlying assumptions as Grady and Kipp (1980) and Melosh *et al.* (1992) but which incorporates realistic cell-to-cell stochastic variations in the flaw distribution for the target rock. Flaws in the rock are assumed to obey a power-law distribution $n(\epsilon) = k\epsilon^{m}$ (Weibull, 1939; Melosh *et al.*, 1992) where m and k are material-specific constants derived from dynamic strength tests and n is the number of flaws (per volume) with activation threshold at or below a strain ϵ. Benz and Asphaug (1995) allow strain rate to vary with time during fracture and allow for size-dependent strength without invoking unphysical flaw distributions whose statistics vary with target size or resolution. Cells lose strength as explicit subflaws within them fail, one by one, in response to the current stress. This strength reduction is called *damage*, which ranges from 0 (rock) to 1 (rubble), and equals the sum of the stress-relieved subvolumes encompassing each active flaw divided by the total volume of the cell. Damage alters the constitutive properties of the rock transmitting the stress (elastic modulus, sound speed, *etc.*), and this leads to a complex system. Once damage begins locally, further strains concentrate there due to the softened elastic modulus. Stress concentration at the macroscale drives crack tips forward (*cf.*, Lawn and Wilshaw, 1975), and planar shocks become convoluted due to constitutive fluctuations in rock that undergoes damage. If loading continues to increase in spite of stress release (an imbalance governed by the strain rate *vs.* the crack growth speed), then cracks coalesce until the material behaves macroscopically as a fluid (damage = 1). The computation of fracture damage is the most numerically intensive aspect of these calculations but is essential. Even if we did not care how much rock is broken by the impact or into what sizes, dynamic fragmentation has a dramatic effect on the shape and definition of the impact shock wave, leads to very different particle velocities following the impact, and very different ejecta velocity distributions and crater shapes and sizes.

Where sufficiently high resolution is possible, "real" (or explicit) fractures form as one hydrocode cell after another fails in a crack-plane geometry governed by macroscopic stress concentration (Benz and Asphaug, 1995). Explicit fragments are created as contiguous zones of unbroken rock surrounded by cells of totally damaged material. But numerical resolution is typically too coarse to resolve fragments in such a manner, so we resort to the statistics of flaw activation and coalescence from which formulas for fragment size (Grady and Kipp, 1980) have been derived. These statistical expressions are accurate so long as the stress wave is faithfully resolved (shown by Melosh *et al.*, 1992), which is an unavoidable assumption at present. The smallest possible *explicit* fragment (bounded by damaged cells) is several times larger than the hydrocode resolution, and any ~10 km or smaller asteroid deriving from Vesta (Table 2 and Figs. 2–8) will therefore be a statistical entity given the current resolution of 100 × 200 cells. (Each two-dimensional cell is a torus circling the symmetry axis of volume ~2.7 km × 2.7 km × $2\pi r$, so the resolution is effectively even coarser than implied, especially away from the poles.)

Grady and Kipp (1980) derive fragment size from the spacing of coalesced Weibull flaws in the aftermath of damage. Fragment size in their model is a linear function of the power of strain rate $\dot{\epsilon}^{-m/m+3}$, where $\dot{\epsilon} = d\epsilon/dt$ is the strain rate, assumed constant, and m is the Weibull exponent defined above. Because strain rate varies during the course of failure, I compute the time-average of $\dot{\epsilon}^{-m/m+3}$ and plug this value into the Grady-Kipp equation, having used this technique previously to reproduced the laboratory benchmarks of Melosh *et al.* (1992). The fragment size algorithm of Melosh *et al.* (1992) is effectively identical to my technique of sampling the average of $\dot{\epsilon}^{-m/m+3}$ during failure but is formally linked to their statistical algorithm for fracture damage and cannot be directly employed here. An obvious goal of future research is to move entirely beyond statistical fragments with hydrocode grids containing millions of cells.

Initial Conditions

Self-Gravity–The mean diameter of Vesta (~530 km) gives a total volume ~7.8 × 10^{22} cm^3, and its total mass (based on a presumed density ~4 g cm^{-3}) is $^1/_{20\,000}$ $M_{\oplus}$, or ~3 × 10^{23} g. Internal pressures approaching 2 × 10^9 dyn/cm^2 (20 kbar) must be included when modeling an impact that penetrates the deep interior. The vector accelerations of self-gravity need not be computed for the early stages of any impact into Vesta, however. We can evolve the hydrodynamical calculation in one phase (until ejecta flow velocities are established and the shock has dissipated, *i.e.*, a few minutes on Vesta) and then examine the gravitational accelerations as an entirely separable phase of the impact, provided we incorporate the self-gravitational stress state as an initial condition.

A separable calculation is possible whenever the gravitational timescale (Binney and Tremaine, 1987) is much greater than the impact timescale. In order for impact ejecta to land ahead of the primary stress pulse, the orbital velocity must exceed the sound speed. For the fastest bound ejecta to race along at the speed of sound, $c_s \approx \sqrt{GM/R}$. In terms of typical numbers, this relation yields

$$R \cong 5000\ \mathrm{km}\left(\frac{c_s}{5\ \mathrm{km/s}}\right)\sqrt{\frac{3.5 g/\mathrm{cm}^3}{\rho}} \qquad \text{Eq. (3)}$$

where R and M are the radius and mass of the asteroid, and ρ is the mean density. For global collisions into any rocky object considerably smaller than the Moon, we can therefore incorporate gravity as an overburden strength in a manner similar to Davis *et al.* (1985), although as a radially dependent strength parameter rather than a global one. We thereby avoid a direct computation of the vector accelerations of gravity until after impact fragmentation and shock acceleration is complete. Our method (Asphaug and Melosh, 1993) establishes a radius-dependent strength $\sigma_f(R) = \sigma_0 + {}^2/_3\pi G\rho^2(R-r)^2$, where σ_0 is the native tensile strength of the material, R is the radius of Vesta, and r is the distance of a given hydrocode cell from the target center. (In the Benz-Asphaug explicit failure model used here, hundreds of thresholds $\sigma_{0,i}$ exist within each cell, and all of the discrete thresholds are boosted by the same radius-dependent amount.) For targets the size of Vesta, material strength is small compared with the gravitational overburden several tens of kilometers below the surface, and the strength model is really only relevant to the crustal and upper mantle rocks. Overburden also affects the manner in which rocks break and can lead to enhanced sizes at depth.

Internal Structure

Three points distinguish this work from prior hydrocode analyses of Vesta impacts (Asphaug *et al.*, 1993; Asphaug, 1994). First of all, there is an observed crater to model, making impactor assumptions less arbitrary. Second, much higher resolution is available on modern workstations, allowing for more accurate determination of shock fracture and acceleration. Third, refinements to the code allow for multiple material types, including crust, mantle and core. These

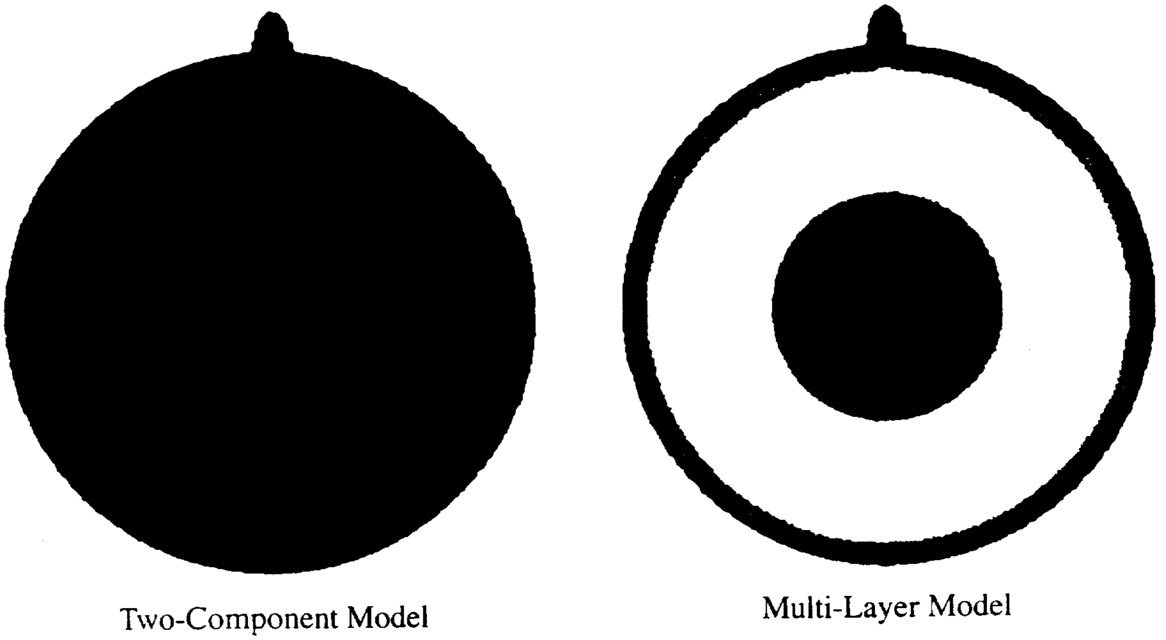

FIG. 2. Initial conditions for high-resolution two-dimensional axisymmetric Lagrangian hydrocode runs, in which a ~21 km radius 2.7 g/cm^3 asteroid (top) impacts a gravitationally compressed Vesta at 5.4 km/s, which is equivalent in energy to a ~400 million megaton explosion. Numerical resolution is 100 × 200 cells. Each target has a 120 km radius iron core and an outer radius 270 km, which is larger than the current mean radius but smaller than a circumscribing sphere. (a) A two-component model, consisting of 2.7 g/cm^3 basalt above the core. (b) A more plausible multilayered model with ~10 km basalt crust, ~15 km thick 2.9 g/cm^3 upper mantle, and 4.0 g/cm^3 lower mantle above the core. Escape velocity for the denser multilayered target is 400 m/s; gravitational acceleration is ~30 cm/s^2 and central pressure is ~2 × 10^9 dyn/cm^2 (20 kbar). The mass of Vesta is ~3 × 10^{23} g.

advances enable an exploration of specific differences in target structure, and it turns out that heterogeneous surface layering is more important than previously supposed. Two "end-member" Vestas (together with a coarser model for late-time analysis) have been constructed for the current study: one with no crustal/mantle distinction and another with a crust/mantle boundary at ~10 km depth.

Figure 2a and b show the initial condition hydrocode grids for each of these targets. Each has a 270 km radius, which is larger than the current mean radius of Vesta but smaller than a circumscribing sphere, accounting for impact-induced alteration of Vesta's original shape. The protuberance shown at the top of each target is the 5.4 km/s, 42 km diameter impactor, already somewhat flattened at time $t = 0$ in an effort to combat numerical instabilities. Crustal rocks, and also the impactor, are modeled as basalt (2.7 g/cm^3), which is well calibrated for impact studies by Nakamura and Fujiwara (1991). The target on the left lacks any crust/mantle interface and consists of basalt all the way down to a 120 km radius iron core (7.9 g/cm^3, ductile but no fracture). The target on the right is more plausible and, as it turns out, much more interesting in that it results in considerably larger and faster fragments. It consists of a 10 km crust atop a 15 km upper mantle, atop a lower mantle that extends to the core. Upper and lower mantles in this second target consist of 2.9 g/cm^3 and 4.0 g/cm^3 phases of anorthosite, respectively, for lack of more suitable candidate rocks for which equation of state parameters and fracture constants are known. Fracture constants for both phases of anorthosite are reported in Ahrens and Rubin (1993). Escape velocity for the multilayered Vesta model is 400 m/s.

Layering in the second target corresponds loosely to constraints proposed by Gaffey *et al.* (1993) on the assumption of bulk chondritic composition, although the actual structure of Vesta is likely to differ in substantial ways. The mantle rocks will behave differently, although density (the most important equation of state parameter) is probably adequately represented by anorthosite. Of greater concern are the fracture constants (m and k) used for the various layers, which derive from laboratory experiments into terrestrial analogues. Basically, a few measurements of strength as a function of strain rate are sufficient to pin these numbers down reasonably well, but the measurements are difficult to perform and not always straightforward to interpret (cf. Lange and Ahrens, 1983; Ahrens and Rubin, 1993; Grady and Kipp, 1980). The low Weibull exponent $m = 3$ for the low-density phase of anorthosite (upper mantle) may be problematic, because m is the exponent that leads to size-dependent strength, and $m = 3$ may lead to excessively small fragment sizes. We might better constrain these numbers for Vesta once meteorite curators, in a moment of weakness, allow their specimens to be the subject of catastrophic impact experimentation. However, meteorites at Earth have been highly selected on the basis of their ability to survive brutal acceleration from an asteroid or planet, followed by millions of years of travel through space and violent entry through a substantial atmosphere onto a hard planet surface. Improving impact models is therefore not an obvious matter of plugging in numbers derived from meteorites unless we can correct for such biases. The most useful calibration may in fact come from iteratively improving our models based on specific simulations of large-scale impact features on asteroids, such as the current effort.

Hydrocode Results

Two high-resolution (100 × 200) calculations each executed ~10 000 timesteps to halt at $t = 32$ s, which is sufficient to serve the primary goals of this study but not sufficient to examine effects in the distal hemisphere of Vesta. A companion simulation at coarser resolution (30 × 60) was therefore run to much later time (9 min), which is sufficient for the impact shock to dissipate after four traversals of the target. At coarse resolution, the shock is too broad to produce the

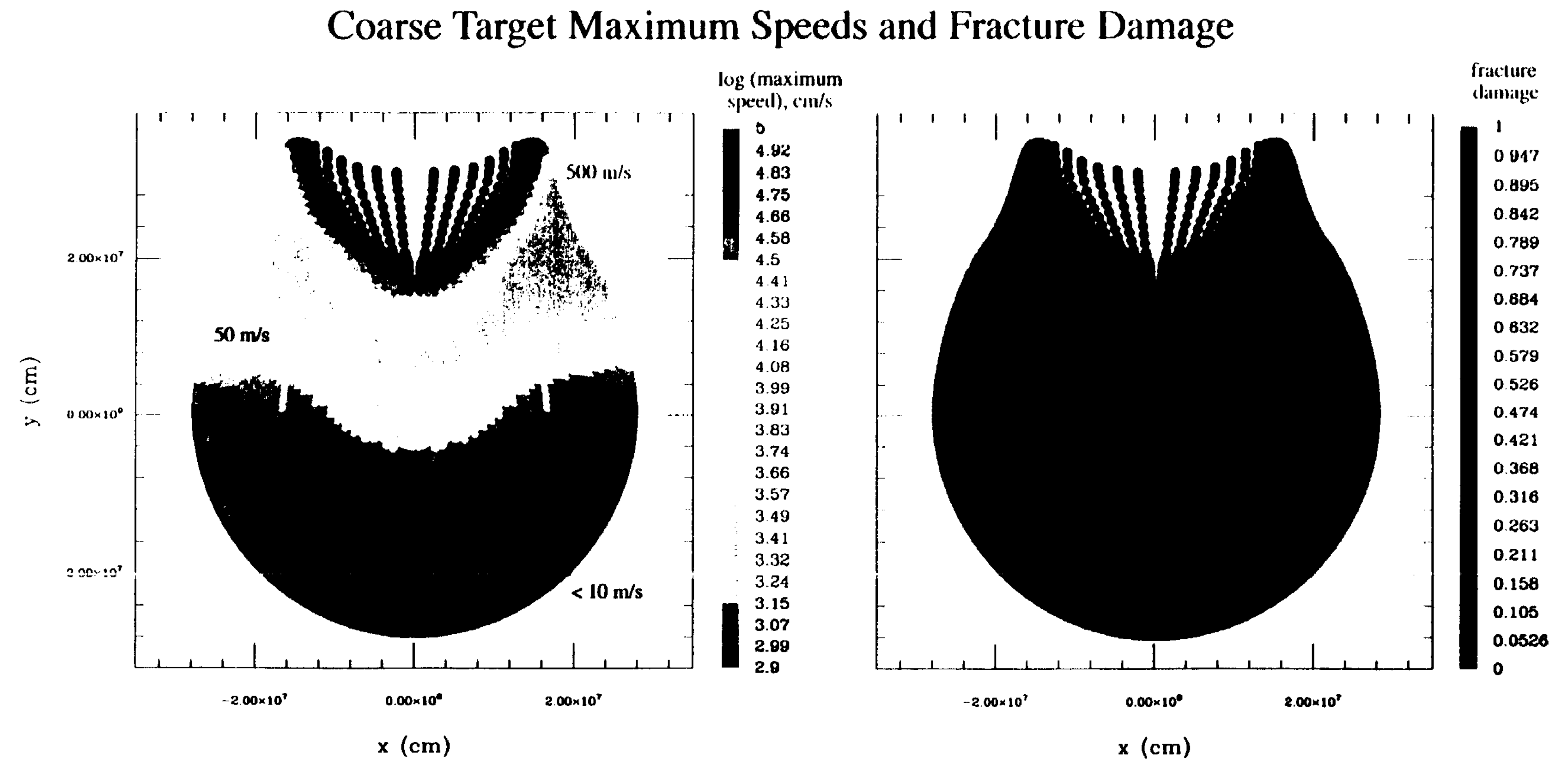
Coarse Target Maximum Speeds and Fracture Damage

FIG. 3. In order to model the impact to late time, a comparison target was constructed at coarse (30 × 60) resolution using initial conditions similar to Fig. 4b (multiple layers). A logarithmically spaced grid was employed, with greater resolution nearer the surface. This has advantages and disadvantages (see text). (a) Velocities inside the target 9 min after impact. Particle velocities in the distal hemisphere are far lower than what is required to overturn a crust. (b) Damage levels inside the target. Most of the mantle and crust is broken, but fragment sizes are large ($\gtrsim$ 10 km) and speeds low ($\lesssim$ 10 m/s) in the distal hemisphere.

near-surface spallation effects required for large, fast fragments. The coarse model leads to accurate results for late-time particle velocities throughout the bulk of the target, however, and is briefly presented first as evidence for the survival of Vesta's crust.

Coarse Target–In order to resolve a crust/mantle boundary at 30 × 60 resolution, a logarithmic grid spacing is employed in this target, with finer resolution near the surface. This method has certain obvious advantages; in particular, the outer layers can be represented somewhat faithfully. But the projectile/target interface is potentially unstable, precluding its use in the 100 × 200 target below. The initial coarse target has a four-layered structure almost identical to Fig. 2b, and the impactor is the same size and speed. Figure 3a plots the maximum particle velocities achieved in the coarse-resolution target from the moment of impact until 9 min after the collision. Although near-impact velocities exceed escape velocity, little material in the distal hemisphere of Vesta is accelerated faster than ~10 m/s. Even if launched optimally from the surface, this speed carries material only a few kilometers. An ejection speed of ~50 m/s is needed to overturn a ~10 km crust with $g \approx 30$ cm s^{-2}: the impact is not even marginally catastrophic. Figure 3b plots fracture damage in the same target, also at $t = 9$ min. Fracture is not calculated in the ductile iron core. All of the crust and nearly all of the mantle are fragmented into sizes ranging from centimeter to kilometer (in the near-impact hemisphere) to many tens of kilometers in distal regions. While this may technically count as catastrophic disruption according to some (in that ~70% of the target is "broken"), the sizes of fragments (many kilometers) and their relative speeds (meters per second) do not amount to noticable disassembly of the target body except in the vicinity of the crater.

Multi-Layered High-resolution Target–Higher resolution models (100 × 200) yield more detailed results. Uniform grid spacing also results in a more stable calculation where the projectile encounters the target. Impact into the monolayer Vesta (Fig. 2a) yielded no fast, large fragments. At best, one cell with mean fragment size ~0.4 km was ejected at 466 m/s in this simulation. While this null result is interesting in its own right, a ~150 km deep monolithic basaltic crust is unrealistic, and a more detailed surface model is certainly justified. Impact into the multilayered Vesta target (Fig. 2b) yielded copious large, fast spalls that are consistent with an impact origin for the Vesta family of asteroids, which suggests that target heterogeneity plays a dramatic role in the ejection of meteorites.

Figure 4 shows the shock wave beginning its penetration into the core of the multilayered target at $t = 32$ s, at the time the simulation ends. Shades of grey plot pressure in a linear scale ranging from tensile (black) to 10^{10} dyn/cm^2 = 1 GPa at the center of the detached shock. This maximum pressure is considerably lower than the peak pressure during the contact phase but remains strong enough to disrupt rock. The detached shock is beginning to cross the denser,

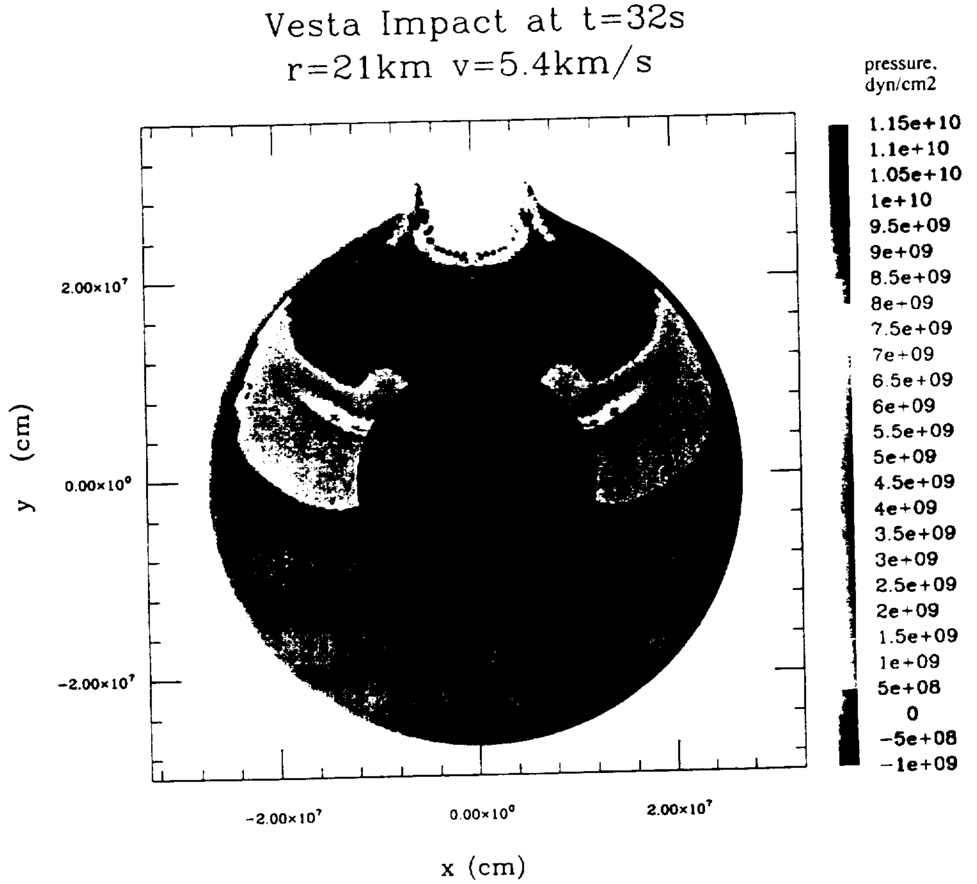

FIG. 4. The shock wave propagating through the high-resolution multilayered target 32 s after impact. The shock has entered the iron core, and a rarefaction follows close behind. Note the zeroing of pressure at the free surface. The transient cavity is 100 km in diameter and growing. By this point, fracture damage and accelerations in the spall zone are complete, although impact stresses continue to cause damage far from the crater. The scale bar ranges linearly from <−1 kbar (black = tensile) to >12 kbar (compressive). The iron core is darkened.

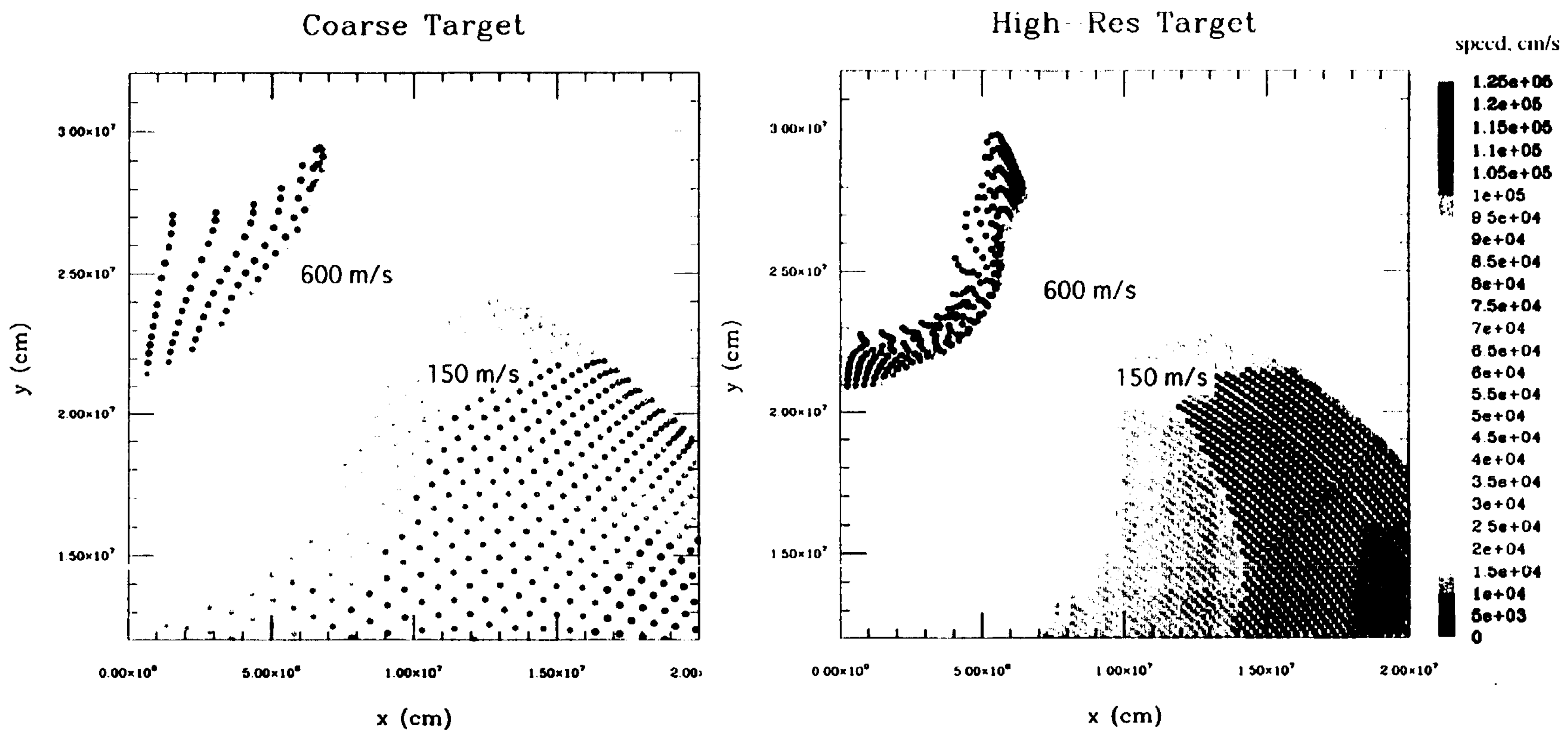

FIG. 5. Maximum speeds achieved in both the coarse target and the high-resolution multilayered target at $t = 32$ s, scaled from <50 m/s to >1.25 km/s, in a zoom of the impacted quadrant. Except for enhanced vaporization in the impact point for the coarse target (an artifact of logarithmic spacing), results are similar. Note the significant velocity enhancement in the near-surface zone of the high-resolution model; however, this provides the fragment sizes and speeds required for the Vesta family.

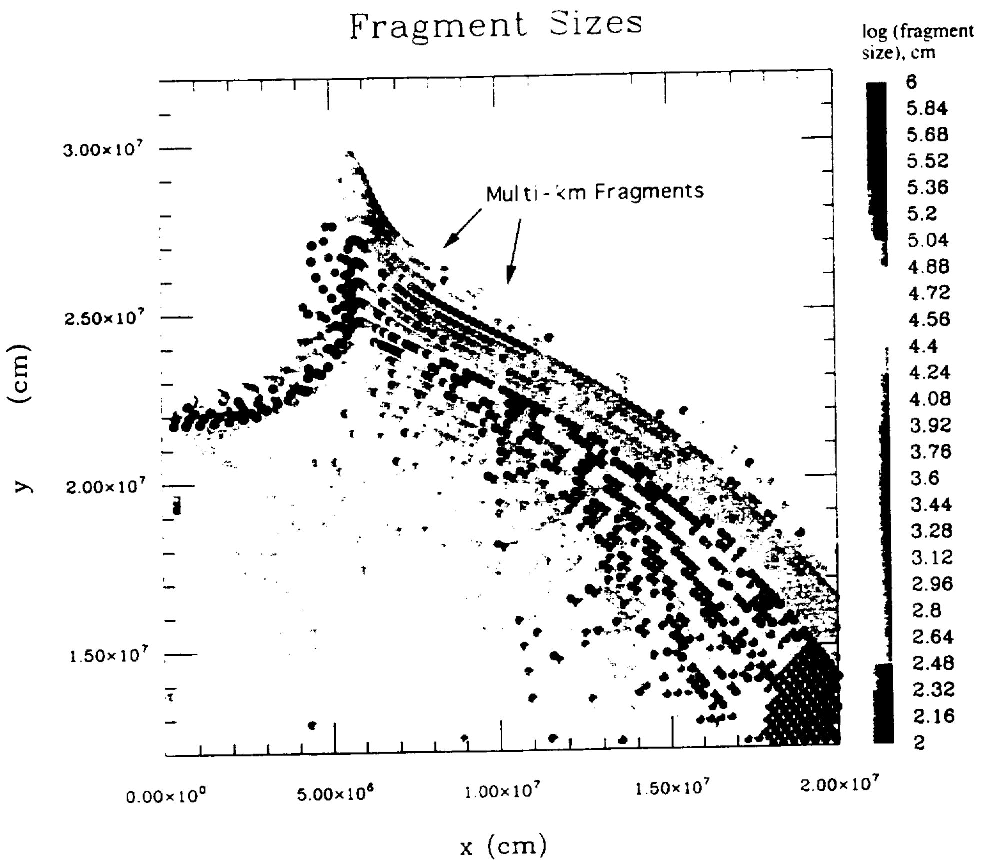

FIG. 6. Fragment sizes in the impacted quadrant of the multilayered high-resolution Vesta target. Black fragments (2 on the scale bar) are projectile materials broken into pieces $<10^2$ cm. Of particular interest are the multikilometer fragments (5 to 6 on the scale bar, or 10^5 to 10^6 cm) contained within cells near the "shoulder" of the impact. Fragments of this size and speed did not form in the two-component Vesta model, which implies that stress interference at crust/mantle boundaries is important. Table 2 provides more specifics about fragment location and velocity.

lower-velocity core (darkened in the figure) whose outline traces a discontinuity of stress gradient. The rarefaction that follows a radially expanding shock wave (cf., Melosh *et al.*, 1992) approaches the core/mantle boundary. The transient cavity of the evolving impact crater is ~100 km across and continues to expand rapidly. (Cavity deformation causes the Lagrangian code to slow down dramatically beyond this point and is responsible for the early termination of this run.) All of the shock fragmentation and acceleration of near-surface materials in the vicinity of the crater is finished by this point, however, so in conjunction with the coarse Vesta model, we have all the results we need. Maximum pressure sustained within the "interesting" fragments (large ones near the surface) is lower than the fracture strength of the rock and much lower than could lead to any discernable shock effects. This is consistent with the low shock levels observed in HED bulk rocks (Stöffler *et al.*, 1988).

Figure 5a and b plots snapshots of maximum speeds achieved as a function of position in the target at t = 32 s, from <50 m/s to >1.25 km/s, for the high-resolution target (right) and the coarse target (left), included for comparison. These views show only the impacted hemisphere and only one half of the symmetry plane. Velocities increase monotonically from the lower right towards the crater center. Speeds in the interior are similar for both models, but speeds near the target surface are significantly enhanced in the high-resolution model. In the latter case, shock waves are sufficiently well resolved to interfere with their tensile image (Melosh, 1984, 1987) and double in gradient, which leads to more powerful accelerations and a bending of velocity contours away from the crater.

Figure 6 plots resultant fragment sizes for the high-resolution simulation. Fragment size does not vary monotonically, as evidenced by the checkerboard pattern near the surface. For comparison, fragment sizes, speeds and locations are listed in Table 2. A number of cells along the "shoulder" of the impact contain fragments a few kilometers across and lie in the high-velocity interference zones of Fig. 5b or near the upper lower mantle discontinuity. The outer three rows of cells (~10 km) consist of basalt (parent material to eucrites), while the next five rows of cells (~15 km) are upper mantle. The rest is lower mantle; the core is just out of view beyond the lower left corner of the plot. Fracture behavior in the upper mantle is quite different from that of the crust on account of its lower Weibull constant $m = 3$, discussed above (Table 1).

Fragment Statistics and Comparisons–All in all, ~100 fragments >2 km and 10 000 fragments >1 km escape Vesta in this simulation. The single largest escaping fragment is ~15 km across. Table 2 lists results for all hydrocode cells containing fragments >1 km at speeds >400 m/s. Initial conditions for the multilayer target were not "tuned" in any way to yield fast, large spalls but were based on impactor sizes and speeds and target structures most consistent with crater scaling rules, asteroid encounter velocity estimates, and mineral-

TABLE 2. Fragments ejected from Vesta.

Speed (m/s)	Size (km)	Quantity	Type
408	15.0	0.7*	H/D
461	2.6	117	H/D
570	2.2	10	H/D
406	1.6	450	H/D
564	1.6	457	H/D
454	1.5	1115	E
429	1.3	833	H/D
434	1.3	1165	H/D
493	1.3	915	H/D
448	1.2	1142	H/D
528	1.2	1233	H/D
598	1.2	61	H/D
554	1.1	2058	E
628	1.1	91	H/D
459	1.0	1990	H/D

*One 15 km escaping fragment is 70% likely to have formed (see text).

Many cells in the multilayer hydrocode simulation achieve escaping velocities ($v_{esc} \approx 400$ m/s). For the complete size-velocity distribution, see Fig. 6; tabulated here are cell-averaged results for fragment speed, fragment size, total number of fragments, and petrographic type for cells ejected faster than 400 m/s. The largest fragment to escape Vesta is a 15 km asteroid; ~100 fragments >2 km and 10 000 fragments >1 km are ejected faster than 400 m/s. The fourth column tells whether the ejected material comes from the mantle (H/D) or the crust (E). The most *plentiful* fast fragments >1 km come from the crust (E), but in general, the *fastest* fragments come from ~10 km, or half a projectile radius, beneath the surface (H/D). The largest 15 km escaping fragment, surprisingly, derives from the mantle. This result agrees with Binzel and Xu's (1993) observations that Vesta family asteroids most distant from Vesta tend to have diogenitic spectra but remains difficult to explain in terms of existing spallation models. All ejecta faster than 628 m/s are of sizes <1 km.

ogical/evolutionary constraints (*e.g.*, Housen *et al.*, 1983; Farinella and Davis, 1992; Drake, 1979; Gaffey, 1993). Given that two-dimensional axisymmetry requires a normal incidence angle and that numerical resolution of these studies is marginal, we might expect faster and larger spalls in nature where smoothing and symmetry do not apply. Table 2 shows that the fastest multikilometer fragments derive from mantle rocks and not from the crust. It is worth noting that the basaltic family asteroids most distant from Vesta (in dynamical space) have spectra resembling diogenites rather than eucrites, a fact which prompted Binzel and Xu (1993) to coin the "J" spectral type. While the mantle rock fracture constants are only a fair assumption at best, the trend in the simulation is consistent with astronomical observation.

Figure 7 plots the fragment size distribution following the event, for those fragments moving between 300 and 650 m/s and >100 m. (No fragments >~1 km are accelerated faster than 650 m/s.) The scale bar plots the number of fragments in each cell, ranging from 1 to 10^6. The range is essentially monotonic, with the greatest numbers corresponding to the smallest fragments. Millions of >100 m fragments, hundreds of >1 km fragments, and a single >10 km fragment are ejected at escaping speed. This largest fragment (15 km) derives from below the upper crust, and therefore its ejection speed will be modified as the crater bowl evolves. The fastest fragments come from approximately half a projectile radius (~10 km) below the surface (Table 2), and their speeds will therefore be reduced if they are overlain by slower debris. However, as Fig. 5 indicates, ejection velocity increases towards the surface, so this may be a moot point. Nevertheless, the final, hydrodynamically evolved velocities for the fragments will remain uncertain until computations are performed to much later time on faster computers with algorithms including explicit gravitational acceleration.

The final plots show statistics of the outcome for the high-resolution layered target. The 15 largest escaping fragments produced in this study are plotted in a size *vs.* ejection velocity plot (Fig. 8) together with the inferred sizes and velocities of Vesta family members (Binzel and Xu, 1993) and inferred ejection sizes and speeds based on secondary counts from the Martian crater Lyot (Vickery, 1987). Only escaping fragments are shown; Binzel and Xu (1993) assume a somewhat lower escape speed than used here. The Lyot impact involves a somewhat faster (~8–10 km/s) projectile onto a flat surface and may, therefore, have produced smaller, faster fragments than a basin-forming impact on Vesta. Comparison with Binzel and Xu's (1993) data for Vesta family asteroids suggests that fragment sizes might remain underestimated in this two-dimensional axisymmetric calculation. This is not surprising considering resolution constraints and rheological approximations: comparison with the two-component Vesta model shows how sensitive ejecta size and speed is to surface structure. Figure 9 plots summary outcome statistics for the high-resolution layered target. While these graphs are self-explanatory, it is worth pointing out that a cumulative size-frequency distribution slope of ~ -4 is steeper than anticipated from catastrophic disruption scenarios yet consistent with crater bombardment rates in the main belt. In Fig. 9b, all V and J type asteroids tabulated by Binzel and Xu (1993) have been plotted for comparison. The match would be considered good if it were a hydrocode fit to a laboratory impact experiment (Melosh *et al.*, 1992; Benz and Asphaug, 1994), although sizes between 3 and 10 km are missing in the model outcome. Model resolution for shock and explicit fracture falls across these missing sizes, and one direction for future work is therefore clear.

CONCLUSIONS

The mystery of Vesta will not be solved until we understand how this asteroid managed to retain most of its crust while dozens of comparable bodies were apparently destroyed (Davis *et al.*, 1985). Had Vesta suffered a similar fate, basaltic meteorites might be as rare in our collections as the notoriously absent olivine-rich mantle rocks (Chapman, 1986; Grady, 1995). Basalt is neither significantly stronger than dunite nor produced in greater abundance during core-stripping catastrophic breakups; therefore, the skewed abundance of basaltic meteorites suggests a noncatastrophic source event that preferentially launched surface materials into space, a crater on Vesta for example (Consolmagno and Drake, 1977). Smaller V-type candidates trailing from Vesta to the "escape hatch" resonances (Binzel and Xu, 1993) and perhaps into near-Earth space (Cruikshank *et al.*, 1991) suggest a secondary source for basaltic achondrites, a view which may be easier to accept in light of the relatively short exposure ages. Little or no correlation exists between HED petrographic type and exposure age in the data of Welten *et al.* (1996), however, so if the ~22 and ~38 Ma peaks record two specific impacts (from whatever parent body), then each impact appears to have launched all three kinds of meteorites towards Earth.

This implies one of three scenarios for an HED parent body: (1) an Earth-approaching asteroid containing eucrite, diogenite and howardite material was launched from Vesta during the impact that created the observed 460 km basin; (2) a similar asteroid was ejected during the same event into close proximity of a resonance; or (3) one

FIG. 7. (Right) Size *vs.* velocity for fragments >100 m ejected between 300 and 650 m/s. This range includes all escaping fragments >~1 km. Each disrupted hydrocode cell (each point) contains a number of fragments determined by the cell's volume and its mean fragment size; this number (shading) ranges from 0.7 (the probable 15 km escaping fragment, 0 on the scale bar) to millions (6 on the scale bar) of ~100 m rocks.

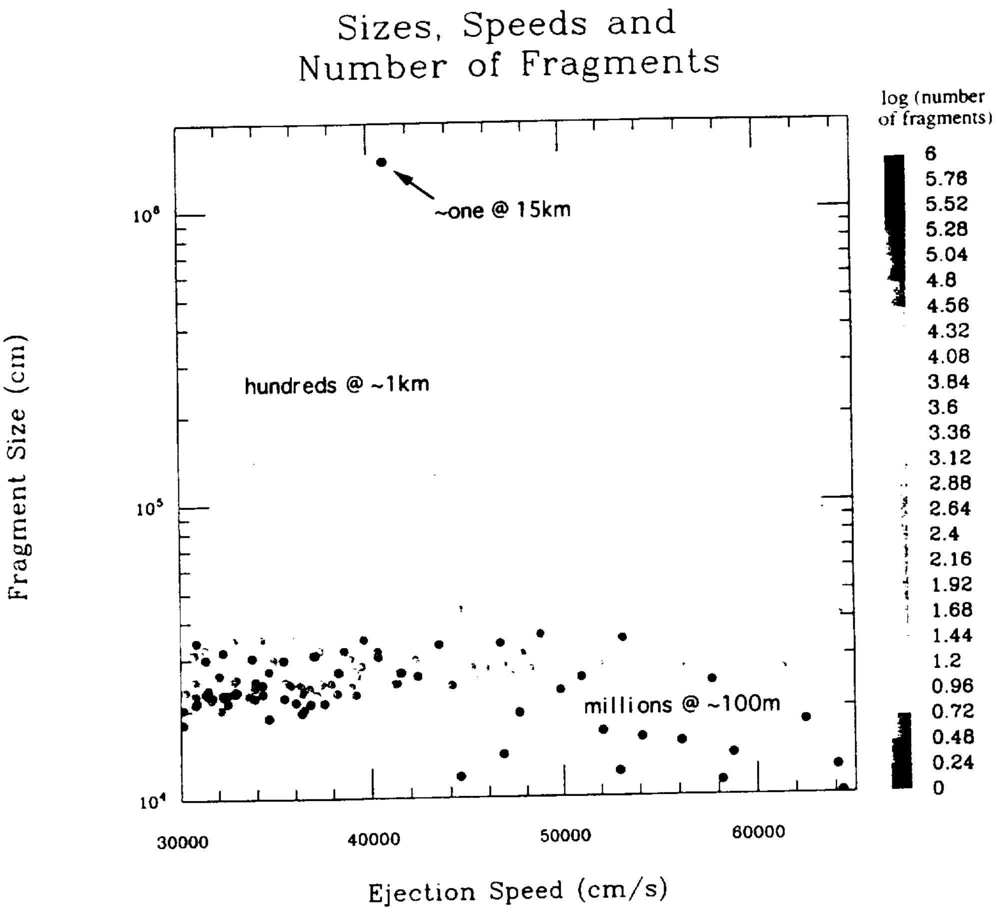

FIG. 8. (Below) Size vs. velocity from the multilayered hydrocode result (triangles) plotted together with Vickery's (1987) data for ejecta from the impact crater Lyot (small dots) and Binzel and Xu's (1993) estimated sizes and ejection velocities for 20 Vesta family asteroids (circles). Only the 15 largest fragments from the hydrocode are plotted. Binzel and Xu (1993) have an observational cutoff for objects <~4 km.

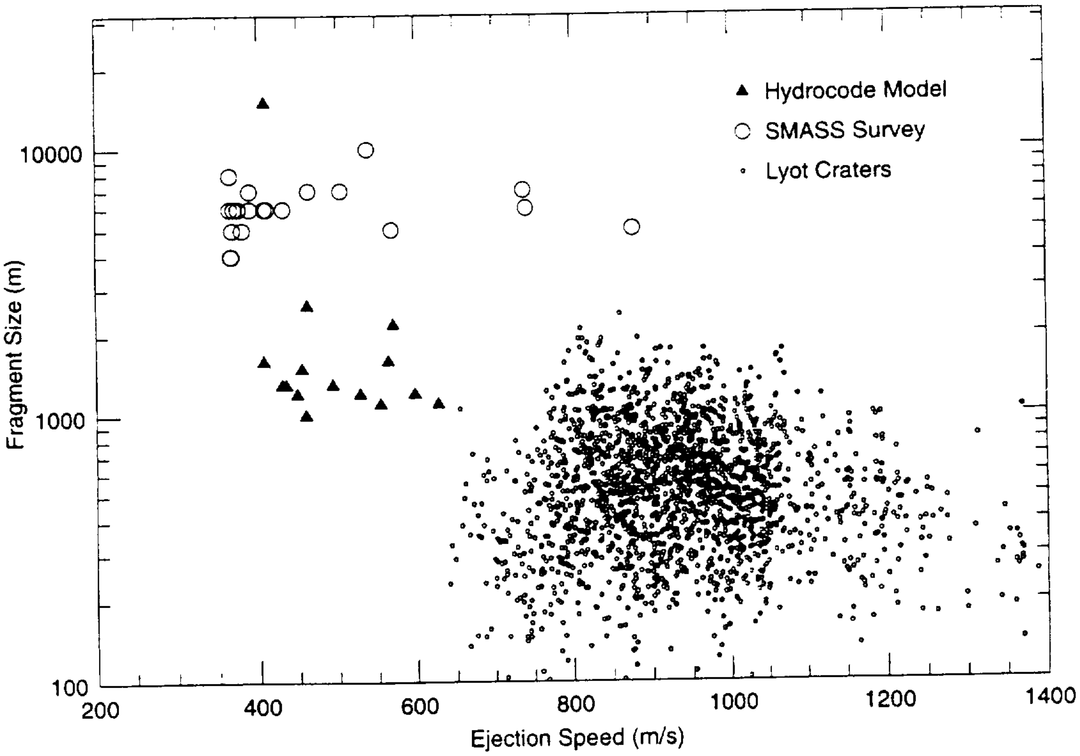

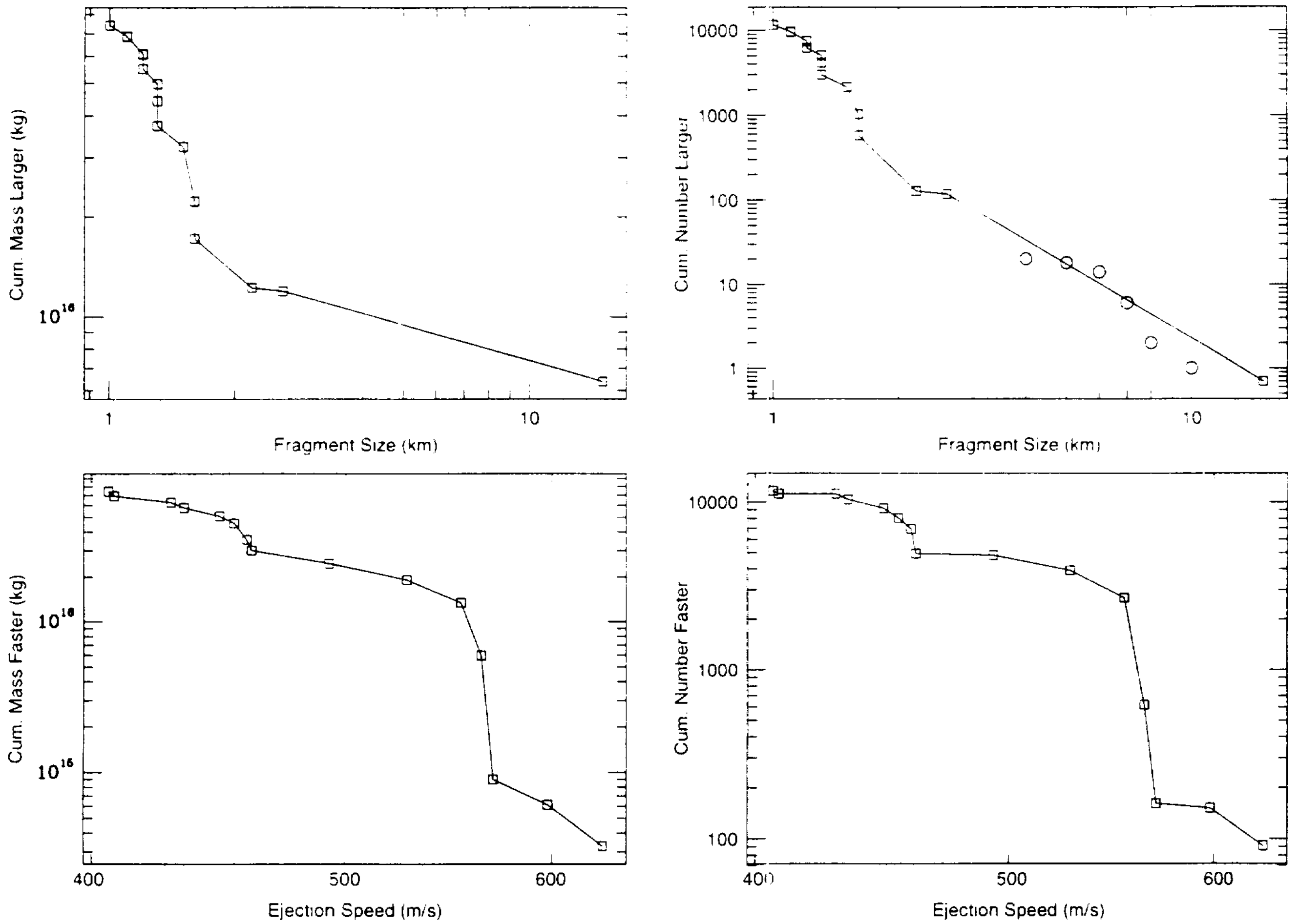

FIG. 9. Size-velocity-mass distributions for the *escaping* fraction of ejecta resulting from the high-resolution layered Vesta impact. The plots are self-explanatory. The cumulative size frequency distribution slope (top right) is −4, which is somewhat steeper than expected from catastrophic disruption events; size distribution data for the Vesta family asteroids is superposed for comparison. Most of the ejected mass is at the lower speeds and the smaller sizes, as expected.

or more comparatively recent and minor impacts at Vesta each ejected all three kinds of material at speeds sufficient to reach Earth directly. The first scenario may be the most economical explanation based on current evidence, and the second also has good merit. Higher resolution models at nonzero incidence would probably enhance fragment sizes and speeds in impact models; therefore, even though the simulation presented here did not yield fragments of the speed presumably required to produce a kilometer-sized Earth-approacher, the proximity of asteroid 1980 PA (Cruikshank *et al.*, 1991) and its exceptional radar roughness (Ostro *et al.*, 1991) makes this V-type asteroid a leading candidate for further observation.

One possible implication of these numerical models is that asteroids swap material with relative ease. If Vesta rocks arrive at Earth in abundance, then we might infer that rocks from smaller asteroids are ejected to even greater distances in even greater numbers. A "greying" of the solar system seems not to have taken place, however, and to avoid an embarassment of riches, we should notice that the monolayered Vesta model (Fig. 2a) failed to yield copious, large fast ejecta. Porous targets (Love *et al.*, 1993; Asphaug *et al.*, 1996b) likewise exhibit dramatically lowered ejection efficiency. It may be that Vesta, a stratified rock with distinct layers, is better suited than most other asteroids to sending material across the solar system.

Acknowledgements–I thank Donald Davis, Paolo Farinella and Kevin Zahnle for their detailed comments and valuable critiques; Anne Vickery for providing secondary crater data for Lyot; and Jay Melosh for getting the ball rolling several years ago. Funding and computational support were provided by NASA's Planetary Geology and Geophysics Program: "Geophysics of Small Planetary Bodies" and "Numerical Simulations of Impacts and Collisions."

Editorial handling: R. P. Binzel

REFERENCES

AHRENS T. J. AND RUBIN A. M. (1993) Impact-induced tensional failure in rock. *J. Geophys. Res.* **98**, 1185–1203.

AMSDEN A. A., RUPPEL H. M. AND HIRT C. W. (1980) *SALE: A Simplified ALE Computer Program for Fluid Flow at All Speeds.* LA-8095, Los Alamos National Laboratory, New Mexico.

ASPHAUG E. (1994) Large ejecta fragments from asteroids (abstract). *Meteoritics* 29, 440–441.

ASPHAUG E. AND BENZ W. (1994) The surface and interior of Phobos (abstract). *Lunar Planet. Sci.* **25**, 43–44.

ASPHAUG E. AND MELOSH H. J. (1993) The Stickney impact of Phobos: A dynamical model. *Icarus* **101**, 144–164.

ASPHAUG E., MELOSH H. J. AND VICKERY A. (1993) High-velocity ejection of large fragments from asteroids in non-catastrophic impact events: Results for Vesta. In *IAU Symposium* **160**: *Asteroids Comets, Meteors* (eds. A. Milani, M. Di Martino and A. Cellino). Kluwer, Dordrecht, The Netherlands.

ASPHAUG E., MOORE J. M., MORRISON D., BENZ W., NOLAN M. C. AND SULLIVAN R. J. (1996a) Mechanical and geological effects of impact cratering on Ida. *Icarus* **120**, 158–184.

Asphaug E., Benz W., Ostro S. J., Scheeres D. J., De Jong E. M., Suzuki S. and Hudson R. S. (1996b) Disruptive impacts into small asteroids. *Bull. Am. Astron. Soc.*, DPS Meeting #28, 10.31.

Bell J. F., Owensby P. D., Hawke B. R. and Gaffey M. J. (1988) The 52-color asteroid survey: Final results and interpretation (abstract). *Lunar Planet. Sci.* **19**, 57-58.

Bell J. F., Davis D. R., Hartmann W. K. and Gaffey M. J. (1989) Asteroids: The big picture. In *Asteroids II* (eds. R. P. Binzel, T. Gehrels and M. S. Matthews), pp. 921–945. University of Arizona Press, Tucson, Arizona.

Belton M.J.S., Mueller B. E. A., D'Amario L. A., Byrnes D. V., Klaasen K. P., Synnott S., Breneman H. T., Johnson T. V., Thomas P.C., Veverka J., Harch A. P., Davies M. E., Merline W. J., Chapman C. R., Davis D. R., Denk T., Neukum G., Petit J-M., Greenberg R., Storrs A. and Zellner B. (1996) The discovery and orbit of 1993 (243)1 Dactyl. *Icarus* **120**, 185–199.

Benz W. and Asphaug E. (1994) Impact simulations with fracture. I. Methods and tests. *Icarus* **107**, 98–116.

Benz W. and Asphaug E. (1995) Simulations of brittle solids using smooth particle hydrodynamics. *Comput. Phys. Comm.* **87**, 253–265.

Binney J. and Tremaine S. (1987) *Galactic Dynamics.* Princeton Univ. Press, Princeton, New Jersey. 773 pp.

Binzel R. P. and Xu S. (1993) Chips off of asteroid 4 Vesta: Evidence for the parent body of basaltic achondrite meteorites. *Science* **260**, 186–191.

Burbine T. H., Meibom A. and Binzel R. P. (1996) Mantle material in the main belt: Battered to bits? *Meteorit. Planet. Sci.* **31**, 607–620.

Cellino A., Zappalà V., DiMartino M., Farinella P. and Paolicchi P. (1987) Flattening, pole, and albedo features of 4 Vesta from photometric data. *Icarus* **70**, 546–565.

Chapman C. R. (1986) Implications of the inferred compositions of the asteroids for their collisional evolution. *Mem. Soc. Astron. Italiana* **57**, 103–114.

Chapman C. R., Paolicchi P., Zappalà V., Binzel R. P. and Bell J. F. (1989) Asteroid families: Physical properties and evolution. In *Asteroids II* (eds. R. P. Binzel, T. Gehrels and M. S. Matthews), pp. 386–415. University of Arizona Press, Tucson, Arizona.

Consolmagno G. J. and Drake M. J. (1977) Composition and evolution of the eucrite parent body: Evidence from rare earth elements. *Geochim. Cosmochim. Acta* **41**, 1271–1282.

Cruikshank D. P., Tholen D. J., Hartmann W. K., Bell J. F. and Brown R. H. (1991) Three basaltic Earth-approaching asteroids and the source of the basaltic meteorites. *Icarus* **89**, 1–13.

Davis D. R., Chapman C. R., Greenberg R. and Weidenschilling S. J. (1985) Collisional history of asteroids: Evidence from Vesta and the Hirayama families. *Icarus* **62**, 30–53.

Davis D. R., Ryan E. V. and Farinella P. (1994) Asteroid collisional evolution: Results from current scaling algorithms. *Planet. Space Sci.* **42**, 599–610.

Drake M. J. (1979) Geochemical evolution of the eucrite parent body: Possible nature and evolution of asteroid 4 Vesta? In *Asteroids* (ed. T. Gehrels), pp. 765–782. Univ. Arizona Press, Tucson, Arizona.

Drummond J. D., Eckart A. and Hege E. K. (1988) Speckle interferometry of asteroids IV: Reconstructed images of 4 Vesta. *Icarus* **73**, 1–14.

Dumas C. and Hainaut O. R. (1996) Mapping Vesta in the visible and near-infrared: The 1994 and 1996 oppositions as viewed from the ground. In *Workshop on Evolution of Igneous Asteroids.* Lunar and Planetary Institute, Houston, Texas.

Farinella P. and Davis D. R. (1992) Collision rates and impact velocities in the main asteroid belt. *Icarus* **97**, 111–123.

Fujiwara A., Cerroni P., Davis D. R., Ryan E. and DiMartino M. (1989) Experiments and scaling laws for catastrophic collisions. In *Asteroids II* (eds. R. P. Binzel, T. Gehrels and M. S. Matthews), pp. 240–265. University of Arizona Press, Tucson, Arizona.

Gaffey M. J. (1983) The asteroid 4 Vesta: Rotational spectral variations, surface material heterogeneity, and implications for the origins of basaltic achondrites (abstract). *Lunar Planet. Sci.* **14**, 231–232.

Gaffey M. J. (1993) Forging an asteroid-meteorite link. *Science* **260**, 167–168.

Gaffey M. J. (1997) Surface lithologic heterogeneity of asteroid 4 Vesta. *Icarus* **127**, 130–157.

Gaffey M. J. and McCord T. B. (1978) Asteroid surface materials: Mineralogical characterizations from reflectance spectra. *Space Sci. Rev.* **21**, 555–628.

Gaffey M. J., Bell J. F., Brown R. H., Burbine T. H., Piatek J. L., Reed K. L. and Chaky D. A. (1993) Mineralogical variations within the S-type asteroid class. *Icarus* **106**, 573–602.

Gault D. E. and Wedekind J. A. (1969) The production of tektites by meteoroid impact. *J. Geophys. Res.* **74**, 6780–6794.

Grady M. M. (1995) Parental paradoxes. *Nature* **378**, 18–19.

Grady D. E. and Kipp M. E. (1980) Continuum modeling of explosive fracture in oil shale (abstract). *Int. J. Rock Mech. Min. Sci. Geomech.* **17**, 147–157.

Graham A. L., Bevan A. W. R. and Hutchison R. (1985) *Catalogue of Meteorites*, 4th ed., University of Arizona Press, Tucson, Arizona.

Hewins R. H. and Newsom H. E. (1988) Igneous activities in the early solar system. In *Meteorites and the Early Solar System* (eds. J. F. Kerridge and M. S. Matthews), pp. 73–101. Univ. Arizona Press, Tucson, Arizona.

Heymann D., Mazor E. and Anders E. (1969) Ages of the CA-rich achondrites. In *Meteorite Research* (ed. P.M. Millman), pp. 444–457. Reidel, Dordrecht, The Netherlands.

Housen K. R., Schmidt R. M. and Holsapple K. A. (1983) Crater ejecta scaling laws: Fundamental forms based on dimensional analysis. *J. Geophys. Res.* **88**, 2485–2499.

Keil K., Haack H. and Scott E. R. D. (1994) Catastrophic fragmentation of asteroids: Evidence from meteorites. *Planet. Space Sci.* **42**, 1109–1122.

Lange M. A. and Ahrens T. J. (1983) The Dynamic Tensile Strength of Ice and Ice-Silicate Mixtures. *J. Geophys. Res.* **88**, 1197–1208.

Lawn B. R. and Wilshaw T. R. (1975) *Fracture of Brittle Solids.* Cambridge University Press, Cambridge, U.K.

Love S. G. and Ahrens T. J. (1996) Catastrophic impacts on gravity dominated asteroids. *Icarus* **124**, 141–155.

Love S. G., Hörz F. and Brownlee D. E. (1993) Target porosity effects in impact cratering and collisional disruption. *Icarus* **105**, 216–224.

Mandell D. A. and Wingate C. A. (1994) Prediction of material strength and fracture of glass using the SPHINX smooth particle hydrodynamics code. LANL Report *LA-12830.*

Martelli G., Rothwell P., Giblin I., DiMartino M. and Farinella P. (1993) Fragment jets from catastrophic break-up events and the formation of asteroid binaries and families. *Astron. Astrophys.* **271**, 315–318.

Marzari F., Cellino A., Davis D. R., Farinella P., Zappalà V. and Vanzani V. (1996) Origin and evolution of the Vesta asteroid family. *Astron. Astrophys.* **316**, 248–262.

McCarthy D. W., Jr., Freeman J. D. and Drummond J. D. (1994) High resolution images of Vesta at 1.65 *μ*m. *Icarus* **108**, 285–297.

Melosh H. J. (1984) Impact ejection, spallation, and the origin of meteorites. *Icarus* **59**, 234–260.

Melosh H. J. (1987) High-velocity solid ejecta fragments from hypervelocity impacts. *Int. J. Impact Engineering* **5**, 483–492.

Melosh H. J. (1989) *Impact Cratering: A Geologic Process.* Oxford Univ. Press, New York, New York. 245 pp.

Melosh H. J., Ryan E. V. and Asphaug E. (1992) Dynamic fragmentation in impacts: Hydrocode simulation of laboratory impacts. *J. Geophys. Res.* **97**, 14 735–14 759.

Mitchell D. L., Ostro S. J., Hudson R. S., Rosema K. D., Campbell D. B., Vélez R., Chandler J. F., Shapiro I., Giorgini J. D. and Yeomans D. K. (1996) Radar observations of asteroids 1 Ceres, 2 Pallas, and 4 Vesta. *Icarus* **124**, 113–133.

Nakamura A. and Fujiwara A. (1991) Velocity distribution of fragments formed in a simulated collisional disruption. *Icarus* **92**, 132–146.

Nolan M. C., Asphaug E., Melosh H. J. and Greenberg R. (1996) Impact craters on asteroids: Does gravity or strenth control their size? *Icarus* **124**, 359–371.

Ostro S. J., Campbell D. B., Chandler J. F., Shapiro I. I., Hine A. A., Velez R., Jurgens R. F., Rosema K. D., Winkler R. and Yeomans D. K. (1991) Asteroid radar astrometry. *Astron. J.* **102**, 1490–1502.

Ryan E. V. C. and Melosh H. J. (1995) Asteroids: Shattered but not dispersed. EOS **76** (46), F336.

Schultz P. H., Gault D. E. and Crawford D. (1986) Impacts of hemispherical granular targets: Implications for global impacts (abstracts). *Lunar Planet. Sci.* **17**, 783–784.

Sears D. W. G. and Dodd R. T. (1988) Overview and classification of meteorites. In *Meteorites and the Early Solar System* (eds. J. F. Kerridge and M. S. Matthews), pp. 3–34. University of Arizona Press, Tucson, Arizona.

Standish E. M. and Hellings R. W. (1989) A determination of the masses of Ceres, Pallas and Vesta from their perturbations upon the orbit of Mars. *Icarus* **80**, 326–333.

Stöffler D., Bischoff A., Buchwald V. and Rubin A. E. (1988) Shock effects in meteorites. In *Meteorites and the Early Solar System* (eds. J. F. Kerridge and M. S. Matthews), pp. 165–202. University of Arizona Press, Tucson, Arizona.

Tholen D. J. (1984) Asteroid taxonomy from cluster analysis of photometry. Ph.D. Dissertation, Univ. Arizona, Tucson, Arizona.

THOMAS P. C., BINZEL R. P., GAFFEY M. J., STORRS A. D., WELLS E. N. AND ZELLNER B. H. (1997) Impact excavation on asteroid 4 Vesta: Hubble Space Telescope results. *Science* **277**, 1492–1495.

TILLOTSON J. H. (1962) Metallic equations of state for hypervelocity impact. *General Atomic Report* GA-3216.

VICKERY A. (1986) Size-velocity distribution of large ejecta fragments. *Icarus* **67**, 224–236.

VICKERY A. (1987) Variation in ejecta size with ejecta velocity. *Geophys. Res. Lett.* **14**, 726–727.

WASSON J. T. AND WETHERILL G. W. (1979) Dynamical, chemical and isotopic evidence regarding the formation locations of asteroids and meteorites. In *Asteroids* (ed. T. Gehrels), pp. 926–974. Univ. Arizona Press, Tucson, Arizona.

WEIBULL W. A. (1939) A statistical theory of the strength of materials (in Swedish). *Ingvetensk. Akad. Handl.* **151**. 5–45.

WELTEN K. C., LINDNER L., VAN DER BORG K., LOEKEN TH., SCHERER P. AND SCHULTZ L. (1993) Cosmogenic ^{10}Be and noble gases in diogenites (abstract). *Meteoritics* **28**. 459.

WELTEN K. C., LINDNER L., VAN DER BORG K., LOEKEN TH., SCHERER P. AND SCHULTZ L. (1996) Cosmic-ray exposure ages of diogenites and the collisional history of the HED parent body or bodies. In *Workshop on Evolution of Igneous Asteroids*. Lunar and Planetary Institute, Houston, Texas.

WETHERILL G. W. (1985) Asteroidal source of ordinary chondrites. *Meteoritics* **20**, 1–22.

WETHERILL G. W. (1987) Dynamical relationship between asteroids, meteorites, and Apollo-Amor objects. *Phil. Trans. Roy. Soc. London* **A323**, 323–337.

WISDOM J. (1983) Chaotic behavior and the origin of the 3/1 Kirkwood Gap. *Icarus* **56**, 51–74.

XU S., BINZEL R. P., BURBINE T. H. AND BUS S. J. (1995) Small main-belt asteroid spectroscopic survey: Initial results. *Icarus* **115**, 1–35.

ZAPPALÀ V., BENDJOYA PH., CELLINO A., FARINELLA P. AND FROESCHLÉ C. (1995) Asteroid families: Search of a 12,487-asteroid sample using two different clustering techniques. *Icarus* **116**, 291–314.

ZELLNER B., THOLEN D. J. AND TEDESCO E. F. (1985) The eight-color asteroid survey: Results for 589 minor planets. *Icarus* **61**, 355–416.

ZELLNER B. H., ALBRECHT R., BINZEL R. P., GAFFEY M. J., THOMAS P. C., STORRS A. D. AND WELLS E. N. (1997) Hubble Space Telescope images of Asteroid 4 Vesta in 1994. *Icarus* **128**, 87–88.

ICARUS 124, 359–371 (1996)
ARTICLE NO. 0214

Impact Craters on Asteroids: Does Gravity or Strength Control Their Size?

MICHAEL C. NOLAN[1]

Lunar and Planetary Laboratory, University of Arizona, Tucson, Arizona 85721
E-mail: nolan@naic.edu

ERIK ASPHAUG

NASA Ames Research Center MS 245-3, Moffett Field, California 94035

H. JAY MELOSH

Lunar and Planetary Laboratory, University of Arizona, Tucson, Arizona 85721

AND

RICHARD GREENBERG

Lunar and Planetary Laboratory, University of Arizona, Tucson, Arizona 85721

Received March 10, 1995; revised April 9, 1996

The formation of kilometer-size craters on asteroids is qualitatively different from the formation of meter-size (laboratory- and weapons-scale) craters on Earth. A numerical hydrocode model is used to examine the outcomes of various-size cratering impacts into spheres and half-spaces. A shock wave fractures the target in advance of the crater excavation flow; thus, for impactors larger than 100 m, impacting at typical asteroid impact velocities, target tensile strength is irrelevant to the impact outcome. This result holds whether the target is initially intact or a "rubble pile," even ignoring the effects of gravity. Because of the shock-induced fracture, crater excavation is controlled by gravity at smaller sizes than would otherwise be predicted. Determining the strength–gravity transition by comparing the physical strength of the material to the force of gravity will not work, because strength is eliminated by the shock wave.

A key property that describes the outcomes of impacts is the strength of the targets under various conditions, but "strength" has several different meanings in this context. All involve a quantity with the units of force per unit area (pressure), or, equivalently, energy per unit volume (Housen *et al.* 1983). Here we define "physical strength" as static tensile strength against brittle failure. Tensile strength is usually assumed to be the most appropriate material parameter for models used to extrapolate experimental collision outcomes to asteroidal dimensions, for example, by Housen *et al.* (1991), because the critical failure is assumed to be tensile. In this paper, we show that physical strength is almost always unimportant in events that form large craters, because the shock wave generated by the impact fractures material before the crater excavation flow begins.

This discovery shows that the widely adopted "strength scaling" used to extrapolate from laboratory experiments has (until recently) been applied inappropriately.

1. SCALING LAWS

In a sequence of papers, K. Housen, R. Schmidt, and K. Holsapple developed a widely used set of scaling laws to the outcomes of large impacts from terrestrial experiments (Holsapple and Housen 1986, Holsapple and Schmidt 1980, 1982, 1987, Housen and Holsapple 1990, Housen *et al.* 1983, 1991). These scaling laws are based on a dimensional analysis of the problem, combined with fits to experimental data.

Dimensional analysis relies on the construction of dimensionless combinations of parameters describing the ini-

---

[1] Current address: Arecibo Observatory, PO Box 995, Arecibo PR 00613 USA.

0019-1035/96 $18.00

tial and final states of the impact. Ambiguity arises if more than one dimensionless combination can be constructed. Such ambiguity arises if, for example, there are more than one more parameter (*e.g.*, density, size, strength, and impact velocity) than there are dimensions that relate them (*e.g.*, length, time, and mass). Note that there is no ambiguity in the *outcome*, but there is no way to find specific functional forms using *only* dimensional analysis. To alleviate this problem and allow unique solutions, they assume that there are separate regimes where different target parameters (*e.g.*, strength or gravity) dominate the outcome, so that other parameters may be ignored. They also assume that there are two different phases of an impact: an "early-time" phase, where momentum and energy are coupled into the target, and a "late-time" phase, where the details of that coupling are unimportant and can be combined into a single "coupling parameter" *C*. These assumptions are required to reduce the number of variables so that unique power-law scaling relations can be constructed. In most cases, experiments show power-law behavior, indicating that the assumptions hold in the regimes in which they have been tested.

Scaling laws do allow interpolation and limited extrapolation of experimental results. Longer extrapolation is possible (bearing in mind the uncertainties of the fits), but runs the risk of missing a change in the dominant physics. For example, velocity dependence probably cannot be extrapolated across the speed of sound. As another example, for the largest targets, gravity likely is the only relevant force, whereas in the laboratory, it is usually irrelevant. Thus, when it applies, gravity scaling should give accurate results, but it is difficult to determine when it applies from laboratory experiments. Once the relevant physical regimes have been identified, scaling, by its nature, works well within those regimes.

There is, however, no well-founded a priori way to know at what size gravity dominates, without either understanding the change in physics or performing experiments with different gravity conditions and using dimensional analysis to determine the dependence (Chapman and McKinnon 1986, Schmidt and Holsapple 1980). In the strength-scaling limit, the primary resistance to the flow of ejecta is due to the poorly defined "strength" of the rock. On the Earth, this regime is thought to apply to the formation of craters up to a few tens of meters in diameter (Melosh 1989). For larger craters, the primary resistance is due to gravity: excavation stops when insufficient energy remains to lift the overlying material against the force of its weight. On asteroids, the force of gravity is much smaller than on Earth, so strength was considered likely to dominate. However, the material may also be very weak. Thus the dominant process is uncertain. Empirical scaling laws derived *for terrestrial conditions* do not directly apply.

2. NUMERICAL MODELING OF IMPACTS

We attack this problem using a numerical hydrocode [SALE (Amsden *et al.* 1980)] modified by H. J. Melosh and E. Asphaug to include the fracture algorithm of Grady and Kipp (1987) (Asphaug 1993, Asphaug and Melosh 1990, 1993, Asphaug *et al.* 1996, Melosh *et al.* 1992). This program simulates the small-scale physics of fracture, shock, and gravity, allowing the ejecta to form under the relevant physical conditions. The numerical procedure has the advantage over scaling relationships that it operates locally, at relatively small scale, using the physical properties of materials rather than phenomenological parameters extrapolated to large scale. The large-scale results are determined as a consequence of the cumulative small-scale processes.

Melosh *et al.* (1992), Asphaug (1993), and Ryan (1992) confirmed that the results of this numerical hydrocode model match the outcomes of laboratory experiments. Asphaug and Melosh (1993) used this program to simulate the impact that created the crater Stickney on Phobos. That result contradicted the results of strength-scaling models, which predicted that an impact large enough to create Stickney would destroy the satellite.

The hydrocode model has some disadvantages compared with analytic scaling theory. The large-scale results depend strongly on the correct representation of the small-scale fragmentation. Also, as in any numerical model, each case of interest must be modeled separately, until enough cases have been studied to show how the results depend on the various model parameters individually. In this way, this modeling complements analytical scaling by (1) making a different set of assumptions and (2) allowing the visualization of impacts at scales unattainable in the laboratory, so that we can examine the physical processes that operate at those scales. The correct prediction of laboratory impact outcomes, together with comparisons to weapons data, suggests that the measurement accuracy of the fracture parameters (and the model itself) is sufficient for the materials studied.

The results reported here use the two-dimensional version of the hydrocode, with the targets modeled as axially symmetric solids. With this version, we were able to perform a large number of model runs much more quickly than with a three-dimensional model. The shape can be an arbitrary solid of revolution, although the actual grid is rectangular, so that large asymmetries can result in numerical instabilities.

The Grady and Kipp (1987) fracture model assumes that materials have a preexisting distribution of flaws, and that brittle fracture occurs by failure of these flaws under tensile stress. This distribution of flaws is modeled as two material parameters, determined by experiment. As implemented in the hydrocode (Asphaug 1993, Melosh *et al.* 1992), these flaws change the bulk material properties through a parameter D called "damage." This parameter varies from 0 to 1 to describe degree of fragmentation of the material as fracture proceeds. When $D = 0$, the material behaves as a Hooke elastic solid; as D increases, the elastic moduli are reduced by a factor of $1 - D$ for tensile and shear stresses. Thus, when $D = 1$, the material has been fragmented so that it has zero tensile strength and behaves as a liquid, resisting only compressional forces.

The Grady–Kipp model is both size and rate dependent. Large targets have a greater likelihood of containing flaws of a given weakness and, therefore, have a lower overall failure threshold. Similarly, at modest loading rates only the few weakest flaws are activated by the stress pulse, resulting in a lower peak stress of failure. Hence rocks become effectively stronger when loaded at high strain rates (Asphaug 1993, Melosh *et al.* 1992). The size-dependent strength becomes a global initial condition in our method, scaling approximately with the inverse cube root of the size for the parameters we are using. The rate-dependent strength scales approximately linearly with the loading rate. Such behavior is well known in rocks (Rinehart 1965, Weibull 1939); it is in fact the rate-dependent strength measurements in the laboratory that constrain the flaw distribution coefficients.

Because flaws are entirely statistical entities in our method, failure is exaggerated along the symmetry axis where there are a greater number of cells per unit spatial volume. This amounts to an exaggerated number of flaw nucleation sites near the axis. Benz and Asphaug (1994a, 1994b) get around this problem by making the flaw distribution purely explicit, with flaws distributed randomly, in proportion to the cell volume. Their method foregoes the Grady–Kipp fragment size and damage statistics. In regions of sparse damage, the difference between the two models is important; but where damage is total, such as the interior of a crater bowl, the statistical and explicit methods agree. Because the size-dependent strength is global in our treatment and local in the explicit method of Benz and Asphaug, the fracture constants that best fit the data can differ between the two methods. Here we have used those constants that produced the best agreement with laboratory data for tests using the same code (Melosh *et al.* 1992).

3. LARGE- AND SMALL-SCALE IMPACTS

The targets in these simulations are 12.6-km-diameter basalt spheres (the same volume as asteroid 951 Gaspra), and infinite half-spaces. Note that gravity is purposely not applied in any of these simulations. They address only the effects of *fracture* in various situations. Any departure from strength scaling in these smulations is not due to the influence of gravity. For sufficiently large targets (*e.g.*, the Earth and the very largest asteroids), gravitational self-compression inhibits fracture by increasing the total pressure, but that effect is negligible in these simulations, where the maximum lithostatic pressure is smaller than the tensile strength of the weakest flaw.

3.1. *Large Cratering Event*

First, we consider the impact of a 123-m-diameter basalt ($\rho = 2700$ kg m^{-3}) body hitting the 12.6-km-diameter target at 5.3 km sec^{-1}. Figures 1–3 show a time sequence of this impact in the model target. The left half shows the model grid, and the right shows the velocities at each of the grid nodes, all initially zero, except for the actual impactor. The grid is a solid of rotation about a vertical axis at the center of the diagram. Thus, in this case, it is a sphere. In some of the models, the projectile is formed by extending the grid upward, so that the earliest deformation makes the grid more rather than less regular, increasing the code stability. For moderate-velocity impacts with relatively small projectiles (like the one-node projectile here), that turned out to be unnecessary. Table I shows the material properties used in all of the simulations presented here. We use the Tillotson equation of state for low-pressure anorthosite, as described in Melosh (1989, pp. 233–234), substituting the bulk modulus κ for the Tillotson A and B parameters. Figure 1 shows the situation 0.234 sec after the initial contact. On the right, note that the velocity field is essentially radial, away from the point of impact. The contour plot on the left shows the "damage" parameter D used in the fragmentation model. At the early stage shown in Fig. 1, both the shock wave due to the (marginally) supersonic impact and the strain of crater flow are fracturing the material, increasing D in the fracturing region. Figure 1 shows that undamaged material has substantial velocity (and divergence of velocity), so that cratering is occurring in undamaged rock. Material strength can affect the flow behavior at this stage.

Figure 2 shows a later stage in the process, 1.88 sec after initial contact. The damage front has proceeded about halfway down the body, and the velocity field begins to show the crater forming. Here, the damage front is due to the shock wave and to the following rarefaction wave. The region of ejecta flow has long since been left behind by the damage front. At about this time, the damage front spreads out, indicating that the shock wave is dissipating.

TABLE I

Material Properties Used in the Hydrocode Simulations

Uncompressed density	$\rho = 2700$ kg m^{-3}
Bulk modulus	$\kappa = 26.7$ GPa
Shear modulus	$\mu = 22.7$ GPa
Weibull flaw distribution	$N(\varepsilon) = 10^{33}\varepsilon^{9.5}$ m^{-3}

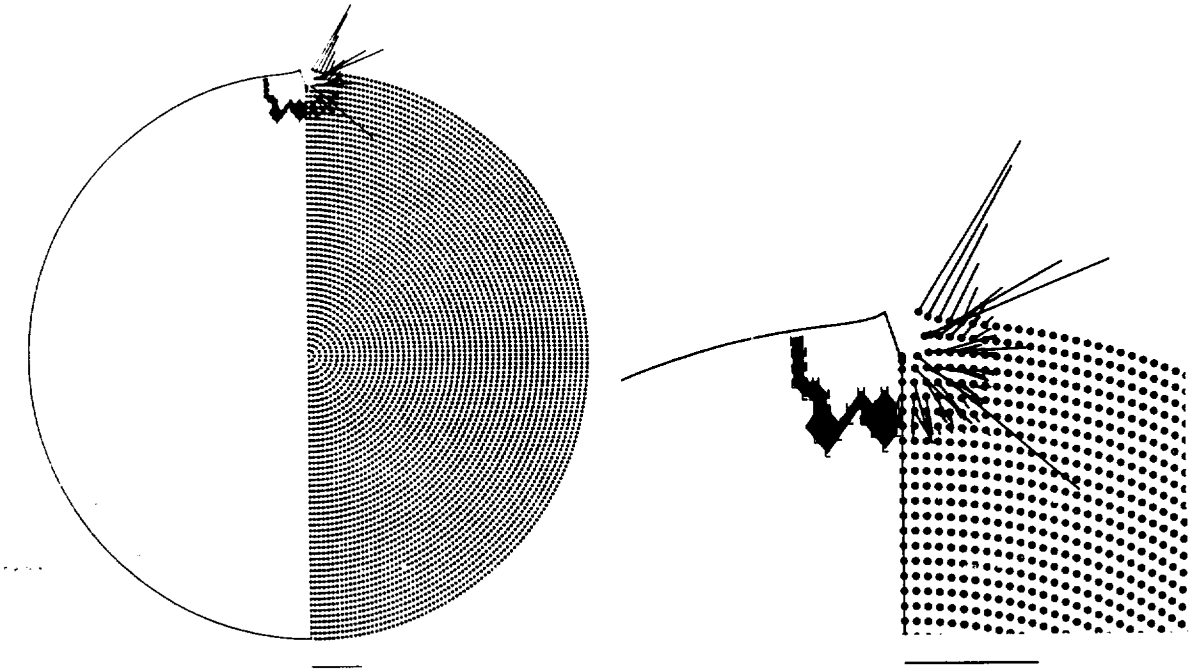

FIG. 1. Model 0.234 sec after the impact, showing the whole target and a blowup of the region near the impact site. The right half of each diagram shows the velocity field. The horizontal bars at the bottom are scale bars, here 200 m sec^{-1}. The left half is a contour map of damage, as discussed in the text. The contour values are from low (L) to high (H) 0.1, 0.2, 0.3, 0.4, 0.5, 0.6, 0.7, 0.8, 0.9. Note that the contour levels are very tightly clustered within one to two cell lengths, as the damage front is propagating with the rarefaction wave that follows the shock wave. The structure in the damage front is at least partly due to the finite grid resolution, which is coarse enough that any real structure would not be well represented.

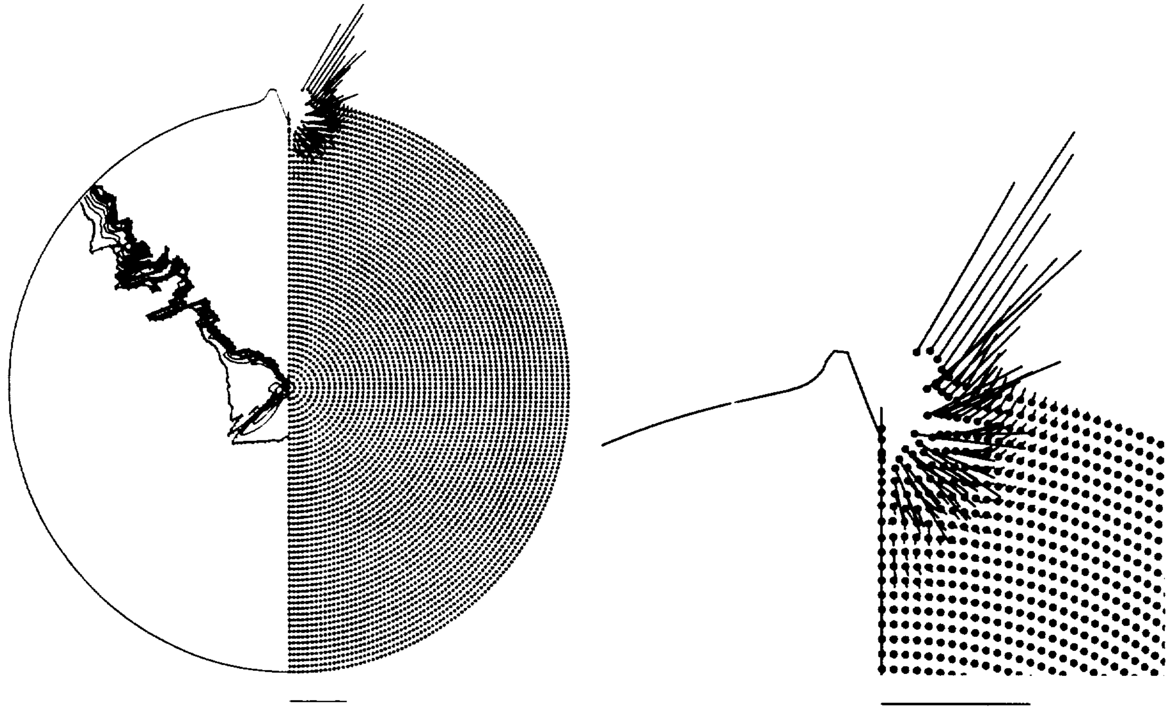

FIG. 2. Later in the run (1.88 sec), the parameters plotted as before. The scale bar is 200 m sec^{-1}. The right half is a blowup of the impact region. The damage has propagated much of the way through the body, and the region of increasing damage has grown to be about 10 cells wide. Note that the entire region in which crater flow is occurring, and will occur, has been completely damaged.

Figures 1 and 2 show fundamentally different fracture mechanisms in operation. In Fig. 1, cratering flow is accomplished through compressive deformation of solid unfractured rock. Later, as the cratering event proceeds (Fig. 2) cratering flow is in fragmented, strengthless rock. From the point of view of crater excavation, the rock only has physical strength for a very short time at the beginning of crater formation. For most of the crater formation, and certainly when the maximum crater extent is reached, the material is completely shattered and has little physical strength to resist flow. Friction may provide some strength, but it is orders of magnitude less than in the original unfractured material. We discuss this possibility further in Section 4.1.

Figure 3 shows the model after 240 sec. At this time, we are faced with one of the standard problems in cratering models: When does the cratering finish? Since there is no friction or gravity in the model, the ejecta flow will continue forever, though more and more slowly. It is possible to set upper limits on the final crater size, however. By this time, damage has long since ceased to increase. Since the ejecta velocities at this time are only a few meters per second and falling, they will not cause further expansion of the damaged region. Thus, an upper limit to the size of the crater is the extent of the damaged region when the damage stops increasing. In the case shown here, that limit is between 45° and 90° from the impactor. This problem is discussed further in Section 5.

3.2. *Small Cratering Event*

For comparison, Figs. 4 and 5 show an impact that forms a 1-cm crater in a half-space. The material is the same as in the previous simulations. Figure 4 shows the situation 3.77 μsec after impact. As in Fig. 1, the damage front is expanding with the shock wave. The flow velocities are approximately radial from the impact point. Figure 5 shows the event 60.4 μsec after the impact. Note that the crater flow is still keeping up with the damage front and that there are substantial velocities outside the damaged region.

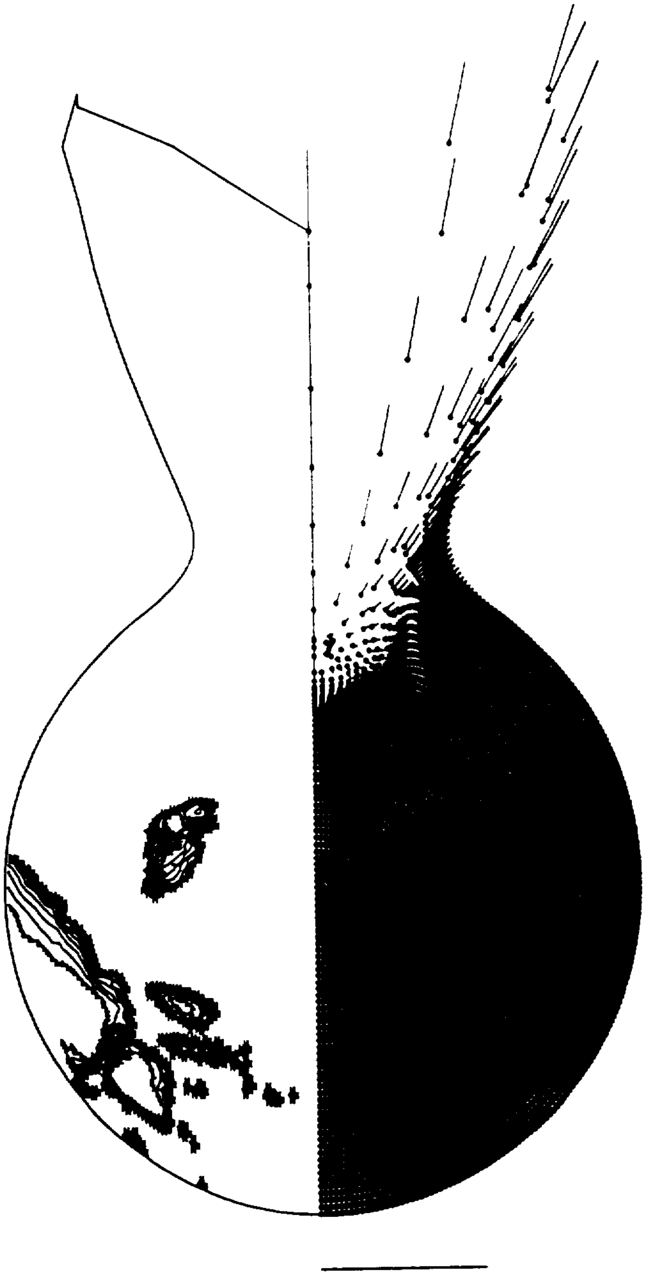

FIG. 3. Model 240 sec after the impact. The scale bar is 100 m sec^{-1}.

The crater bowl is at approximately the same position as the damage front (shown facing the velocity field), which is no longer advancing. The damage front is somewhat deeper in the center, partly due to the wave artificially reflected from the bottom and sides, but this feature appears to some extent even before the reflected shock returns. This effect is largely due to the fact that the computational cells all begin to fracture at the same stress, resulting in more flaws per unit volume near the axis where the cells are smaller due to the axial symmetry, as discussed in Section 2. This effect may also partly result from having all of the impact momentum emplaced on the axis. As the crater was evolving, material was being ejected right at the edge of the damage front, or more likely, the damage was done by the ejection flow which was proceeding through unfractured rock doing work against tensile strength.

The flow velocities in undamaged material show that elastic deformation and plastic deformation are doing work

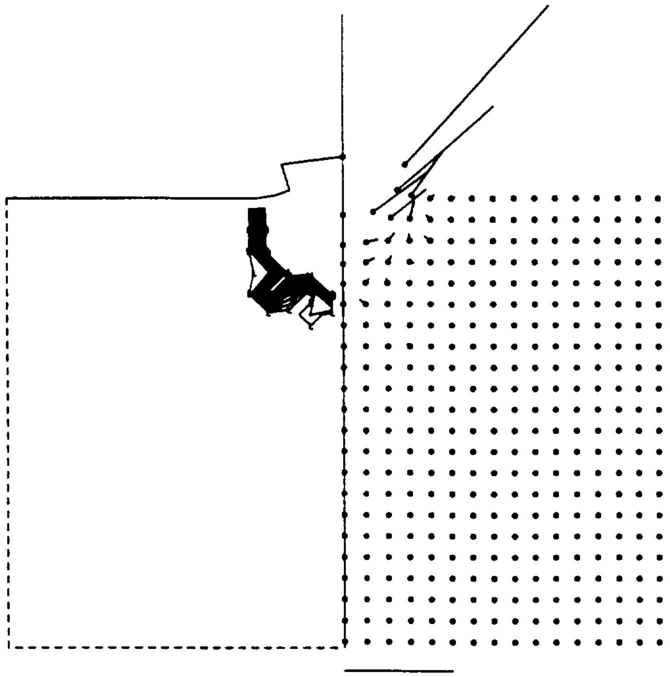

FIG. 4. Hydrocode simulation of an impact that forms a 1-cm crater in an infinite half-space, 3.77 μsec after the impact. The right half is the velocity field and the left half is a contour map of damage as in Fig. 1. The nodes are initially 1 mm apart, so that the region shown is 3.2 cm across. The actual numerical grid is twice the size of the region shown (in each direction). The scale bar is 200 m sec^{-1}. Note that the contour levels are very tightly clustered within one to two cell lengths, as the damage front is propagating with the rarefaction wave, which follows the shock wave.

against the strength of the material, so strength may be important in determining the final size of the crater. If so, the strength must be strain rate dependent to explain the faster-than-linear growth of the fractured region with impactor size (Holsapple and Schmidt 1987). In comparison, the flow in the large event of Section 3.1 is in material rubblized by the shock wave, so any initial tensile or shear strengths are irrelevant, and only compressive stresses can be transmitted.

A key qualitative difference can be recognized in Figs. 2 and 5 in the profile of velocities as a function of distance from the impact site. In Fig. 2, the flow velocities decrease gradually with distance from the impact. In contrast, in Fig. 5, the flow velocity decreases dramatically at the point where the flow field crosses the damage front. Clearly, the strength of the unfractured material is significantly affecting the crater flow for small impacts, but not for large ones.

3.3. Strengthless Targets

If the apparent differences in ejecta flow noted above are due to the loss of physical strength with size as we claim, then initially strengthless targets would give results very different from those above for the small impact and results very similar to those above for the large impact. We tested this hypothesis by running simulations identical to those shown above, except with damage D set to 1 when the run began, so that the target behaves as a strengthless liquid.

Large impacts. Figure 6 compares the final ejecta flow patterns for the run with (left) and without (right) initial tensile strength. The case on the left is the same as that described in Section 3.1, 15 sec after the impact. The crater

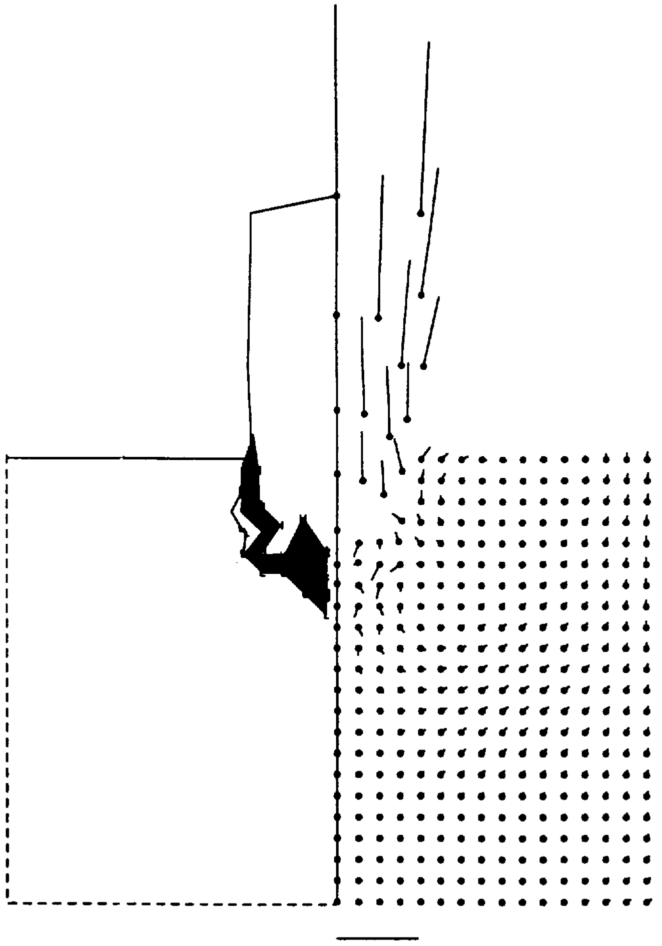

FIG. 5. Later in the run (121 μsec), the parameters plotted as in Fig. 1. The scale bar is 10 ms^{-1}. The damage has propagated as far as it ever will. Note that there are substantial crater flow velocities right up to the edge of the undamaged region.

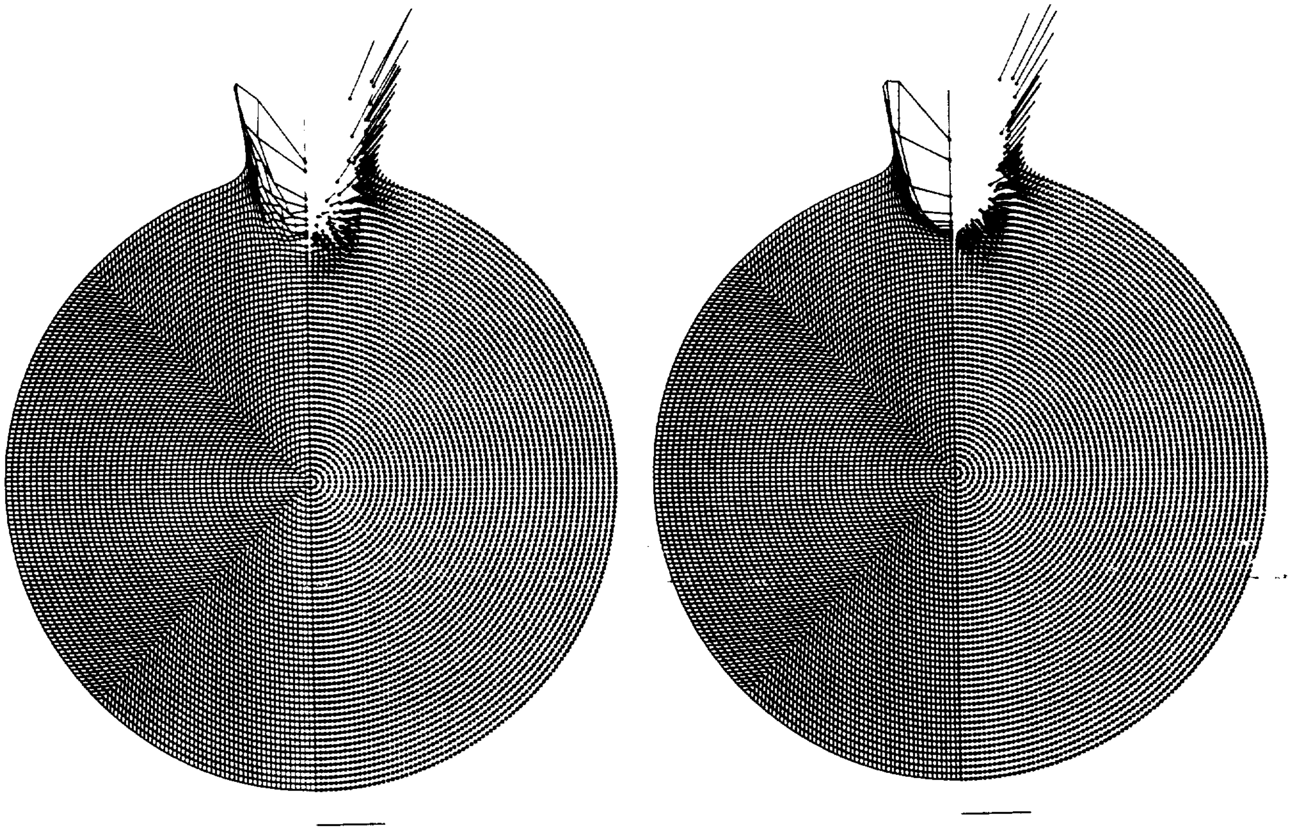

FIG. 6. Impacts of 123-m-diameter projectiles into strong (left) and strengthless (right) 12.6-km-diameter spherical targets at 5.3 km $\sec^{-1}$, 15 sec after impact. The velocity scale bar is 100 m $\sec^{-1}$ in both cases. The similarity indicates that physical strength is unimportant in an impact of this size.

sizes, the flow patterns, and the ejection velocities are quite similar in the two diagrams. There are some minor differences, apparently due to differences in the initial stages of the impact when the undamaged body retains tensile and shear strength (as shown in Fig. 1), and possibly to a difference in the effective depth of burial for the same reason. Nonetheless, these results demonstrate that physical strength is unimportant in an impact of this size, even though gravity was completely ignored in this calculation.

Small impacts. For comparison, Fig. 7 shows the same comparison for the small impact. On the left we see the strong target 60.4 μsec after impact, identical to Fig. 5, and on the right we see the result of the same impact into a strengthless target. On the left, we see high-velocity ejecta (tens to hundreds of meters per second) leaving the crater bowl almost vertically. The right-hand model in Fig. 7 shows the crater evolution in predamaged material. In this simulation, we see that the crater bowl is larger than in the unfractured case and that it is still expanding hemispherically: node velocities are radial from the impact, rather than vertically up out of the bowl. The maximum velocities are lower, but occur in a much larger volume of material.

This contrast can also be seen in Fig. 8, which shows the speed at each of the surface nodes, as a function of original distance from the impact site. The initially strong target yields speeds of tens of meters per second, but drops very quickly to near zero within 4 mm of the impact point. The strengthless target shows lower speeds, but ejecta flow continues out for several centimeters.

The crater in the initially strengthless target will continue to expand, slowing as more mass is accelerated. Eventually it will form a pattern similar to that of Fig. 6, with a crater much larger than shown for the unfractured target. Note that these two outcomes bear little resemblance to one another, and therefore physical strength is very important in impacts of this size.

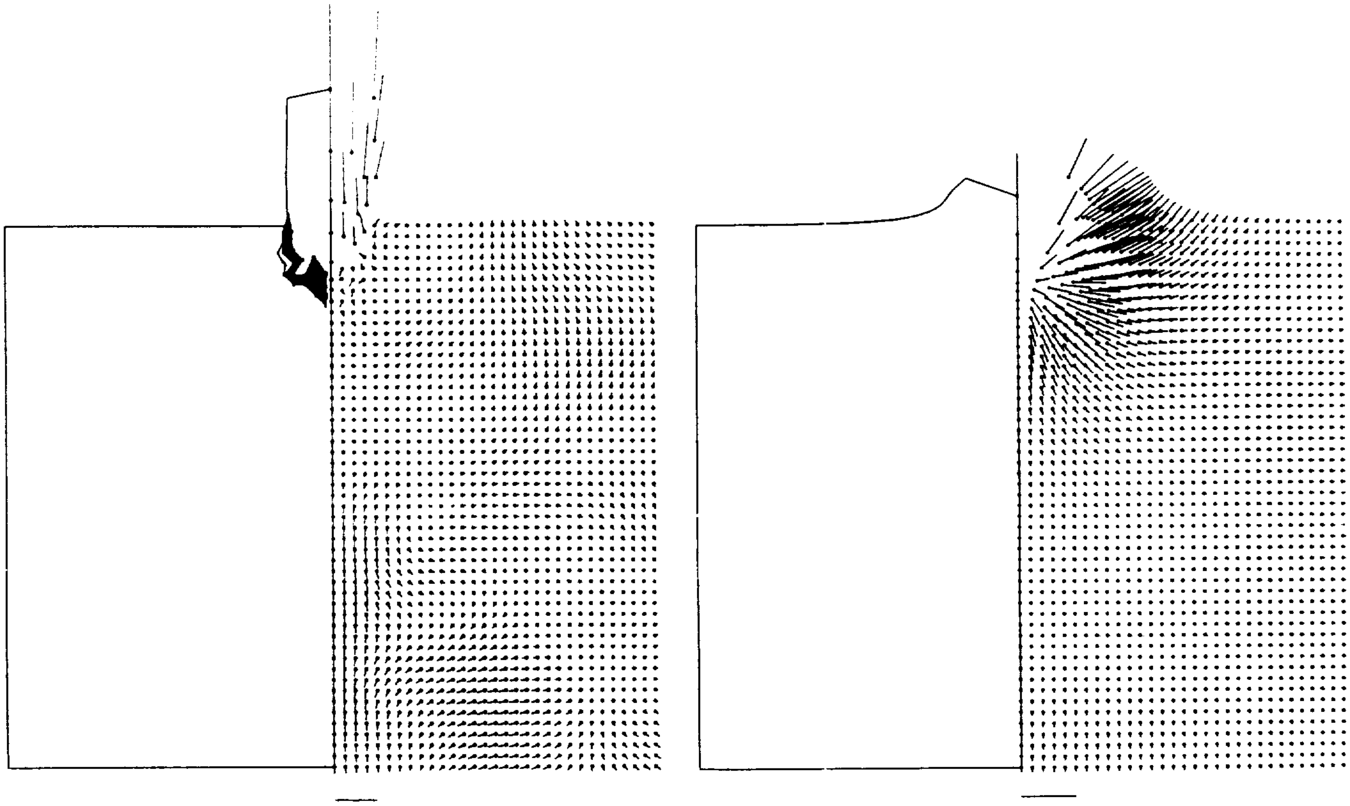

FIG. 7. Comparison of impacts of a 1-mm projectile into strong (left) and weak (right) semi-infinite targets at 5.3 km sec^{-1}, 60.4 μsec after impact. The velocity scale bar is 10 m sec^{-1} to show detail in both cases, so some velocity vectors are truncated. The peak velocities are >70 m sec^{-1}. Note that these two outcomes bear little resemblance to one another, and therefore physical strength is very important in impacts of this size.

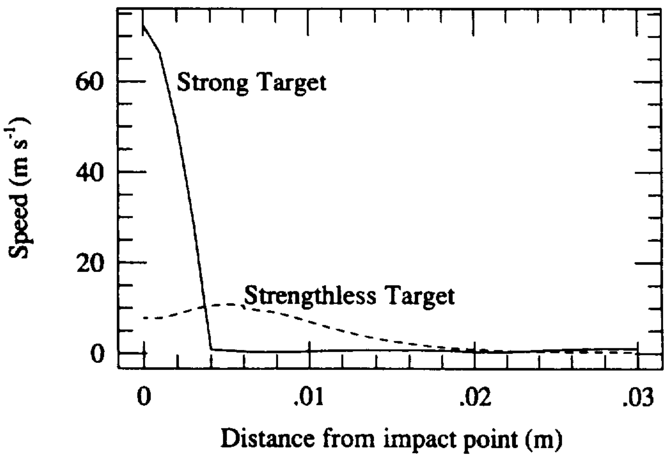

FIG. 8. Profiles of the speed at each surface node as a function of initial distance from impact point for the initially strong (solid) and strengthless (dashed) targets. The impact conditions are those of Fig. 4.

Thus these experiments have demonstrated our claim that physical strength is only important for small impacts, *even ignoring the effects of gravity*. In larger impacts, the shock wave due to the impact fractures the target so that it behaves as a strengthless material during the later cratering flow. Note, however, that the size of the fractured region may depend on the strength of the material, but it also depends on many other factors, such as the impact history of the target. These experiments also show that determining the strength–gravity transition by comparing the physical strength of the material (as measured in the laboratory) with the force of gravity will not work, because strength is eliminated by the shock wave.

Comparison of large and small impacts. These simulations show that the effects of physical strength are very different for large and small impacts. This difference is not due to the effect of gravity, which was ignored in all of the simulations shown above. Thus, in these simulations, we observe a strength–fracture transition. A further transition to a gravity-dominated regime occurs at sizes when gravity dominates the flow of material in strengthless rock.

The point of transition to gravity dominance depends on the gravity of the target and on the other forces resisting flow, such as sliding friction within the debris, and is not directly addressed here. If there are no other forces resisting flow, gravity will become important once physical strength is eliminated. The point of transition to gravity dominance has nothing to do with static strength, and predictions of the transition point based on a comparison of the gravitational stress with the static strength are bound to fail. This will be seen in Section 5, where we compare these hydrocode results with scaling-law predictions for cratering.

For small impacts, material strength dominates the crater evolution: the crater is confined when the flow has insufficient energy to fracture the material. For large impacts, physical strength is important only at the very beginning of the event, before the shock has fractured the material in which the flow is occurring. Indeed this strength makes the resulting crater larger than in the strengthless case, presumably by distributing the energy and/or momentum more effectively.

4. EFFECTS OF FRAGMENT SIZES

4.1. Fragment Size Distribution

Figure 9 shows contour plots of the fragment sizes resulting from the impact of Section 3.1. Not surprisingly, the fragments are smallest nearer to the impact and get larger with distance. This trend is a result of the stress pattern in the body. In the Grady–Kipp fragmentation model used in the hydrocode, fractures grow as a function of the strain rate, until failure occurs. Failed regions are treated in the model as having zero tensile and shear strength. We discuss the accuracy of this assumption in Section 4.2. Near the impact, fractures nucleate very quickly due to the large strain rate that accompanies the passage of a strong shock. Since there are many fractures, they do not have to propagate far before they intersect and failure occurs. Farther from the impact, the shock weakens, so that the strain rates are lower, resulting in lower nucleation rates. Thus, a few fractures grow large before failure, resulting in large fragments.

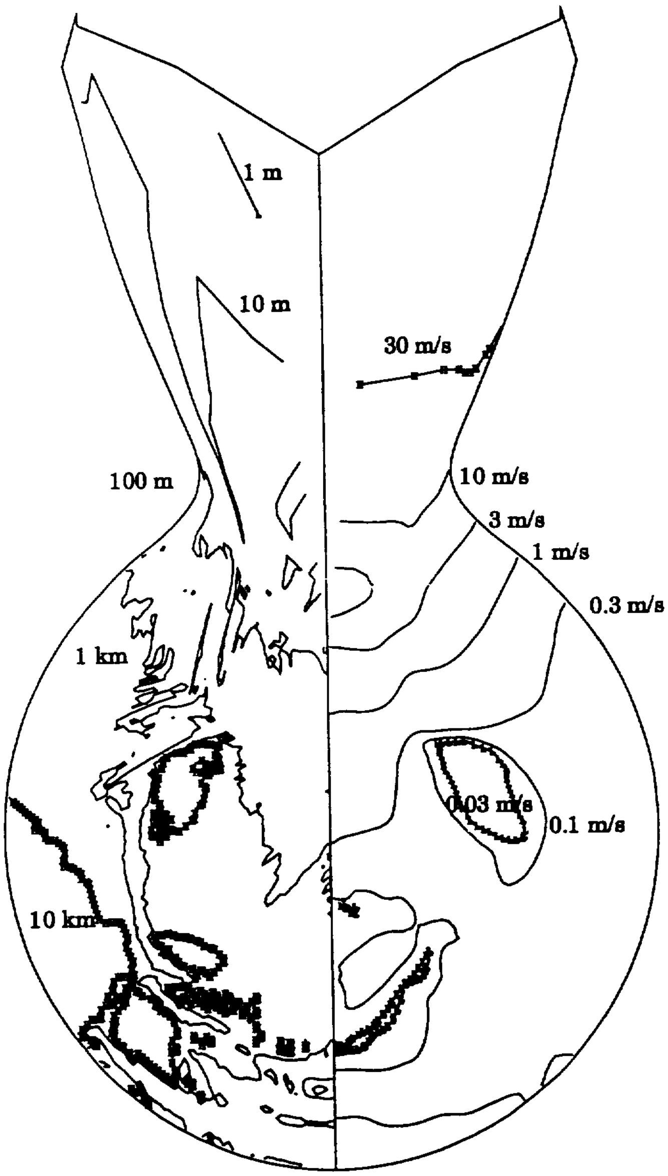

FIG. 9. Contours of the fragment size distribution (left) and the speed distribution (right) from the impacts of Fig. 1.

4.2. Flow in Fragmented Material

An important aspect of the cratering process is the flow within the fractured material. Conventional wisdom requires that rock debris flows as a frictional, strengthless coulomb material, that is, granular flow. However, large terrestrial landslides demonstrate that our understanding of large-scale flow is not adequate to be certain: Vibrations induced in the fractured debris may permit it to flow briefly as a viscous liquid (Gaffney and Melosh 1982).

It is plausible that large blocks will not participate in crater flow without further fracture, due to interlocking of blocks. Our fragmentation model is too simple to investigate this possibility, as it assumes that all fragmented material has zero tensile and shear strength, as discussed in Section 2. This issue is probably unimportant in terrestrial cratering, because gravity dominates the energy budget at the sizes where this process would operate. In other circumstances, for example, asteroid collisions, the problem is more complicated (Nolan 1994).

5. CRATER SIZES

These numerical experiments allow estimates of the sizes of craters formed on the asteroids the size of 951 Gaspra as a function of impactor size. Impactors larger than 60 m in diameter were simulated using the spherical model described earlier, and smaller impactors were simulated using the infinite half-space model. Determination of the final crater size in a numerical model such as this one is quite difficult, because the model material is homogeneous and, in the larger impacts discussed here, completely fluid.

Figure 10 shows a comparison of the sizes of craters formed for a variety of impacts into our model asteroid with the results predicted by scaling-law models. The triangles represent the size of the region within which damage $D = 1$ for each impactor size. These can be considered upper limits to the crater size. The solid line is a least-squares fit to those estimates. Another upper limit to the crater size is that the flow must have enough energy to lift its own weight out of the crater bowl. This constraint determines the gravity-scaled crater size. For impactors larger than about 100 m in diameter, the gravity-scaled estimate (upper dashed line) is smaller than the damaged region. Thus, for such large impacts, gravity stops the crater flow before it reaches the edge of the damaged region. These physical limits are shown schematically in Fig. 11. For small impacts, strength controls the evolution, and there is never a fractured region: the edge of the excavation flow is coincident with the damage front. For larger impacts, the damage front follows the initial shock wave and runs ahead of the excavation flow, creating a fractured region in which flow will be unresisted. The final crater size is limited by the size of this fractured region, which will eventually be cleared by the excavation flow. Strain-rate-dependent strength may determine the size of this fractured region, but in a different way than for smaller impacts. For still larger impacts, a fractured region forms, but there is insufficient energy to raise all of the fractured material against its own weight. This gravity-scaled diameter is an upper limit to crater size, as it depends only on the bulk density of the materials and the impactor and target sizes, not on other material properties of the target. For a Gaspra-sized target, most of the observable craters are in the fracture-controlled range.

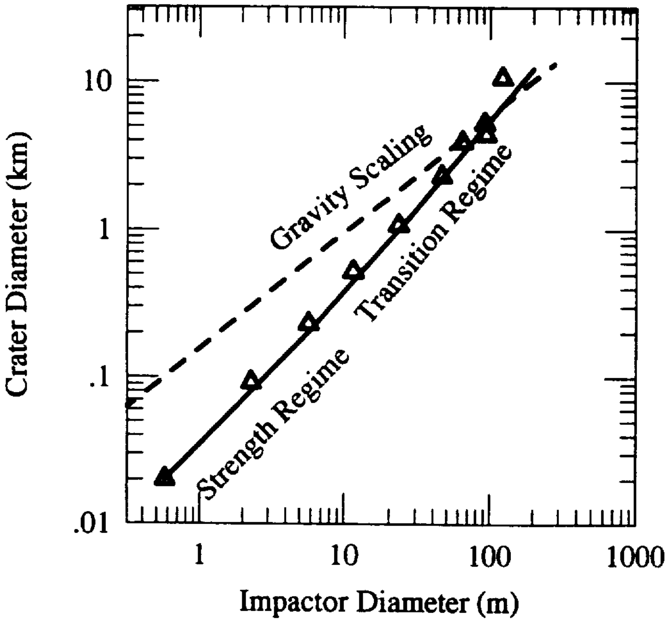

FIG. 10. Crater sizes as a function of impactor diameter for impacts at 5300 m $\sec^{-1}$ into a 12.6-km-diameter (Gaspra-sized) sphere. The gravity scaling curve is from Melosh (1989), for those same impact conditions, with target and projectile densities of 2700 kg m^{-3}. The triangles indicate model results, representing the size of the region within which damage $D = 1$ in each model run, and are upper limits to the crater size for that run. The solid line is a least-squares fit to those results between 5.6 and 150 m impactor diameter, and has the strength-scaling slope smaller for sizes smaller than 5.6 m.

Note, however, that these crater sizes are only upper limits. Viscosity in the flow of crater ejecta may stop the crater flow before it reaches either of these limits, but since viscosity is not included in this model, we are unable to determine its effect. For the smallest craters, the results appear to be linearly dependent on impactor size, indicating that physical strength controls the outcomes.

Based on a comparison of the yield strength of rocks and the force of gravity, most previous workers considered cratering on objects the size of Gaspra to be in the so-called "strength regime." The dominance of strength was assumed because the surface gravity of this size asteroid is low enough that the gravity term in the scaling analysis is negligible compared with the tensile strength of rocks, and for terrestrial craters, the gravity and strength terms seem to be sufficient to describe the cratering process. As discussed above, our hydrocode model suggests that strength, as well as gravity, is much reduced at asteroid sizes, because the shock wave shatters the surrounding rock and destroys any intrinsic strength before the crater itself opens. Note that strength appears to play a role in the energy deposition and the fracture, but not through the same mechanism as for laboratory-scale samples. Previous impacts will also tend to leave a fractured target, so that

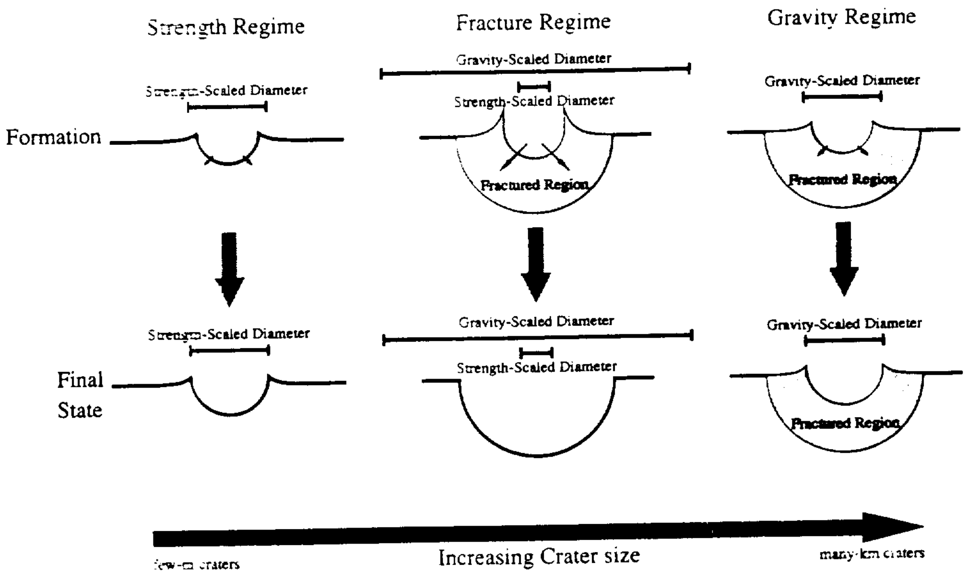

FIG. 11. Schematic of crater formation in the strength (left), fracture (center), and gravity (right) regimes. The crater sizes increase by orders of magnitude from left to right. For small craters (left), strength controls the evolution, and there is never a fractured region. For large craters (right), a fractured region forms, but there is insufficient energy to raise all of the fractured material against its own weight. In the intermediate case, the size of the crater is controlled by the size of the fractured region, which is eventually cleared of material by the excavation flow. The gravity-scaled diameter is an upper limit to crater size, as it depends only on the bulk density of the materials and the impactor and target sizes, not on material properties of the target. For a Gaspra-sized target, most of the observable craters are in the fracture-controlled range.

the initial strength is not likely to be large, but would depend on processes not considered here, such as annealing.

Figure 12 shows the projectile and crater sizes where gravity controls the crater size, as a function of target size. Note that, for small asteroids, most observable craters would be controlled by fracture, not by strength or gravity. For the largest targets, approximately the size of the Moon, gravity is so strong that the "fracture-controlled" region is pinched out. The exact transition point cannot be determined without also considering the effects of lithostatic pressure, which was not done in these simulations. Note also that the effects discussed here do not affect the most easily observed astronomical targets, the terrestrial planets.

6. STRENGTH VERSUS GRAVITY SCALING IN LIGHT OF HYDROCODE RESULTS

For small (centimeter-scale) craters in asteroids, the strength regime applies, whereas for large (kilometer-scale) craters, the gravity regime does apply. In the analyses above, we find that the transition is caused by a loss of

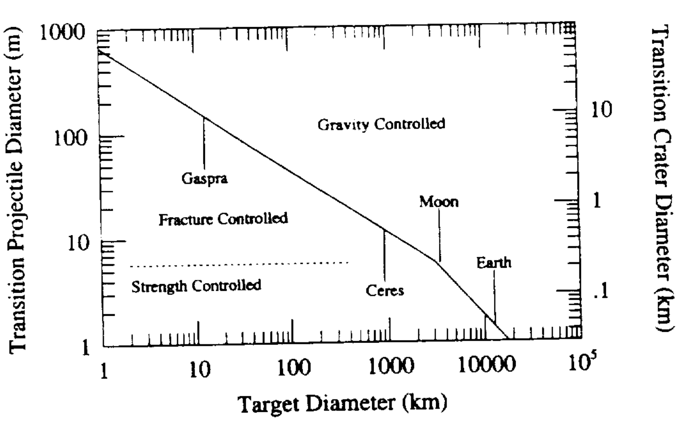

FIG. 12. Projectile (left axis) and crater (right axis) sizes for the strength–fracture (dotted line) and fracture–gravity (solid line) transitions. These computations all assume the impactor and target parameters discussed in this paper (ρ = 2700 kg m^{-3}, v = 5300 m sec^{-1}), and ignore the effect of gravity on fracture, so they are not accurate for the largest targets (Ceres, Moon, and Earth). The strength–fracture transition occurs at a constant size in the range of target sizes between where curvature of the target is important (about 1 km) and where gravity influences the fracture (a few hundred kilometers). This size is the inflection point at 5.6 m shown in Fig. 10. The fracture–gravity transition occurs where the gravity-scaled crater size is the same size as the fractured region, taken to be the fit line from Fig. 10.

strength due to fragmentation preceding ejecta flow, not by a scale-dependent shift in the dominant forces as Housen *et al.* (1983) assume. In addition, we find a transition region in which fracture determines the crater size.

Several authors distinguish between physical strength and impact strength, but then assume that they are related. In a recent example, Housen *et al.* (1991) carefully measured the ASTM tensile and compressive strengths of their target materials, setting aside standardized 2 × 4-in. cylinders cast simultaneously with the targets. This hydrocode model allowed us to watch the fracture proceed in front of the flow, and enabled us to realize that there cannot be any physical strength in the flow region, because the shock had already fragmented the material there.

The change in behavior due to strength degradation was noted by Swift (1977), who used an arbitrary damage model and noted that there is more kinetic and less elastic energy as cratering proceeds, but did not examine size dependence. One potential shortcoming of the hydrocode model is that it does not allow friction-induced shear stress (K. Holsapple, personal communication, 1993). While an ad hoc coefficient of friction would be fairly simple to implement, we have been reluctant to do so, because the hydrocode matches the results of experiments so well. It may be that friction is not important due to acoustic fluidization (*e.g.*, Gaffney and Melosh 1982).

7. CONCLUSION

For impacts into targets the size of asteroid 951 Gaspra, the initial shock wave fractures the target before cratering flow begins (Section 3), so that strength scaling does not apply for crater sizes larger than about 200 m in diameter on Gaspra (Section 5). For the largest observable craters (≥10 km), gravity is the only relevant force.

Using the methods of Housen *et al.* (1983) to scale from laboratory- or weapons-scale experiments is difficult because there is a qualitative change in the cratering mechanism at large scales. This effect is not obvious on the Earth because of the large force of gravity, but it dominates for impacts that have observable effects on asteroids. Thus these numerical experiments complement analytical scaling by allowing the visualization of physical processes at scales difficult to examine in the laboratory.

The results of this hydrocode modeling have been used to match the cratering distributions of asteroids 951 Gaspra (Greenberg *et al.* 1994) and 243 Ida (Greenberg *et al.* 1996), though those treatments do not uniquely test these conclusions.

REFERENCES

Amsden, A. A., H. M. Ruppel, and C. W. Hirt 1980. *SALE: A Simplified ALE Computer Program for Fluid Flow at All Speeds.* LA-8095, Los Alamos National Laboratory.

Asphaug, E. 1993. *Dynamic Fragmentation in the Solar System: Applications of Fracture Mechanics and Hydrodynamics to Questions of Planetary Evolution.* Ph.D. dissertation, Univ. of Arizona, Tucson.

Asphaug, E., and H. J. Melosh 1990. The Stickney Impact of Phobos: A dynamical model. *Bull. Am. Astron. Soc.* **22**, 1112.

Asphaug, E. and H. J. Melosh 1993. The Stickney impact of Phobos: A dynamical model. *Icarus* **101**, 144–164.

Asphaug, E., J. M. Moore, D. Morrison, W. Benz, M. C. Nolan, and R. A. Sullivan 1996. Mechanical and geological effects of impact cratering on Ida. *Icarus* **120**, 158–184.

Benz, W., and E. Asphaug 1994a. Impact simulations with fracture: I. Method and tests. *Icarus* **107**, 98–116.

Benz, W., and E. Asphaug 1994b. Simulations of brittle solids using smooth particle hydrodynamics. *Comput. Phys. Commun.* **87**, 253–265.

Chapman, C. R., and W. B. McKinnon 1986. Cratering of planetary satellites. In *Satellites* (J. Burns and M. S. Matthews, Eds.), pp. 492–580. Univ. of Arizona Press, Tucson.

Gaffney, E. S., and H. J. Melosh 1982. Noise and target strength degradation accompanying shallow-buried explosions. *J. Geophys. Res.* **87**(B3), 1871–1879.

Grady, D. E., and M. E. Kipp 1987. Dynamic rock fragmentation. In *Fracture Mechanics of Rock* (B. K. Atkinson, Ed.), pp. 429–475. Academic Press, New York.

Greenberg, R., W. F. Bottke, M. Nolan, P. Geissler, J.-M. Petit, D. D. Durda, E. Asphaug, and J. Head 1996. Collisional and dynamical history of Ida. *Icarus* **120**, 106–118.

Greenberg, R., M. C. Nolan, W. F. Bottke, Jr., R. A. Kolvoord, and J. Veverka 1994. Collisional history of Gaspra. *Icarus* **107**, 84–97.

Holsapple, K. A., and K. R. Housen 1986. Scaling laws for the catastrophic collisions of asteroids. *Mem. S. A. It.* **57**, 65–85.

Holsapple, K. A., and R. M. Schmidt 1980. On the scaling of crater dimensions: 1. Explosive processes. *J. Geophys. Res.* **85**(B12), 7247–7256.

Holsapple, K. A., and R. M. Schmidt 1982. On the scaling of crater dimensions: 2. Impact processes. *J. Geophys. Res.* **87**(B3), 1849–1870.

Holsapple, K. A., and R. M. Schmidt 1987. Point-source solutions and coupling parameters in cratering mechanics. *J. Geophys. Res.* **92**, 6350–6376.

Housen, K. R., and K. A. Holsapple 1990. On the fragmentation of asteroids and planetary satellites. *Icarus* **84**, 226–253.

Housen, K. R., R. M. Schmidt, and K. A. Holsapple 1983. Crater ejecta scaling laws: Fundamental forms based on dimensional analysis. *J. Geophys. Res.* **88**, 2485–2499.

Housen, K. R., R. M. Schmidt, and K. A. Holsapple 1991. Laboratory simulations of large scale fragmentation events. *Icarus* **94**, 180–190.

Melosh, H. J. 1989. *Impact Cratering: A Geologic Process.* Oxford Univ. Press, New York.

Melosh, H. J., E. V. Ryan, and E. Asphaug 1992. Dynamic fragmentation in impacts: Hydrocode simulation of laboratory impacts. *J. Geophys. Res.* **97**, 14735–14759.

Nolan, M. C. 1994. *Delivery of Meteorites from the Asteroid Belt.* Ph.D. dissertation, Univ. of Arizona, Tucson.

Rinehart, J. S. 1965. *The Dynamic Strength of Rock.* Paper presented at 7th U.S. Symposium on Rock Mechanics.

Ryan, E. V. C. 1992. *Catastrophic Collisions: Laboratory Impact Experiments, Hydrocode Simulations, and the Scaling Problem*. Ph.D. dissertation, Univ. of Arizona, Tucson.

Schmidt, R. M., and K. A. Holsapple 1980. Theory and experiments on centrifuge cratering. *J. Geophys. Res.* **85**(B1), 235–252.

Swift, R. P. 1977. Material strength degradation effect on cratering dynamics. In *Impact and Explosion Cratering* (D. J. Roddy, R. O. Pepin, and R. B. Merril, Eds.), pp. 1025–1042.

Weibull, W. A. 1939. A statistical theory of the strength of materials. *Ingvetensk Akad. Handl.* **151,** 5–45.